http://journal_aeronautical.af-acad.bg/.bg

ISSN 2815-293X
ISSN 2815-2948

Aeronautical Research and Development

1

"*Georgi Benkovski*"

Bulgarian Air Force Academy

April, 2022

Aeronautical Research and Development Volume1, 2022

http://journal_aeronautical.af-acad.bg/.bg

ISSN 2815-293X
ISSN 2815-2948

Aeronautical Research and Development

1

"*Georgi Benkovski*"

Bulgarian Air Force Academy

April, 2022

AERONAUTICAL RESEARCH AND DEVELOPMENT
Volume 1 ▪ Dolna Mitropolia ▪ 2022

"Georgi Benkovski" Bulgarian Air Force Academy

Address

AERONAUTICAL RESEARCH AND DEVELOPMENT

Dolna Mitropolia, 5855

1 "Sv.sv. Kiril i Metodii", St.

journalaeronautical@af-acad.bg

Technical Editor

Yoto Georgiev

Dimitar Nanovski

"Georgi Benkovski"

Bulgarian Air Force Academy, 2022

Aeronautical Research and Development

1

Dolna Mitropolia, 2022

Contents

Deducing of deflection angle and expression of the θ-β-M diagram

Assen Angelov Marinov

Bulgarian Air Force Academy, Faculty of Aviation, asen_aerodynamics@abv.bg

Abstract: The article considers one-dimensional flow, taking into account only the normal component of the velocity, which is normal to the wave. The flow deflection angle was calculated for a Mach number M = 1.5 and the CFD method was used. Then the θ-β-M diagram is expressed.

Keywords: *oblique shock wave, mass equation, momentum equation, energy equation, deflection angle.*

1. Introduction

In many of the aerodynamic tasks the shape of the nose of the aircraft is known, but the angle of formation at supersonic speeds shock wave is not known. This paper presents ways to obtain the flow deflection angle using known mathematical models.

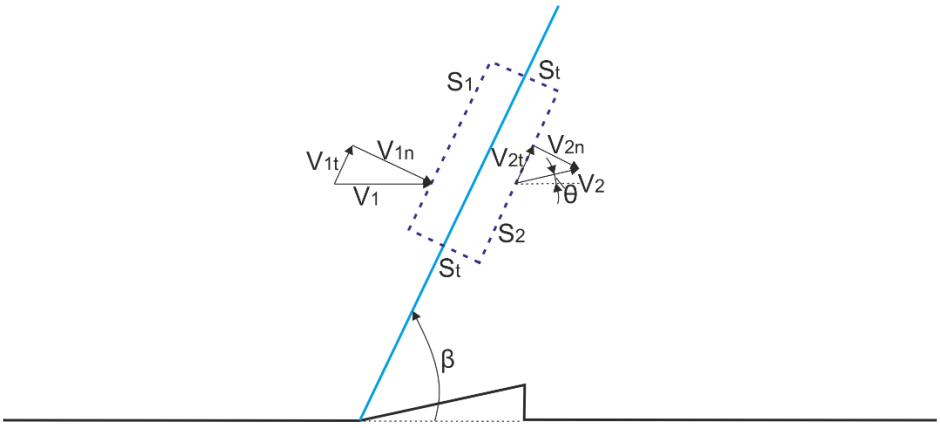

Fig.1.1. Steady conservation equations

Conservation equations describe continuity equation, motion equation and energy equation [1].

Mass equation:

$$\oiint_S \rho V dS = 0 \tag{1.1}$$

Integral have to be expand for side before oblique shock (S_1) and after oblique shock (S_2):

$$-\rho_1 V_{1n} A_{s1} + \rho_2 V_{2n} A_{s2} = 0,$$

(1.2) $A_{s1} = A_{s2} \rightarrow \rho_1 V_{1n} = \rho_2 V_{2n}$

Momentum equation –2D

(1.3) $$\oiint_S V_{t\ or\ n}(\rho V dS) + \oiint_S p dS = 0$$

- tangential component

$$-(\rho_1 V_{1n} A_{s1}) V_{1t} + (\rho_2 V_{2n} A_{s2}) V_{2t} = 0$$
$$A_{s1} = A_{s2}$$
(1.4) $$\rho_1 V_{1n} = \rho_2 V_{2n}$$
$$V_{1t} = V_{2t}$$

- normal component

$$-(\rho_1 V_{1n} A_{s1}) V_{1n} + (\rho_2 V_{2n} A_{s2}) V_{2n} = -(-p_1 A_{s1} + p_2 A_{s2})$$
$$A_{s1} = A_{s2}$$
(1.5) $$p_1 + \rho_1 V_{1n}^2 = p_2 + \rho_2 V_{2n}^2$$

Energy equation –

(1.6) $$\oiint_S \rho \left(e + \frac{1}{2}V^2\right)(V dS) + \oiint_S P\,(V dS) = 0$$

$$-\rho_1 \left(e_1 + \frac{1}{2}V_1^2\right) V_{1n} A_{s1} + \rho_2 \left(e_2 + \frac{1}{2}V_2^2\right) V_{2n} A_{s2} - p_1 V_{1n} A_{s1} + p_2 V_{2n} A_{s2} = 0$$

$$-\rho_1 V_{1n} \left(e_1 + \frac{1}{2}V_1^2 + \frac{p_1}{\rho_1}\right) + \rho_2 V_{2n} \left(e_2 + \frac{1}{2}V_2^2 + \frac{p_2}{\rho_2}\right) = 0$$

$$e + \frac{p}{\rho} = h - enthalpy$$

$$\rho_1 V_{1n} \left(h_1 + \frac{1}{2}V_1^2\right) = \rho_2 V_{2n} \left(h_2 + \frac{1}{2}V_2^2\right)$$

$$\rho_1 V_{1n} = \rho_2 V_{2n}$$

$$\left(h_1 + \frac{1}{2}V_1^2\right) = \left(h_2 + \frac{1}{2}V_2^2\right)$$

$$V^2 = V_n^2 + V_t^2$$

$$V_1^2 - V_2^2 = (V_{1n}^2 + V_{1t}^2) - (V_{2n}^2 + V_{2t}^2)$$

$$V_{1t} = V_{2t}$$

$$V_1^2 - V_2^2 = V_{1n}^2 - V_{2n}^2$$

(1.7) $$h_1 + \frac{1}{2}V_{1n}^2 = h_2 + \frac{1}{2}V_{2n}^2$$

2. θ-β-M relation

For any given Mach number M (1), there is a maximum deflection angle θmax. This is illustrated in Figure 2.1. For any given angle of deflection θ, there are two solutions for a given upstream Mach

number. The smaller solution of β is called the weak shock, and the larger solution of β is the strong shock.

The obtained results for weak shock and strong shock, obtained from the presented mathematical model are presented in figure 2.1 for Mach number = 1.1, 1.5, 2.0, 2.5, 3.0.

Deflection angle θ is a function of M_1 and β [1],

(1.8) $$tan\beta = \frac{V_{1n}}{V_{1t}}$$

$$\tan(\beta - \theta) = \frac{V_{2n}}{V_{2t}}$$

$$V_{1t} = V_{2t}$$

$$\rho_1 V_{1n} = \rho_2 V_{2n}$$

$$\frac{\tan(\beta - \theta)}{tan\beta} = \frac{V_{2n}}{V_{1n}} = \frac{\rho_1}{\rho_2}$$

$$M_{1n} = M_1 sin\beta$$

$$\frac{\rho_2}{\rho_1} = \frac{(\gamma+1)M_{1n}^2}{2 + (\gamma-1)M_{1n}^2}$$

$$\frac{\tan(\beta - \theta)}{tan\beta} = \frac{2 + (\gamma-1)M_1^2 sin^2\beta}{(\gamma+1)M_1^2 sin^2\beta}$$

(1.9) $$tan\theta = 2cot\beta \frac{M_1^2 sin^2\beta - 1}{M_1^2(\gamma + cos2\beta) + 2}$$

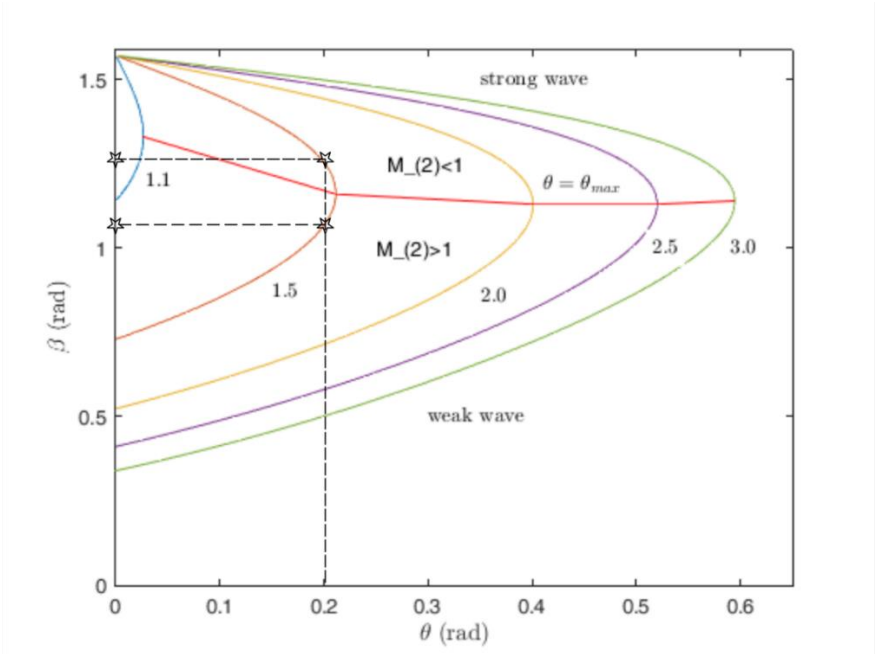

Fig. 2.1. θ-β-M relation

There are a variety of CFD products that solve tasks of different complexity. Some are limited to one-dimensional flows, others to plane flows, and still others solve spatial problems.

To solve the defined task it is necessary to perform the following:

- the area is discretized to a finite number of cells;

- general equations are discretized;
- all equations are solved and the fluid flow is obtained.

The analysis includes the creation of a mathematical model of physical phenomena:

- the laws must be in force throughout the area under consideration;
- the properties of the fluid are modeled empirically;
- assumptions are made for simplification and solution of the problem.

In Figure 2.2 an algorithm of the CFD experiment is presented.

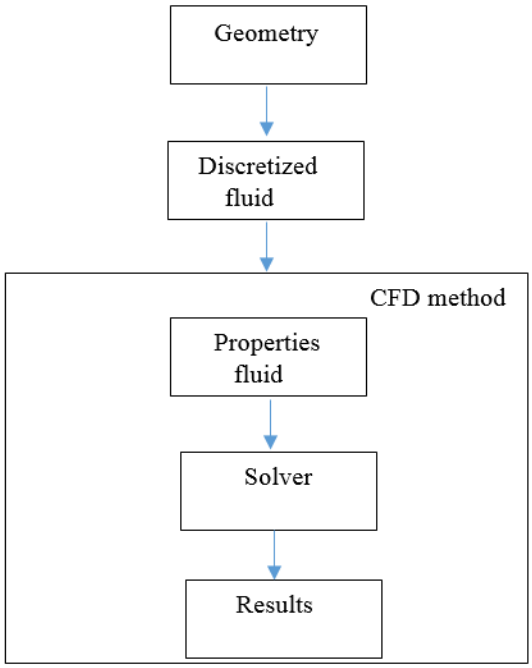

Fig. 2.2. Algorithm of CFD experiment

The result of the Mach number distribution is presented in Figure 2.3.

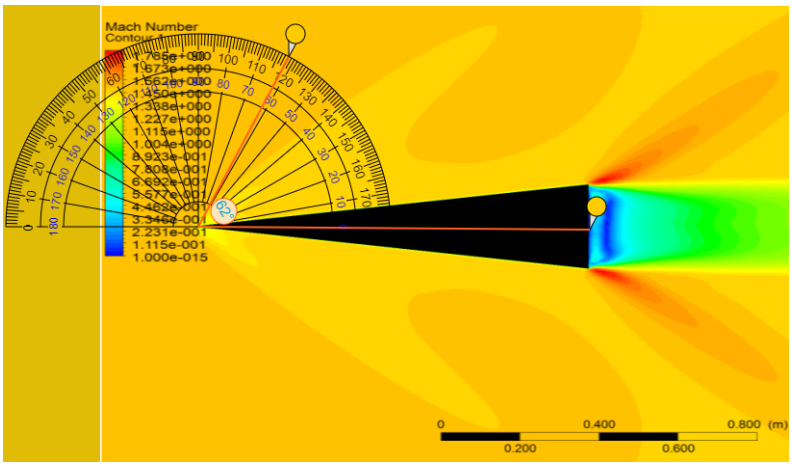

Fig. 2.3. Mach number distribution

3. Conclusion

The difference of approximately two degrees from the calculated $\theta - \beta - M$ diagram and the CFD method is due to the mesh, which is defined in the CFD method. The computational domain has

coordinates 4000 2000 800, and the object in question is located in the middle with coordinates 2000 1000 400. With a maximum size of the element of the computational domain 180. If you reduce the size of the maximum element of the domain and the size of the computational cell the proximity to the flow will also reduce the difference presented.

Appendix.

```
close all; clear; clc;
gama=1.4;
beta_angle=0:0.005:(pi/2);
z=0;
for M1=[1.1,1.5,2.0,2.5,3.0]
z=z+1;
    theta_angle=atan(2*cot(beta_angle).*(((M1^2)*((sin(beta_angle)).^2))-
1) ...
        ./(((gama+(cos(2*beta_angle)))*M1^2)+2));
    m(z)=max(theta_angle);
    n(z)=beta_angle(theta_angle==m(z));
    plot(theta_angle,beta_angle)
    hold on
end
```

References

1. Anderson J., Aerodynamics, McGraw-Hill Education, 2016.

Automatic piloting assessment

Georgi Yordanov

Bulgarian Air Force Academy „Georgi Benkovski“, Dolna Mitropolia, Bulgaria,
georgi_mitkov_iordanov@abv.bg

Abstract: The article examines the principle of the automatic processing of flight data and the assessment of the piloting techniques. It is very important the assessment to be impartial and objective. The use of known models for automatic processing of flight data records and the development of the method for automatic evaluation of the elements performed in flight tasks would lead to a reduction of the subjective factor and optimization of flight assessment. The main requirements are very accurate recognition of the performed elements and the application of approved valuation standards.

Keywords: *aviation, flight, piloting, flight data, assessment*

1. Introduction

Flight training is a complex and responsible process and requires experienced specialists, a good organization and a very good quality control of the flight activity. Assessment of the trainees is complex and involves an evaluation of their theoretical knowledge, their practical skills, and their physical endurance and discipline. Assessment is an essential component of the teaching process and determines how, what, and how well a student is learning. A well designed assessment provides a trainees with something constructive upon which he or she can work or build. An assessment should provide direction and guidance to raise the level of performance.

The evaluation of practical skills is of paramount importance in forming the final grade of the trainee. It is done after each flight, evaluating all the elements of the exercise. For this purpose, flight instructors complete a grade sheet, which, together with other documentation related to flight task, is stored in student’s personal file.

In order to maintain the high quality of the training, the training methodology must be continuously improved and assessment optimized. The main steps to increase the level of the training are:

- up-to-date training programs;
- updating of the manuals regulating flight activity;
- clear standards for the evaluation of piloting techniques;
- the use of modern flight simulators;
- a very good quality control.

The main goal in optimizing the assessment of piloting techniques is to reduce the subjective factor. This could be achieved using a computer application for automatic flight data processing and analysis.

The subjective factor can be reduced by automatically and correctly evaluating the performed elements of the flight task in accordance with the approved standards.

2. Flight data recorders

Flight recorders are electronic devices that record and store important information related to the operation of the aircraft, the operation of its systems, the communication of the crew with the air traffic controller (other aircraft) and the sounds in the cockpit. The sensors are installed on or in the aircraft and are used to measure flight parameters such as airspeed, heading, fuel consumption, altitude, engine temperature, engine rpm, etc. The accessed signals are sampled, filtered, decoded, encrypted, and subjected to an adaptive compression process prior to being stored on self-protected memory device. The present recorders make it possible to record a large number of important parameters on a relatively small and secure storage, and the information can be easily downloaded, processed and analyzed after the flight ends. Computer technology and software allow fast and accurate processing of downloaded information with the ability to visualize.

The information related to the piloting of the aircraft is used in the assessment of the trainees. The flight data recorders record a sufficient number of parameters necessary for a qualitative analysis of the performed flight tasks and an objective assessment of the included elements.

3. Automatic flight data processing

The creation of rational means for automatic processing of flight information uses sufficiently simple models for processing flight data. This also could be embedded in computer analysis software.

3.1. Initial processing of the recorded flight data

Initial processing of flight information involves extracting the data from the aircraft's recorder then decompressing and decrypting it using support equipment and software. It is very important the recorded information to be accurately restored. The processed data can be presented in graphical or tabular form (Figure 1.).

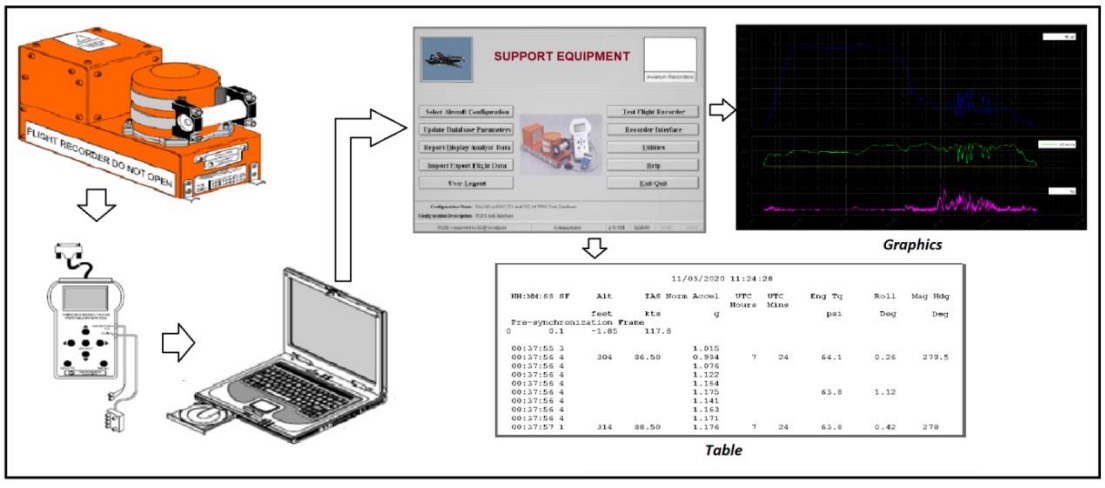

Figure 1.

The data recorded in tabular form is used for in-depth analysis of the completed exercise. In analyzing and evaluating the piloting technique of performed elements in the exercise, several parameters are used. Usually these are – airspeed, altitude, heading, roll, normal acceleration, engine rpm, etc. The data presented in tabular form represent columns of numbers. The length of the columns depends on the duration of the flight and the priority of recorded parameter. Depending on the capability of the flight data recorder, the parameters are recorded every second and the most important of them several times per second. Initially each parameter is processed separately depending on its priority. This includes removing control messages, rounding its values, determining its absolute values, specifying the length of the record, etc. As the lengths of the recorded parameters may be different, they must be equated. For example in 15 seconds can be saved 15 values of the airspeed, 30 values of the roll, and 150 values of the normal acceleration.

3.2. Secondary processing of the recorded flight data

The secondary processing of the flight information involves a qualitative analysis of the recorded flight data. The qualitative analysis is used to determine the elements performed in the flight task and to detect deviations of the parameters from their set values.

The analysis of the flight information is performed in the following areas:

- Analysis of the take-off and landing;
- Analysis of the of simple or complex aerobatics elements;
- Analysis of the en route flight;
- Analysis of combat missions and the obtained results;
- Special analysis.

Of particular importance for the analysis is the correct determination of the beginning and end of the stage or of the element. Also the objects to mandatory determination are its duration, the maximum or minimum values of the considered parameters, etc.

To identify a stage or a element, it is necessary to define several control points, each of which is characterized by the measurement of each of the parameters selected for analysis. The number of control points depends on the studied element. The characteristics of the elements and the stages performed in the flight tasks should be well known, because their characteristics used for identification are set in advance.

First, the flight data is divided into sections (Figure 2.). This requires a pre-set value of some of the studied parameters ($P_{pre\text{-}set}$). Usually the choice of such a parameter depends on the flight task, the type of elements and the plane in which they are performed. For example, for elements of simple aerobatics performed in the horizontal plane, this could be the bank angle(γ), and for elements performed in the vertical plane – airspeed(V) or normal acceleration (ny) (Figure 3.).

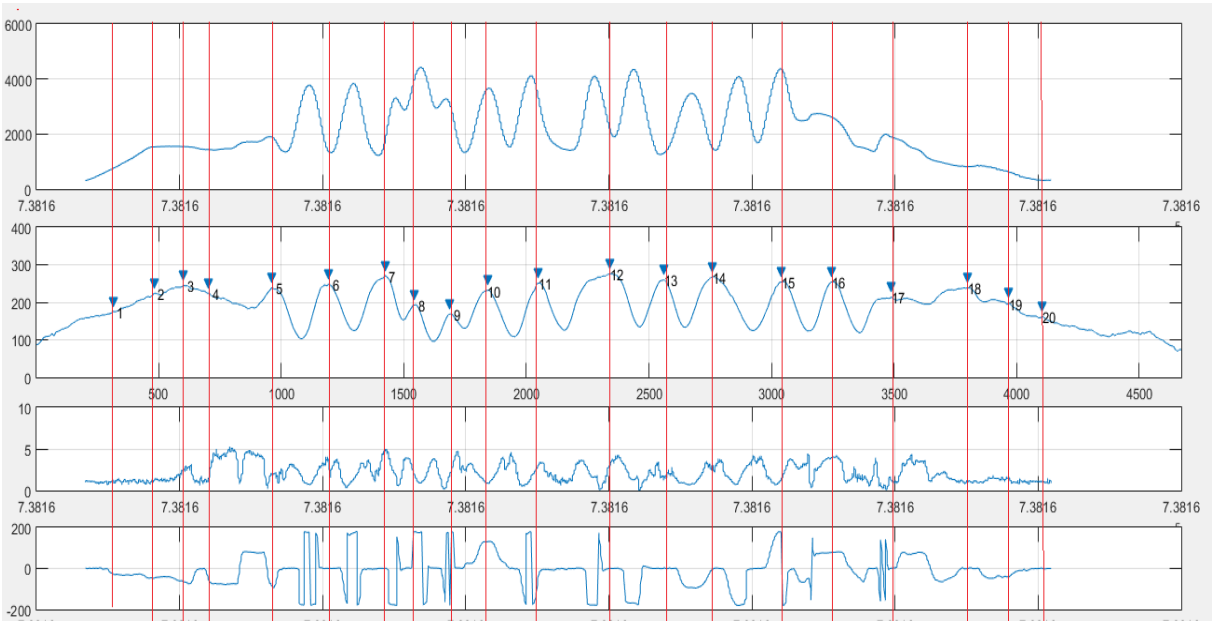

Figure 2.

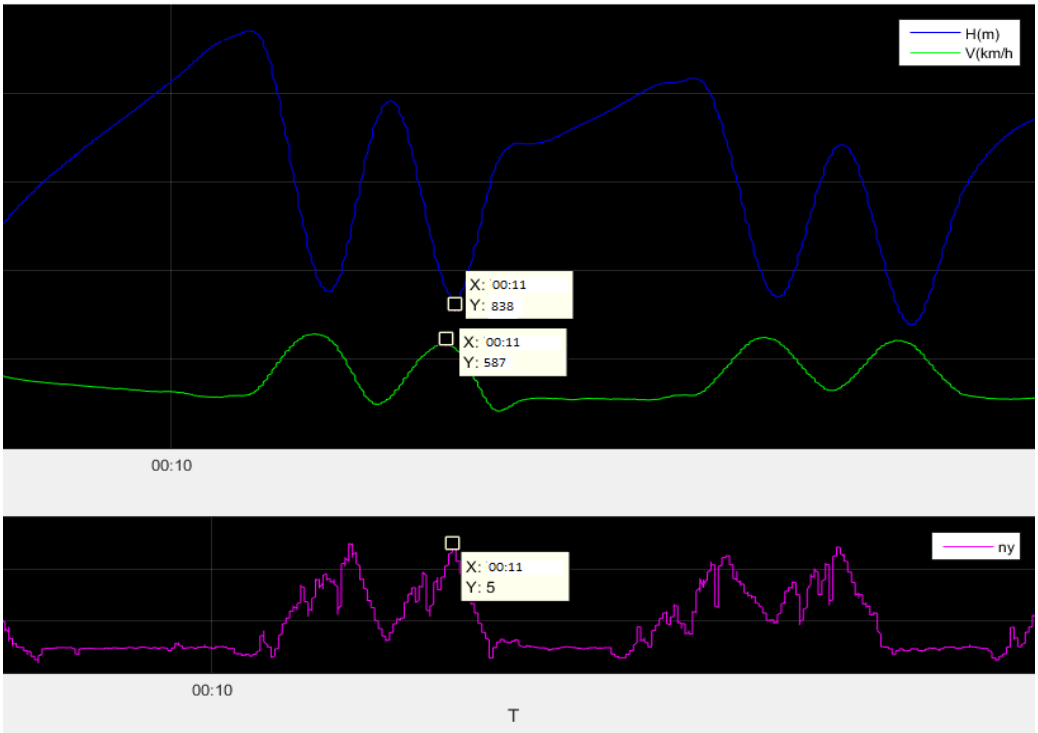

Figure 3.

Next, for each section are determined its duration (Δt), the first and last values of the parameters, the change of parameters and their maximum and minimum values.

$$(1) \quad S(i) = f\begin{pmatrix} Pr_{(1)first};\ Pr_{(1)last};\ Pr_{(1)min};\ Pr_{(1)max};\ \Delta Pr_{(1)};\ Pr_{(1)last} - Pr_{(1)first} \\ Pr_{(2)first};\ Pr_{(2)last};\ Pr_{(2)min};\ Pr_{(2)max};\ \Delta Pr_{(2)};\ Pr_{(2)last} - Pr_{(2)first} \\ \dots \quad \dots \quad \dots \quad \dots \quad \dots \quad \dots \\ Pr_{(n)first};\ Pr_{(n)last};\ Pr_{(n)min};\ Pr_{(n)max};\ \Delta Pr_{(n)};\ Pr_{(n)last} - Pr_{(n)first} \end{pmatrix}$$

- S(i) – sections;
- Pr(n) – a recorded parameter.

The obtained data are compared with pre-set values of the parameters characterizing the stages of the flight or the performed elements in the exercise. If the data match, it is assumed that the corresponding stage or element is performed in this section. In order to distinguish similar elements or variants of any of them, additional features or limitations in some of the parameters are used. For example: a heading, a pitch angle or a bank angle.

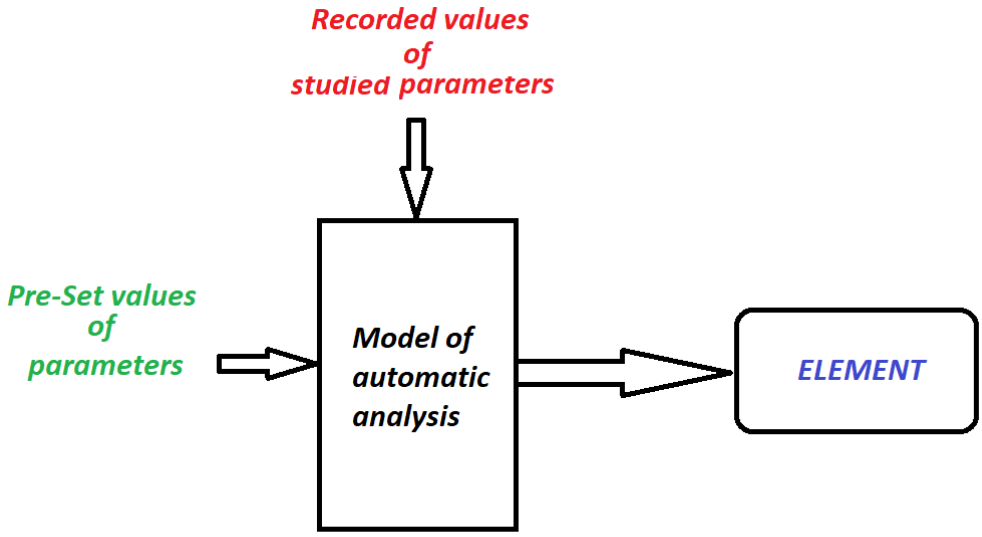

Figure 4.

$$(2) \quad t_{pre-set} - \delta \leq \Delta t \leq t_{pre-set} + \delta$$

$$(3) \quad P_{pre-set} - \delta \leq Pr \leq P_{pre-set} + \delta$$

- $P_{pre-set}$ – a pre-set value of the studied parameter
- δ – a threshold value

The threshold value is a very important for identifying the elements. In the case of a small or a very large tolerance the elements could be missed or confused.

There are several models for automatically identifying the stages of the flight or the elements performed in the exercise. To be more reliable and accurate the identification, several of the models can be combined.

4. Models of flight elements

4.1. Type model

This model shows the position of the center gravity of the aircraft relative to the ground. The flight trajectory can be divided by changing the altitude into three types [1]:

- T_1 – level flight ($\Delta H = 0$);
- T_2 – climb ($\Delta H > 0$);
- $T3$ – descent ($\Delta H < 0$).

The change of heading allows the trajectory to be divided into two more varieties:

- $M1$ – without turns ($\Delta\psi = 0$);
- $M2$ – with turns ($\Delta\psi \neq 0$).

Depending on the positive or negative value of $\Delta\psi$ the turn can be determined on the left or right.

The following relations are used in the formation of logical variables (Table 1.):

- altitude:

(4) $X_1^H => \delta H \leq \Delta H \leq \delta H$

(5) $X_2^H => \Delta H > \delta H$

(6) $X_3^H => \Delta H < \delta H$

- heading:

(7) $X_1^\psi => -\delta\psi \leq \Delta\psi \leq \delta\psi$

(8) $X_2^\psi => \Delta\psi > \delta\psi$

(9) $X_3^\psi => \Delta\psi < \delta\psi$

The sequences of logical variables X_3^H and X_1^ψ formed in time make it possible to determine each spatial trajectory, but not the elements of aerobatics. An additional parameter is needed to describe them. This is the normal acceleration. It introduces three new varieties:

(10) $ny = 1$

(11) $ny > 1$

(12) $ny < 1$

They determine the straightness or distortion of the trajectory. Few new elements are defined (Table 2.).

A sequence of three additional ratios is used to identify aerobatic figures related to the transverse rotation of the aircraft:

(13) $\gamma > \Delta\gamma_{\text{pre-set}}$

(14) $\Delta\gamma = const$

(15) $\gamma > \gamma_{\text{pre-set}}$

For more accurate operation of the identification algorithm, additional conditions are introduced for the individual stages: for example, execution time at each stage.

Table 1.

Sign	Trajectory	Variables	Sign	Elements	Discription
$\mathbf{T_1}$	Level flight	$\mathbf{T_1} = \boldsymbol{X_1^H}$ $-\delta H \leq \Delta H \leq \delta H$	$\mathbf{M_1}$	Straight and level flight	$\mathbf{M_1} = \boldsymbol{X_1^H}.\boldsymbol{X_1^\psi}$
			$\mathbf{M_2}$	Level flight with turns	$\mathbf{M_2} = \boldsymbol{X_1^H}.\overline{\boldsymbol{X_1^\psi}}$
			$\mathbf{M_{2L}}$	Level flight with left turn	$\mathbf{M_{2л}} = \boldsymbol{X_1^H}.\boldsymbol{X_2^\psi}$
			$\mathbf{M_{2R}}$	Level flight with right turn	$\mathbf{M_{2д}} = \boldsymbol{X_1^H}.\boldsymbol{X_3^\psi}$
$\mathbf{T_2}$	Climb	$\mathbf{T_2} = \boldsymbol{X_2^H}$ $\Delta H \geq \delta H$	$\mathbf{M_3}$	Straight climb	$\mathbf{M_3} = \boldsymbol{X_2^H}.\boldsymbol{X_1^\psi}$
			$\mathbf{M_4}$	Climb with turns	$\mathbf{M_4} = \boldsymbol{X_2^H}.\overline{\boldsymbol{X_1^\psi}}$
			$\mathbf{M_{4L}}$	Climb with left turn	$\mathbf{M_{4л}} = \boldsymbol{X_2^H}.\boldsymbol{X_2^\psi}$
			$\mathbf{M_{4R}}$	Climb with right turn	$\mathbf{M_{4д}} = \boldsymbol{X_2^H}.\boldsymbol{X_3^\psi}$
$\mathbf{T_3}$	Descent	$\mathbf{T_3} = \boldsymbol{X_3^H}$ $\Delta H \leq \delta H$	$\mathbf{M_5}$	Straight descent	$\mathbf{M_5} = \boldsymbol{X_3^H}.\boldsymbol{X_1^\psi}$
			$\mathbf{M_6}$	Descent with turns	$\mathbf{M_6} = \boldsymbol{X_3^H}.\overline{\boldsymbol{X_1^\psi}}$
			$\mathbf{M_{6л}}$	Descent with left turn	$\mathbf{M_{6л}} = \boldsymbol{X_3^H}.\boldsymbol{X_2^\psi}$
			$\mathbf{M_{6д}}$	Descent with right turn	$\mathbf{M_{6д}} = \boldsymbol{X_3^H}.\boldsymbol{X_3^\psi}$

Table 2.

Sing	Trajectory	Description
E_1	Straight climb /*ny* = 1/	$M_3(ny = 1)$ or $(\Delta H > 0).(\Delta\psi = 0).(ny = 1)$
E_2	Energetically climb /*ny* > 3/ in the vertical plane along a convex curve	$M_3(ny > 3)$ or $(\Delta H > 0).(\Delta\psi = 0).(ny > 3)$
E_3	Energetically climb with turn /*ny* > 3/ in the vertical plane along a convex curve	$M_4(ny > 3)$ or $(\Delta H > 0).(\Delta\psi \neq 0).(ny > 1)$
E_4	Straight descent /*ny* = 1/	$M_5(ny = 1)$ or $(\Delta H < 0).(\Delta\psi = 0).(ny = 1)$
E_5	Energetically descent /*ny* > 3/ in the vertical plane along a convex curve	$M_5(ny > 3)$ or $(\Delta H < 0).(\Delta\psi = 0).(ny > 3)$
E_6	Energetically descent with turn /*ny* > 3/ in the vertical plane along a convex curve	$M_6(ny > 3)$ or $(\Delta H < 0).(\Delta\psi \neq 0).(ny > 3)$

4.2. Mathematical model.

The mathematical model of description is used to identify the aerobatic maneuvers performed in the exercise. Aerobatic maneuvers are divided into maneuvers from the horizontal, vertical and inclined planes [1]. This model includes the change of the trajectory of the aircraft and some limitations in the parameters characterizing the individual elements (Figure 5.).

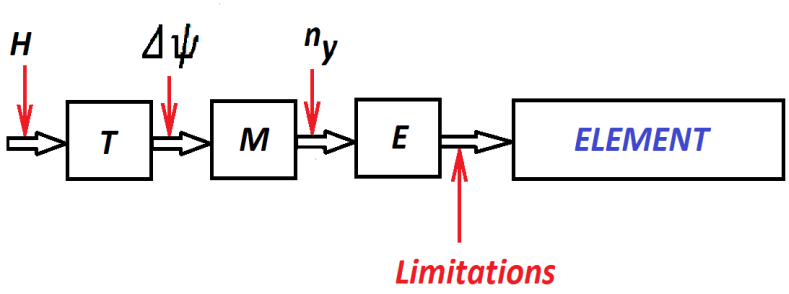

Figure 5.

For example:

360 Turn. Characteristics: the altitude and speed from the beginning to the end of the figure are constant. Limitations: change of course greater than 330°.

(16) $F_T = \{M_2.[|\Delta\psi| \geq 330^o]\}M_2$

- $\{.....\}M_2$ – requirement for continuity of the maneuver.

Loop. Characteristic features: normal acceleration ny > 3, change in altitude and speed in both halves of the figure and at control points. Limitations: change of roll – up to 10°, change of heading to be greater than 330°.

(17) $F_L = \{[T_2(ny>3).(\Delta\vartheta \geq 75^o)][|\gamma| \leq 10^o][T_3(ny>3)(\Delta\vartheta \leq -75^o)]\Pi[\Delta\psi \geq 330^o]\}_{T2,T3}$

- Π – requirement for correct sequence of performance.

The absence of the necessary characteristics for more than the set time means that the figure is not fulfilled.

5. Automatic piloting assessment

For each type of aircraft there are determined permissible indicators characterizing the performance of the elements. They are determined taking into account the characteristics of the aircraft itself and the level of training of the pilot. In practice, it is considered that the less the maximum deviation from set values, the higher the quality of piloting. The threshold values of the assessed parameters are selected on the basis of static studies and recommendations from experienced pilots. The choice of high thresholds leads to inflated grades, which contradicts the safety rules. Traditional assessment depends on a grading scale of "excellent", "good", "fair" and "poor".

Computer software for automatic processing and analysis of flight information, which automatically indentifies the stages of the flight and the performed elements, can also be used for their automatic assessment. Used evaluation criteria and standards are introduced into the program (Figure 6.).

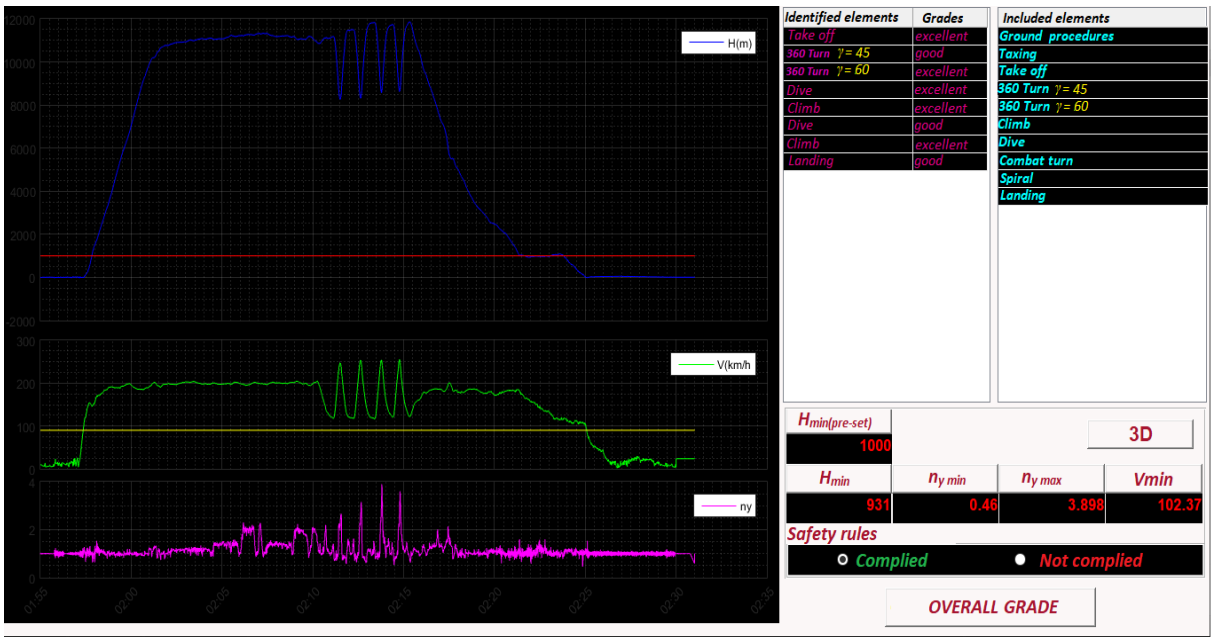

Figure 6.

Firstly all values of the evaluated parameters are determined at each control point of the identified stage or element. The obtained data is compared with the set values for the correct performance. These values are described in the flight manuals for the aircraft.

Next, the deviations are calculated and compared with the pre-set evaluation standards. The evaluation of the each element is the arithmetic mean of the results obtained for each evaluated parameter. For example, an element will be considered "excellent", if the deviations of all evaluated parameters are within "excellent", if a parameter goes beyond these standards, then the assessment of the element will be reduced.

(18) $O_E = \frac{O_{p(1)}+\ldots+O_{p(n)}}{n}$

Overall flight assessment includes grades of all assessed stages of the flight and all performed elements and represents their arithmetic mean. This is provided that all assessed elements are equivalent.

(19) $O_{Ft} = \frac{c.O_{E(1)}+\ldots+c.O_{E(n)}}{n}$

- c – criterion for the complexity of the elements

A criteria can be introduced for the complexity of the performed element, which changes the assessment in such way that the lower assessment of the easy-to-perform elements has less impact on the overall assessment.

6. Conclusions

- The computer application for automatic analysis and evaluation of flight tasks must include several models for automatic identification of the performed elements.
- The elements included in the flight exercises must be known in detail.
- The initial processing of flight data is essential and plays an important role in the automatic analysis of information.
- The automatic identification of the elements in flight tasks depends on the type of exercise and the spatial plane in which the elements are performed.
- The number of identified elements depends on the number of used parameters, respectively on the capabilities of the flight data recorder – the larger number of recorded parameters allows the detection of more elements.
- Setting too small or too large threshold values of the studied parameters leads to omission of one element or to its confusion with another one.
- The reliability in detecting the elements increases with the addition of more studied parameters and additional limitations.
- The detected elements must correspond to the ones set in the exercise – this can also be used as an indicator of the reliability of the identification.

- In order to perform the automatic assessment of the element, control points must be determined and the values of the parameters recorded in them must be compared with the evaluation criteria and standards set in advance.
- The overall grade of the flight task is determined as the arithmetic mean of the grades of the elements and depends on their number and their complexity.

References

1. Rumen Georgiev, "Technical tools and algorithms for flight information processing", “Vasil Levski” National University, Faculty of Aviation, Dolna Mitropolia, 2004.
2. Flight Crew Standardization and Evaluation Manual.
3. Source [online] Available:https://www.mathworks.com/matlabcentral/answers/.

Synthesis and research of a controller for microclimate stabilization in an automobile based on finite state machines

Radostina Calovska, Stefan Biliderov

Pleven, Bulgaria, radostina.calovska@gmail.com

Airforce academy, Faculty Aviation, Dolna Mitropolia, Bulgaria, biliderow_ss@yahoo.com

Abstract: The model is designed to control the temperature in a car body by opening and closing a window. The control of the window is done mechanically, by a button for lowering and raising or automatically, by a logic controller realized on the basis of the theory of finite state machines. Automatic control leads to energy savings and helps maintain the driver's concentration.

Keywords: *energy saving, logic controller, climate control*.

1. Introduction.

Maintaining a favorable microclimate in the cabin of a car is related to ensuring the performance of passengers and directly affects the mood and emotions of both the driver and passengers. Energy efficiency in this process is particularly important in order to save energy, hence fuel and protect the environment.

The general statement of the research is shown in Fig.1. This is a Matlab-Simulink model [4].

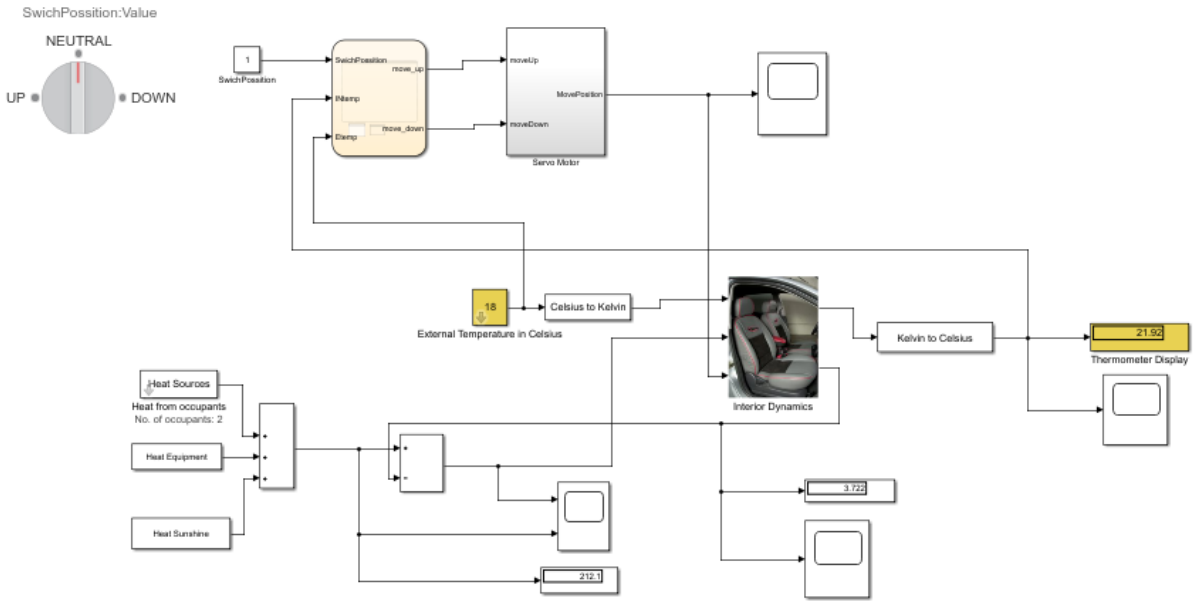

Figure 1. The general statement of the research

2. Processes in the interior dynamics

The temperature in the cabin is accumulated by:

- incoming energy emitted by the number of passengers;
- the energy from the working appliances in the cabin;
- solar energy that enters through glazed surfaces;
- thermal convection, which occurs when opening and closing the window.

The model of thermal and thermodynamic processes in the car body are shown in Fig 2.

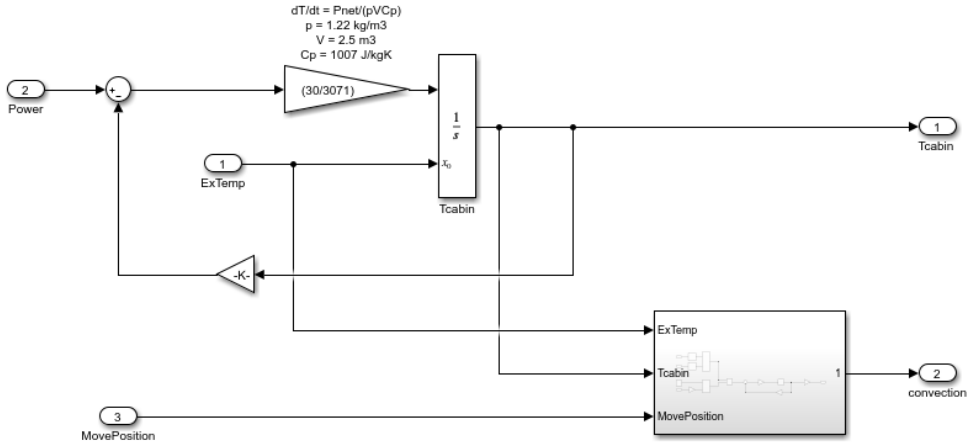

Figure 2. Mathematical model of the thermal processes in the car.

The heat given off by the equipment operating in the passenger compartment is determined by [1]:

- electrical heat equivalent Y / kWh;
- power used kW;
- the coefficient of useful activity.

The value of the conditional solar constant is 1.32-1.34 Kw / (m² x min) [2].

The rate of heat transfer by convection Q ̇_conv is determined by Newton's law of cooling [3], expressed as:

(1) $\dot{Q}_{conv} = hA(T_S - T_f)$

where: $\dot{Q}_{conv}$is heat transfer rate, (W); A is heat transfer area, (m^2); h is convective heat transfer coefficient, (W / (m^2.K)); T_s is surface temperature, (K); T_f is outdoor temperature, (K).

The model of the convection system is shown in Fig.3.

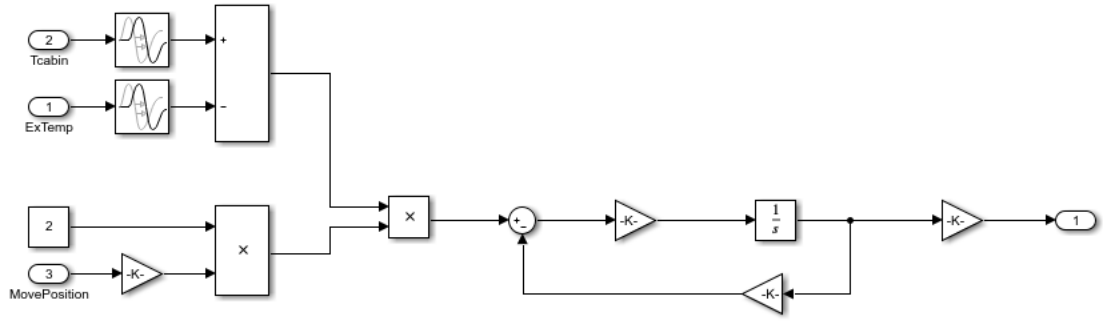

Figure 3. Convection system model

3. Inputs and Outputs

The model is realized so that it is possible at any time to monitor the incoming heat energy in the interior dynamics of a car compartment and the outgoing energy from convection. The working process of temperature regulation can be seen in Fig.4. In this figure, the temperature is shown like function of time.

The working actuator in this system is a window of the car. The temperature is regulated by changing of the window position. Temperature changes in the cabin and the movement of the window are observed until the thermal processes are stabilized. The process of moving the window is shown on Fig.5. In this figure the moving of the windows is shown like function of the time.

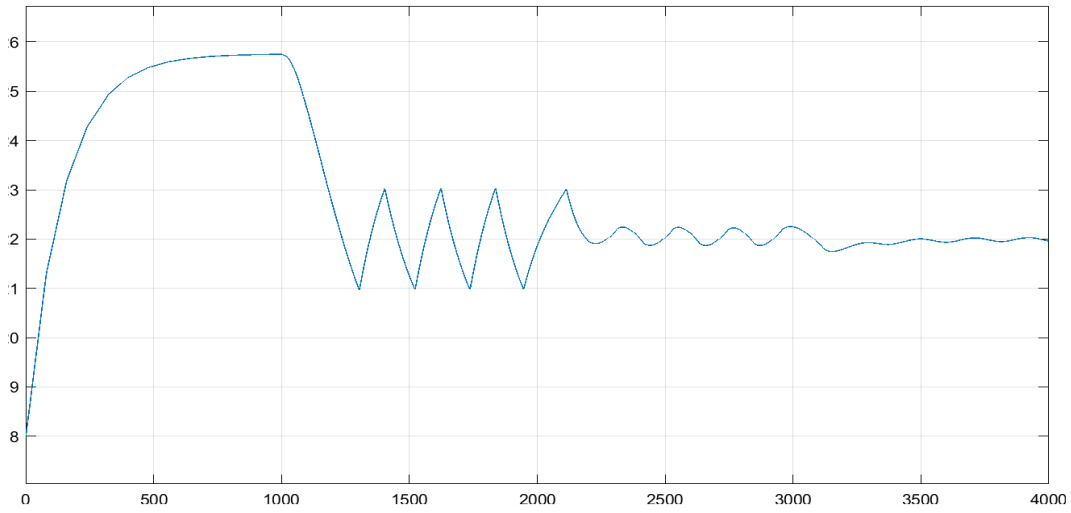

Figure 4. Graph of temperature changes of interior dynamics like function of the time

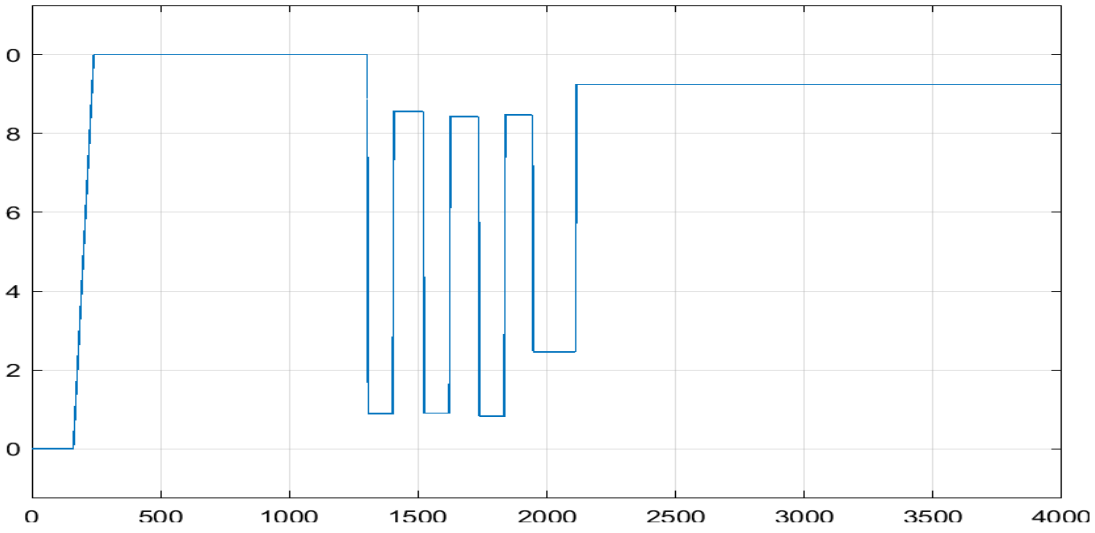

Figure 5. Window movement schedule like function of the time

4. **Implement a controller for Automatic window control based on finite state machines.**

The logic of the controller driving the process of thermoregulation of the car body has been developed, using the theory of the finite state machines. This logic is shown in Fig.6.

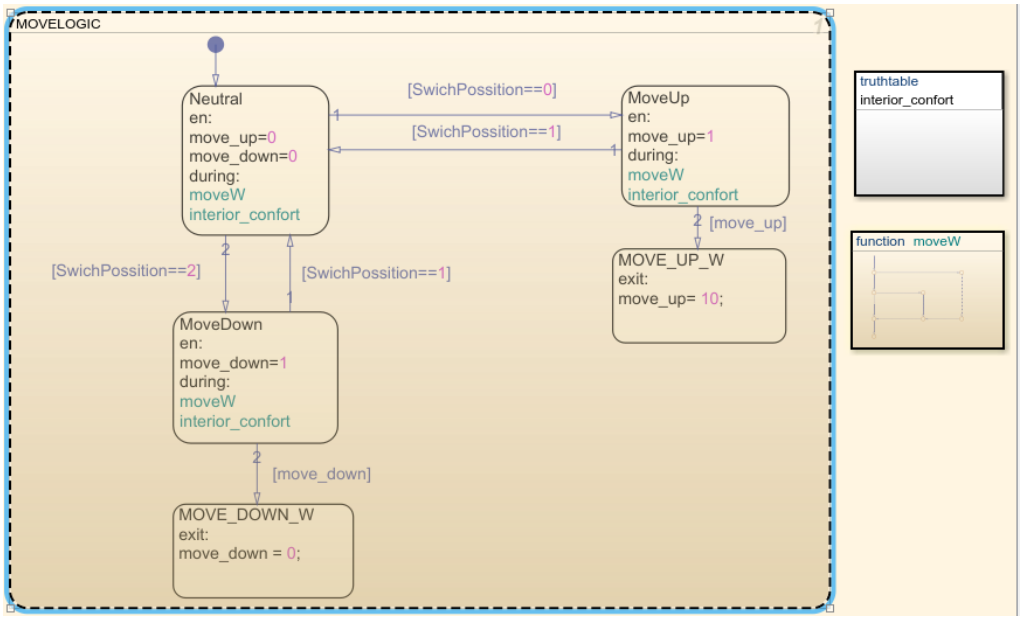

Figure 6. The control logic of termoregulation

Fig.6 shows that the control logic is based on three main states: Neutral; Move up; Move down. 4.2. The transition from one state to another is done by a condition for the position of the key. While the logic is in a given state, it sends a signal to the servo motor that drives the window. The mechanical drive is set by a function If-Else-If-Else on Fig.7:

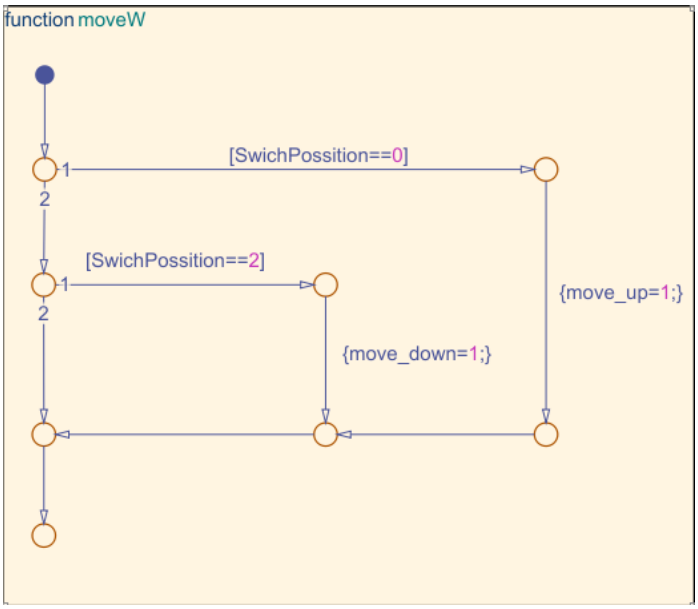

Figure 7. If-Else-If-Else function to perform a conditional action

In the automatic mode the window drive is controlled by a truth table shown in Fig.8.

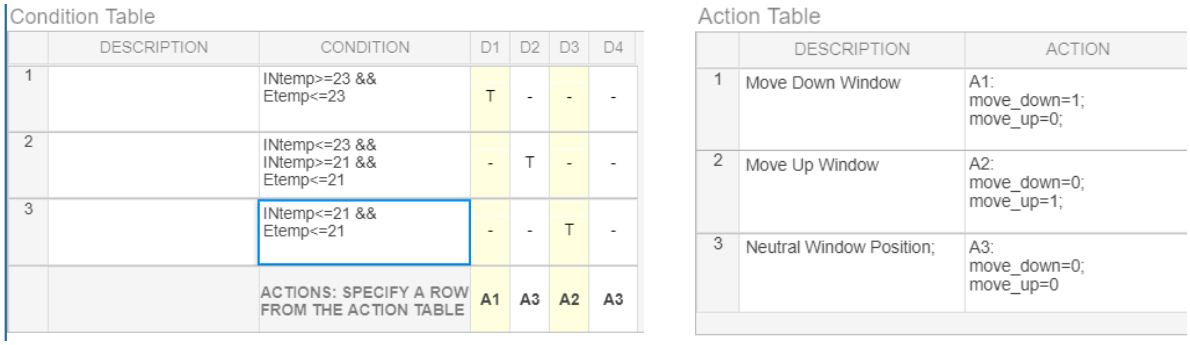

Condition Table

	DESCRIPTION	CONDITION	D1	D2	D3	D4
1		INtemp>=23 && Etemp<=23	T	-	-	-
2		INtemp<=23 && INtemp>=21 && Etemp<=21	-	T	-	-
3		INtemp<=21 && Etemp<=21	-	-	T	-
		ACTIONS: SPECIFY A ROW FROM THE ACTION TABLE	A1	A3	A2	A3

Action Table

	DESCRIPTION	ACTION
1	Move Down Window	A1: move_down=1; move_up=0;
2	Move Up Window	A2: move_down=0; move_up=1;
3	Neutral Window Position;	A3: move_down=0; move_up=0

Figure 8. Truth table to command a window according to temperature

The truth table fulfills the conditions:

- if the internal temperature is greater than or equal to 23 degrees and the external temperature is less than or equal to 23 degrees, send a move signal down to window;
- if the inside temperature is between 23 degrees and 21 degrees and the outside temperature is less than 21 degrees, the window stay in the neutral position;
- if the internal temperature is less than or equal to 21 degrees and the external temperature is less than or equal to 21 degrees, send a signal to window to move up.

The controller takes a signal for the position of the key, a signal from the outside temperature and a signal from the temperature in the compartment. One signals is output from the controller to the servo motor, for upward and downward movement.

5. Conclusions

1. The Finite State Machine are widely used in the control of automated devices. The program for the development of stateflow automata is convenient for programming, as it works in conjunction with other programming languages.

2. Working with Simulink allows the installation of the Finite State Machine in many ready-made models. The Finite State Machines allow the development of different complexity control models through different built-in logics.

3. The advantage of vending machines is that they have a memory that allows you to start from the last active state when revisiting.

References

1. Златев К. Системи за осигуряване живота и дейността на екипажа в летателние апарати". гр.Долна Митрополия, 1984г.

2. Слънчева радиация или йонизираща радиация от слънцето. Обща слънчева радиация. <https://kerchtt.ru/bg/solnechnaya-radiaciya-ili-ioniziruyushchee-izluchenie-solnca-summarnaya/> 15.03.2022

3. Convection Heat Transfer <http://www.mhhe.com/engcs/mech/cengel/notes/ConvectionHeatTransfer.html> 15.03.2022

4. Vehicle Electrical and Climate Control Systems <Vehicle Electrical and Climate Control Systems - MATLAB & Simulink (mathworks.com)> 15.03.2022

Combat use of aircraft with unguided weapons

Milen Atanasov

"Georgi Benkovski" Bulgarian Air Force Academy, e-mail: maa_69@abv.bg

Abstract: The development and introduction of a common ballistic model in the general algorithm of operation of the aviation combat complex will lead to a reduction in the volume of computational operations, which will increase the speed and accuracy of solving combat tasks. Increasing accuracy, in turn, leads to a reduction in the cost of achieving the objectives set for combat aviation.

Keywords: *aircraft, bombing, shooting.*

1. Introduction

Aviation combat complexes are designed to destroy air, land, water and underwater targets with the help of aviation weapons.

At present, the aviation combat complexes use the appropriate mathematical models and algorithms for combat use for each type of weapon. As a result, the pilot manually selects via switches: the type of target (air or ground); moving or stationary target; the type of weapon; mobile or stationary aviation automatic weapons, etc. By selecting the type of weapon, the appropriate ballistic model is selected to determine the ballistic elements.

The rational use of aviation combat complexes by the pilot in performing the assigned tasks is of great importance in the development of new models of aviation equipment.

The introduction of the latest achievements of science and technology in combat aviation allows the compilation and introduction of a common algorithm for combat use of different groups of weapons, as well as the improvement of avionics decisive for the execution of combat missions.

The use of a common algorithm in aviation combat complexes will allow to shorten the decision-making process of the pilot, as well as to facilitate his work with the arms control bodies of the aircraft. It will also increase the speed of computers that solve combat tasks and expand the areas of initial conditions for combat use of weapons.

2. Mathematical modelling of combat use with unguided weapons

Unguided weapons (UW) are used in a wide range of aircraft speeds and altitudes, angles and distances to the target, the presence of an angle between the velocity vectors of the aircraft and the initial

speed of the UW. Different airborne targeting systems use fundamentally different ballistic schemes, requiring specific methods of solving ballistic tasks and forms of presenting the results of decisions.

It is therefore necessary to draw up a common ballistic model for all types of UW, with the type of UW used being introduced on board the aircraft.

Using Newton's second law:

(1) $\sum \bar{F} = \bar{a}m,$

and presenting equation (1) in scalar form, the flight time T of the flight and the coordinates η_s, ζ_s, ξ_s of the contact of the weapons with the target in the navigation basis $O\eta\zeta\xi$ are determined.

Using the vector kinematic method, the point of contact of the weapon with the target is determined from where the target distance vector $\overline{D}_0$ at the time of the shot is calculated:

(2) $\bar{D}_0 = f\left(\bar{a}_{v1}, \dot{\omega}_{yD}, \dot{\omega}_{zD}, \ddot{D}, \bar{V}_1, \bar{V}_t, \bar{U}, \dot{D}, \omega_{yD}, \omega_{zD}, H, \eta_s, \zeta_s, \xi_s, \bar{r}_c, T, \psi, \vartheta, \gamma, \beta_s, \alpha, \beta', \varepsilon'\right),$

where,

$\bar{a}_{v1}, \dot{\omega}_{yD}, \dot{\omega}_{zD}$ - the vector of the acceleration of the aircraft and the accelerations of the angular velocities of the vector of the distance to the target;

$\overline{V}_1, \overline{V}_t, \overline{U}$ - the velocity, target and wind vectors;

$\dot{D}$ - the speed of convergence of the aircraft with the target;

ω_{yD}, ω_{zD} - the angular velocities of the distance vector to the target;

H - the height of shooting and bombing;

$\bar{r}$ - the vector determining the deviation of the projectile in the case of a mobile artillery weapon;

β', ε' - the angles determining the direction of the weapon relative to the aircraft.

The angles $\beta_{t1,0}, \varepsilon_{t1,0}$ of aiming at the target in the connected coordinate system $Ox_1y_1z_1$ are:

(3) $\beta_{t1,0} = f(D_{0z1}, D_{0x1});$

$\beta_{t1,0} = f\left(D_{0z1}, D_{0y1}, \beta_{t1,0}\right).$

The test is performed for firing with: aviation artillery projectile caliber d = 23 mm, initial velocity V_0 = 700 m / s, ballistic coefficient c = 1.52, mass m = 199 g [17]; with unguided aircraft rocket with characteristics [1, 2, 3]: d = 57 mm, initial velocity V_0 = 56 m / s, mass m = 3.86 kg, mass of the propellant engine m_p = 1.13 kg, operating time on the powder engine t_a = 0.9 s, maximum speed V_{max} = 673 m / s [2, 3]; and bombing with an aircraft bomb FAB 500 M62 [4] with a characteristic time θ = 20.38 s, mass m = 497 kg.

2.1. Results of mathematical modelling of combat use with unguided weapons

The study is performed for air shooting with aviation artillery and UR under the following conditions: angle of convergence $\lambda = -10^0$, angle of attack of the aircraft $\alpha = 1^0$, speed V of the aircraft from 240 m/s

to 300 m/s, height H of fields from 4000 m to 6500 m, target speed V_t = 220 m/s, with the target angle of the target relative to the distance q=150^0 и 90^0 In case the shooting is performed with unguided rocket (UR), the vector based $\bar{L}_0$ on the weapon has values: L_{x1}=0, L_{y1}=1 m, L_{z1}=2,5 m.

As a result of solving the problem of the contact of the weapons with the target, the angles $\beta_{t1,0}$ and $\varepsilon_{t1,0}$ are determined, determining the position of the target at the time of firing and the distance D_c of firing.

2.1.1. Shooting with a fixed weapon at an air target

Tables 1 - 6 show the calculated angles $\beta_{t1,0}$, $\varepsilon_{t1,0}$ and distances D_c of the firing.

At target target q = 150^0: the angle $\beta_{t1,0}$ changes in the range from -9.920 to -8.720, the angle $\varepsilon_{t1,0}$ is in the range from -1.200 to -1.140, the distance D_c of shooting - from 701.22 m to 719. 37 m.

At the target course q = 90^0: the angle $\beta_{t1,0}$ is in the range from -14.620 to -13.370, the angle $\varepsilon_{t1,0}$ is in the range from -3.230 to -3.050, the distance D_c of the shooting - from 717.85 m to 721.49 m.

Table 1.

λ= -10^0, V$_t$= 220 m/s, q=150^0				
β$_{t1,0}$, degr.	**V=240, m/s**	**260**	**280**	**300**
H=4000, m	-9.92	-9.63	-9.36	-9.11
4500	-9.82	-9.54	-9.27	-9.02
5000	-9.72	-9.45	-9.18	-8.94
5500	-9.64	-9.36	-9.10	-8.86
6000	-9.55	-9.28	-9.03	-8.79
6500	-9.47	-9.21	-8.96	-8.72

Table 2.

λ= -10^0, V$_t$= 220 m/s, q=150^0				
ε$_{t1,0}$, degr.	**V=240, m/s**	**260**	**280**	**300**
H=4000, m	-1.18	-1.16	-1.15	-1.14
4500	-1.18	-1.17	-1.16	-1.15
5000	-1.19	-1.17	-1.16	-1.15
5500	-1.19	-1.18	-1.17	-1.16
6000	-1.19	-1.18	-1.17	-1.16
6500	-1.20	-1.18	-1.17	-1.16

Table 3.

λ= -10^0, V_t= 220 m/s, q=150^0				
D_c, m	**V=240, m/s**	**260**	**280**	**300**
H=4000, m	701.22	705.37	709.34	713.18
4500	702.60	706.53	710.87	714.51
5000	704.13	707.86	712.01	716.05
5500	705.32	709.44	713.41	717.27
6000	706.19	710.70	714.49	718.16
6500	707.90	711.66	715.27	719.37

Table 4.

λ= -10^0, V_t= 220 m/s, q=90^0				
$\beta_{t1,0}$, degr.	**V=240, m/s**	**260**	**280**	**300**
H=4000, m	-14.62	-14.31	-14.01	-13.72
4500	-14.54	-14.23	-13.93	-13.64
5000	-14.46	-14.15	-13.86	-13.57
5500	-14.38	-14.08	-13.78	-13.50
6000	-14.31	-14.01	-13.72	-13.44
6500	-14.24	-13.94	-13.65	-13.37

Table 5.

λ= -10^0, V_t= 220 m/s, q=90^0				
$\varepsilon_{t1,0}$, degr.	**V=240, m/s**	**260**	**280**	**300**
H=4000, m	-3.23	-3.18	-3.13	-3.09
4500	-3.22	-3.17	-3.12	-3.08
5000	-3.21	-3.16	-3.12	-3.07
5500	-3.21	-3.16	-3.11	-3.06
6000	-3.20	-3.15	-3.10	-3.06
6500	-3.19	-3.14	-3.10	-3.05

Table 6.

λ= -10^0, V_t= 220 m/s,q=90^0				
D_c, m	**V=240, m/s**	**260**	**280**	**300**
H=4000, m	721.49	720.83	719.61	718.69
4500	721.22	720.44	719.10	718.91
5000	720.73	719.83	719.21	718.05
5500	720.87	719.86	719.14	717.87
6000	720.82	719.71	718.89	717.50
6500	720.61	719.40	718.47	717.85

2.1.2. Shooting with UR at a stationary ground target

The study is performed for shooting with UR on a moving and stationary ground target under the same conditions as for shooting aviation artillery weapons, as the base vector $\bar{L}_0$ has the following values: L_{x1}=0, L_{y1}=1 m, L_{z1}=2,5 m.

The angles $\beta_{t1.0}$, $\varepsilon_{t1.0}$, the distance D_c of firing, the time T_c of flight of the projectile and the speed V_c of meeting the projectile with the target are shown in table 7 - table. 10 and fig. 1.

The shooting conditions that meet the conditions for the allowed distance (D_c = 800 - 1800 m) are for heights H from 400 m to 600 m inclusive with a diving angle λ= -20^0.

The calculations were performed in winglessness due to which the angle $\beta_{t1,0}$ =0^0.

Table 7.

λ =-20, degr UR						
$\varepsilon_{t1,0}$, degr	**V=200 m/s**	**220**	**240**	**260**	**280**	**300**
H=400, m	-2.39	-2.30	-2.23	-2.17	-2.10	-2.05
500	-2.56	-2.47	-2.39	-2.32	-2.26	-2.20
600	-2.74	-2.65	-2.56	-2.48	-2.41	-2.35
700	-2.95	-2.84	-2.75	-2.66	-2.59	-2.51
800	-3.16	-3.05	-2.95	-2.86	-2.77	-2.69
900	-3.40	-3.28	-3.17	-3.07	-2.98	-2.89

Table 8.

λ =-20, degr UR						
D_c, m	V=200 m/s	220	240	260	280	300
H=400, m	1096.46	1100.82	1104.19	1107.20	1110.49	1112.99
500	1360.38	1365.53	1370.54	1374.56	1378.65	1382.38
600	1618.97	1625.62	1631.99	1637.75	1643.00	1647.77
700	1872.24	1880.86	1888.30	1895.46	1902.03	1908.50
800	2119.80	2129.92	2139.21	2147.81	2156.17	2163.57
900	2360.75	2372.55	2383.87	2394.16	2403.84	2413.30

Table 9.

λ =-20, degr UR						
T_c, degr	**V=200 m/s**	**220**	**240**	**260**	**280**	**300**
H=400, m	1.86	1.82	1.79	1.75	1.72	1.68
500	2.32	2.28	2.23	2.19	2.14	2.10
600	2.82	2.76	2.71	2.65	2.60	2.55
700	3.34	3.28	3.22	3.15	3.09	3.03
800	3.90	3.83	3.76	3.69	3.62	3.55
900	4.48	4.40	4.32	4.24	4.17	4.09

Table 10.

λ =-20, degr UR						
V_c, degr	**V=200 m/s**	**220**	**240**	**260**	**280**	**300**
H=400, m	592.96	607.60	622.54	637.66	652.84	668.35
500	540.51	553.88	567.36	581.21	595.18	609.39
600	494.20	506.07	518.11	530.43	543.05	555.98
700	453.72	464.08	474.80	485.73	496.96	508.40
800	418.91	427.89	437.15	446.71	456.52	466.71
900	389.61	397.24	405.10	413.30	421.80	430.55

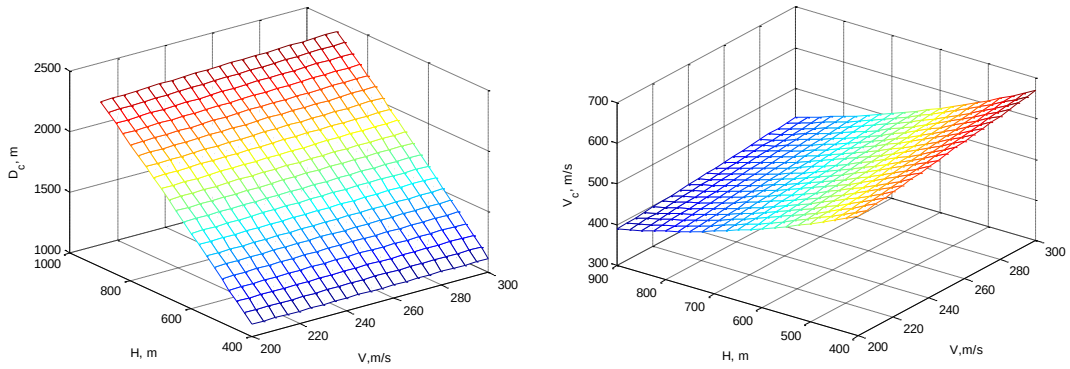

Figure 1. The distance D_c and the speed V_c when shooting with UR on a ground stationary target

2.1.3. Bombing moving target with FAB 500 M62

The study is performed for bombing with an aircraft bomb FAB 500 M62 from horizontal flight and diving on a moving and stationary target with angles λ = -20^0, -40^0, angle of attack of the aircraft α= 1^0, gliding angle β_s = 0, speed V of aircraft from 200 m/s to 300 m/s, bombing height H from 500 m to 1000 m, target speed V target = 60 km/h, target angle ψ_t = 300. The base has values: L_{x1}=L_{y1}=L_{z1}=0 m.

From table. 11 - table 19 it is seen that when bombing from a horizontal flight from heights greater than 600 m and speeds greater than 220 m/s the angle $\varepsilon_{t1,0}$ is greater than the limit value for sighting head C17 VG due to which the bombing will take place in the invisible zone and will use the method "Continuously Computed Release Point" - CCRP. For other conditions, the bombing will take place in the visible area using the method "Continuously Computed Impact Point" - CCIP.

In the case of a dive bomb for the specified conditions, the bombing will take place in the visible area by the CCIP method.

The distance of bombing for horizontal flight is in the range from 1905.65 m to 3997.42 m, and for diving from 690.77 m to 2155.68 m, as the distance for conditions λ = -40^0, V = 200 m/s, H = 500 m (D_c = 690.77 m) borders the safe distance.

Table 11.

λ =0, degr OFAB 500						
$\beta_{ц1,0}$, degr	**V=200 m/s**	**220**	**240**	**260**	**280**	**300**
H=500, m	-2.66	-2.41	-2.20	-2.03	-1.88	-1.77
600	-2.67	-2.41	-2.21	-2.03	-1.89	-1.78
700	-2.67	-2.42	-2.21	-2.04	-1.90	-1.79
800	-2.68	-2.43	-2.22	-2.05	-1.91	-1.80
900	-2.69	-2.43	-2.23	-2.05	-1.91	-1.81
1000	-2.69	-2.44	-2.23	-2.06	-1.92	-1.81

Table 12.

λ =0, degr OFAB 500						
$\varepsilon_{ц1,0}$, degr	**V=200 m/s**	**220**	**240**	**260**	**280**	**300**
H=500, m	-16.20	-14.81	-13.66	-12.68	-11.87	-11.21
600	-17.61	-16.10	-14.85	-13.79	-12.91	-12.20
700	-18.88	-17.28	-15.93	-14.80	-13.86	-13.10
800	-20.05	-18.36	-16.94	-15.74	-14.75	-13.95
900	-21.14	-19.37	-17.88	-16.61	-15.58	-14.74
1000	-22.16	-20.31	-18.76	-17.44	-16.36	-15.48

Table 13.

λ =0, degr OFAB 500						
D_c, m	V=200 m/s	220	240	260	280	300
H=500, m	1905.65	2093.12	2281.03	2468.78	2650.16	2819.51
600	2098.50	2301.87	2505.93	2709.82	2905.97	3088.50
700	2278.87	2496.51	2714.92	2933.30	3142.80	3337.06
800	2449.56	2679.99	2911.48	3143.24	3364.77	3569.35
900	2612.34	2854.67	3098.38	3342.24	3574.70	3788.67
1000	2768.76	3022.09	3276.96	3531.95	3774.41	3997.42

Table 14.

λ =-20, degr OFAB 500						
$\beta_{ц1,0}$, degr	**V=200 m/s**	**220**	**240**	**260**	**280**	**300**
H=500, m	-2.49	-2.26	-2.07	-1.91	-1.78	-1.67
600	-2.48	-2.25	-2.07	-1.91	-1.78	-1.67
700	-2.47	-2.25	-2.06	-1.91	-1.78	-1.67
800	-2.46	-2.24	-2.06	-1.90	-1.78	-1.67
900	-2.45	-2.23	-2.05	-1.90	-1.78	-1.67
1000	-2.44	-2.23	-2.05	-1.90	-1.78	-1.67

Table 15.

λ =-20, OFAB 500						
$\varepsilon_{u1,0}$, degr	**V=200 m/s**	**220**	**240**	**260**	**280**	**300**
H=500, m	-9.67	-8.55	-7.63	-6.88	-6.26	-5.76
600	-10.69	-9.46	-8.46	-7.63	-6.94	-6.38
700	-11.64	-10.32	-9.24	-8.33	-7.60	-6.98
800	-12.53	-11.13	-9.97	-9.01	-8.21	-7.56
900	-13.36	-11.89	-10.66	-9.64	-8.80	-8.11
1000	-14.14	-12.61	-11.32	-10.25	-9.37	-8.64

Table 16.

λ =-20, degr OFAB 500						
D_c, m	V=200 m/s	220	240	260	280	300
H=500, m	1042.56	1081.37	1115.54	1145.44	1171.58	1193.96
600	1211.57	1259.10	1301.30	1338.80	1371.40	1399.60
700	1373.85	1429.51	1479.60	1524.46	1563.53	1597.69
800	1530.28	1594.07	1651.87	1703.75	1749.40	1789.32
900	1681.83	1753.37	1818.74	1877.77	1929.59	1975.13
1000	1829.44	1908.31	1980.85	2046.61	2104.61	2155.68

Table 17.

λ =-40, degr OFAB 500						
$\beta_{u1,0}$, degr	**V=200 m/s**	**220**	**240**	**260**	**280**	**300**
H=500, m	-2.42	-2.20	-2.03	-1.87	-1.75	-1.64
600	-2.40	-2.19	-2.02	-1.87	-1.74	-1.63
700	-2.38	-2.18	-2.01	-1.86	-1.73	-1.63
800	-2.36	-2.16	-2.00	-1.85	-1.73	-1.63
900	-2.35	-2.15	-1.99	-1.84	-1.73	-1.62
1000	-2.33	-2.14	-1.98	-1.84	-1.72	-1.62

Table 18.

λ =-40, OFAB 500						
$\varepsilon_{u1,0}$, degr	**V=200 m/s**	**220**	**240**	**260**	**280**	**300**
H=500, m	-7.40	-6.60	-5.95	-5.41	-4.98	-4.62
600	-7.99	-7.12	-6.41	-5.82	-5.34	-4.95
700	-8.56	-7.62	-6.85	-6.21	-5.70	-5.27
800	-9.09	-8.09	-7.27	-6.60	-6.04	-5.58
900	-9.60	-8.54	-7.68	-6.96	-6.37	-5.88
1000	-10.09	-8.98	-8.07	-7.32	-6.70	-6.19

Table 19.

λ =-40, degr OFAB 500						
D_c, m	V=200 m/s	220	240	260	280	300
H=500, m	690.77	700.08	707.90	714.55	720.06	724.77
600	820.85	832.73	842.71	851.31	858.51	864.54
700	948.95	963.45	975.83	986.42	995.26	1002.86
800	1075.41	1092.60	1107.40	1119.93	1130.62	1139.76
900	1200.25	1220.20	1237.34	1252.10	1264.72	1275.41
1000	1323.69	1346.40	1366.02	1382.95	1397.34	1409.69

3. Conclusions

1. It can be seen that as the exchange rate q decreases, the angles $\beta_{t1,0}$ and $\varepsilon_{t1,0}$ increase. At $q = 90^0$, the existing sighting heads used in aviation targeting systems cannot work out the calculated angles for $\beta_{t1,0}$ ($B_{t1,0max} = \pm 12^0$ for C17 VG). In order to reduce the angle $\beta_{t1,0}$ in absolute value it is necessary to reduce the angle of the target or to reduce the firing distance. Reducing the firing distance at a large angle leads to an increase in the overload of the pilot when performing the aiming maneuver and difficulties in aiming.

Decreasing q reduces the angle $\beta_{t1,0}$ in absolute terms to a greater extent than by reducing the firing distance.

2. From the research conducted on UR firing at ground target, it can be concluded that in order to increase the range of firing altitude, it is necessary to increase the diving angle.

The angles $\varepsilon_{t1,0}$ when firing with air artillery weapons are smaller than when firing with UR, which is explained by the greater distances η than that of UR.

3. From the research performed on horizontal flight and dive bombings, it can be concluded that increasing the diving angle increases the area of use of the CCIP method.

For the bombing conditions under consideration, the angle $\beta_{t1,0}$ does not exceed the limit values $B_{t1,0max} = \pm 12^0$ for C17 VG.

References

1. Kostov M.I., Aviatsionna vŭnshna balistika, S, VI, 1985 g.

2 https://topwar.ru/165730-neupravljaemaja-aviacionnaja-raketa-s-5u-novyj-variant-starogo-izdelija.html

3. http://www.russianarms.ru/forum/index.php?topic=5769.0

4. https://11750-bg.all.biz/fugasna-aviatsionna-bomba-fab-500m62-g76338

Battery energy storage technology for aviation - An overview

Yoto Georgiev Georgiev

"Georgi Benkovski" Air Force Academy, Faculty of Aviation, Dolna Mitropolia, Bulgaria, y_g_g@abv.bg

Abstract: The article presents progress in last years of aviation rechargeable Li-ion batteries. Improvements in recent years have led to increase in energy and power density. Remaining challenges and future research directions are summarized. Emphasis is placed on the safety of aviation Li-ion batteries.

Keywords: *aviation, rechargeable batteries, Lithium-ion batteries*

1. Introduction

Rechargeable batteries are devices in which electricity is converted into chemicals and vice versa, which distinguishes them from other batteries. Initially, under the action of an external source of direct current, charging reactions are performed, chemical energy accumulates. This is the reaction of charging the battery. In the second stage, of the operation of the battery, the chemical energy is converted into electricity.

Rechargeable batteries are widely used in aircrafts as emergency and auxiliary sources of electricity, representing several series connected and installed in a common battery housing. On-board rechargeable batteries are designed for:

- power supply of electric starters and other equipment for autonomous starting of aircraft engines;
- supply of vital consumers in case of failure of the electrical generators during the flight;
- covering the peak loads when switching on powerful consumers;
- inspection of the operation of low-power equipment on the ground in the absence of airport sources of electricity.

There is a focus right now of converting everything that we use to run on electricity. Currently, new developments of future aircraft focus on the electric and electric – hybrid aircraft, while features, as the specific energy and thermal instability of the available rechargeable battery technology cause serious problems [1], [2], [3]. Li-ion batteries could offer higher energy density, which have gained enormous attention to researchers [4]. Therefore, it will be made research on the recent advances of the of Li-ion batteries. Sodium-ion batteries are considered as the best candidate power sources in transportation because sodium is widely available (the fourth most abundant element on earth) and exhibits similar chemistry to that of lithium-ion batteries, but their specific energy density is lower than Li-ion batteries [5]. In comparison with terrestrial rechargeable batteries, safe and high specific energy rather than cost is the major constraint for aviation. Other rechargeable batteries as lead-acid and nickel-cadmium batteries are currently being replacing in aviation by lithium-ion technology, because it can offer greater capacity for less weight. It should be made clear difference between power density – W/kg, and energy

density – Wh/kg. The storage devices with the highest power density are the supercapacitors while with the highest energy density – lithium-ion batteries.

2. Improving Lithium Batteries

Lithium-ion batteries are nowadays technology with application in many fields. The significant improvement of the lithium-ion battery technology was made when lithium metal as an anode active material was changed by carbonaceous compounds, mostly graphite. According to the electrolyte lithium-ion batteries are divided into three groups: with liquid electrolytes [6],[7]; with polymer electrolytes [8], [9], and with solid-state inorganic electrolytes [10], [11], [12].

Nowadays, the most widely used lithium-ion batteries in aviation are lithium-polymer. They are so called because the electrolyte is a thin polymer film. Possibility to replace liquid organic electrolyte to polymer, which should reduce the likelihood of its leaks and increase the safety of the lithium-ion battery, has been studied since the beginning of the commercialization of these current sources. The idea of a lithium polymer battery (Li-pol) is based on the phenomenon of the transition of some polymers into semiconductor state as a result of the introduction of electrolyte ions into them. In this case, the conductivity of polymers increases by more than an order of magnitude. The efforts of researchers have been directed to the search for polymer electrolytes for both lithium-ion batteries and batteries with metallic lithium, the theoretically possible energy density of which is several times higher than that of lithium-ion batteries. Its electric voltage is 3,6 V. Lithium-polymer aviation batteries consist of eight cells located in a common metal housing, giving 28,8 V in total with energy density 260 Wh/kg. Generally, lithium-ion aircraft batteries applications have an underestimated full charge voltage at cell compared to household batteries, respectively lower electrical capacitance, but due to this – more service life.

New concept with using Si nanoparticles with carbon nanotubes was developed in Taiwan for Li-ion batteries [13]. This solved the long-standing rate capability problem of ionic liquid electrolyte. Tests show that this battery retains its capacity after a cycle of 300 charge-discharge [13].

Solid-state Li-ion batteries are thought to be potential next-generation energy storage devices for future aircrafts. In all solid-state Li-ion batteries electrolytes is solid. This is novel concept replacing electrolyte with solid instead of liquid or polymer to obtain higher energy density and to reduce the risk of fire. New research shows that can be achieved voltage 5 V for single cell battery with charge-discharge current density (0.5C = 200 mA/cm^2) [14]. Using cells with voltage 5 V instead of 3,6 V will reduce its number in aviation rechargeable batteries from 8 to 6, and thus reducing the imbalance between individual cells. The biggest problem with solid-state Li-ion batteries is production itself. At current state of art its production cost is much higher than Li-ion batteries with liquid and polymer electrolytes.

In Japan, researchers reported that with K_2NiF_4-type Ba-Li oxyhydride solid electrolyte, hydride ions (H^-) can be used in solid-state Li-ion batteries as charge carrier that facilitates fast ionic conduction in

solids [15]. The significance of this discovery is that it thus increases the conductivity through the solid electrolyte. Another breakthrough from this year (2022) [16] was published by Chinese scientists who achieved to increasing 10 times the diffusion coefficient of Li ions of Li metal anode. They used metallic lithium replacing the graphite anode to increase the energy density of the rechargeable battery. But what is significant in their study is the use of lithium hydride (LiH) nanoparticles which achieved two goals: prevent growth of dendritic lithium and increase the mobility of lithium ions.

Another solution for preventing lithium dendrites was proposed by international team of scientist in March 2022 [17]. The idea is to use hierarchical porous structure on anode made by Cu, P, Co and C which significantly localizes lithium dendrite growth.

The reason why scientists and engineers around the world are actively working to mitigation the lithium dendrite growth is that when it reaches the cathode a short circuit occurs in the battery and an explosion occurs. It is needless to say why explosions are unacceptable in aviation. What distinguishes the two studies above from the others is that the efforts so far have been aimed at creating a barrier between the two cathodes, while the new methods are based on preventing the formation of lithium dendrites.

To date (March 2022) rechargeable batteries known to science with highest energy density are Li-O_2 batteries, due to the highest energy density (11,700 Wh/kg based on Li-metal mass) in theory compared with any other rechargeable batteries [18]. The biggest problems for Li-air batteries are H_2O and CO_2 that exist in ambient air, which can not only form byproducts with discharge products (Li_2O_2), but also react with the electrolyte and the Li anode [19]. Theoretically, the model of Li-air batteries with liquid electrolyte has been developed in 1976 by E. L. Littauer and K. C. Tsai of the Lockheed Missiles & Space Company (USA), and in 1996 K. M. Abraham and Z. Jiang created a lithium-oxygen battery with solid electrolyte. The lithium-oxygen rechargeable battery (Li-O_2) consists of a lithium anode, an electrolyte, a separator and an oxygen cathode. In theory, this type of rechargeable battery has energy comparable to the energy of organic fuels used in aviation.

Another technology currently being actively developed is using silicon for anode [20]. In [21] is provided a general overview of recent progress and the current problems and prospects, and is summarized the future research of silicon anode lithium batteries.

An important aspect of aviation batteries is the correct measurement of the charge level. Using Thevenin model and Kalman filter new method for charge estimation of lithium batteries was developed in China, published in December 2021, with error in less than 0,8 % [22]. Till now it is one of the most accurate methods for charge estimation of lithium batteries found in scientific literature.

3. A safety of a Li-ion battery

When considering and analyzing of a given technology and its application and development in aviation, one of the main aspects is its level of safety. The external short circuit, overcharge and overheat are the main events that can lead to the destruction of Li-ion batteries and in the worst cases to explosion.

One of the significant factors concerning safety of Li-ion batteries is cell imbalance which varies each cell voltage in the battery pack overtime. To solve that problem in the battery pack the battery cells should be leveled to keeps up the difference in charged levels of the cells in the battery as small as possible. There are different techniques of cell balancing classified in two groups: passive and active cell balancing methods [23], [24]. Passive cell balancing method equalizes the charge level of individual cells by dissipation of energy from the most charged, while active cell balancing method transfers energy from higher charged cells to lower charged ones [25]. Battery cell balancing not only increases the safety level of the Li-ion battery but also extends its service life.

Another important topic concerning safety of Li-ion batteries is thermal management. To improve the safety and reliability of Li-ion aviation batteries is of great importance correct prediction of temperature fields inside cells. A very dangerous condition occurs when a self-induced temperature rise occurs, called thermal runaway, which results in battery explosion [26], [27], [28]. Several fires had occurred in commercial aircrafts due to thermal runaway of lithium-ion batteries [29]. The prevention of thermal runaway in lithium-ion aviation batteries is vital as in FMEA analysis it is one of the factors for high value of RPN (risk priority number). Methods for battery thermal management are air cooling, liquid cooling, heat pipe cooling and phase change cooling and in case of lower temperature battery warming. Passive systems for heat removal using phase change process are better options compared to forced air and liquid cooling methods. The uses of passive cooling systems eliminate the costs associated with the installation, maintenance and operation of active cooling systems that require fans and pumps with electric power supplies. When using passive cooling of lithium-ion batteries there are no external power sources or forces, no moving mechanical parts, and no moving working fluid. Another motivation for the use of passive cooling systems for aviation lithium-ion batteries is the potential for enhanced safety through increased safety system reliability – safety is vital for aviation.

Air-cooling system is simple with low cost. In case for aviation what differs from convention lithium-ion batteries is that pressure decrease with increase of the altitude of the aircraft. A novel air-cooling structure design has been proposed by Chinese scientist with profiling the mass flow through the cells [30]. Unfortunately, till now for current air-cooling system, the cooling efficiency is still not enough for the large aviation batteries due to lower pressure in higher altitude [30].

The liquid cooling is more efficient cooling method compared with air cooling, but the liquid cooling system is more sophisticated than air-cooling and there is risk of occurring loss of coolant accident due to leakage of liquid working fluid and last but not least with more weight. Researches in this field are focused on finding the most efficient working fluid. Italian scientists [31] made experiments for investigating the cooling capabilities of different cooling fluids. The experimental results show that the perfluorinated polyether fluid has the best performance [31].

Cooling with phase change materials shows in last years to be very efficient for lithium-ion battery thermal management. Phase change cooling systems are two types: solid-liquid phase change [32] and gas-liquid phase change [33]. Solid-liquid phase change materials are used in passive cooling systems,

and the gas-liquid phase change materials are used in active cooling systems. Phase-change cooling involves the use of the heat of vaporization of the coolant or heat of transition from solid to liquid (and vice versa). A team of scientists from Hefei Energy Research Institute, China proposed in 2019 a flexible form stable composite phase change material for battery cooling [34]. Experiments have shown 20ºC lower battery temperatures using novel flexible form stable composite phase change materials. Another breakthrough was made in 2020 by scientists from Chinese Academy of Sciences using innovative phase change material consisting of paraffin, expanded graphite and epoxy resin [35].

4. Conclusions

In the last years, aviation batteries have developed significantly, but the new designs still are not widely used in commercial manned aviation. In unmanned aerial vehicles lithium-ion batteries are the most used technology. Supercapacitors, although not very large in capacity, can provide a high power density. Thus, the supercapacitor and the rechargeable battery can operate in tandem. In the long run, lithium-oxygen (Li-O2) batteries are likely to be used. They are currently in the final stages of laboratory research. The main areas of research for lithium-ion rechargeable aviation batteries are reducing the mass and dimensions, increasing the service life, reducing the charging time, greater safety in their operation.

References

1. Donateo T., A. Ficarella, „Designing a hybrid electric powertrain for an unmanned aircraft with a commercial optimization software“, SAE International Journal of Aerospace, 2017, Issue 10, 1–11

2. Viswanathan, V., Epstein, A.H., Chiang, YM. et al. „The challenges and opportunities of battery-powered flight.“ Nature 601, 519–525 (2022). https://doi.org/10.1038/s41586-021-04139-1

3. Brelje B. J. , J. R. Martins, „Electric, hybrid, and turboelectric fixed-wing aircraft: A review of concepts, models, and design approaches“, Progress in Aerospace Sciences, Жолуме 104, 2019. https://doi.org/10.1016/j.paerosci.2018.06.004

4. Lain, M.J.; Brandon, J.; Kendrick, E., „Design Strategies for High Power vs. High Energy Lithium Ion Cells.“ Batteries 2019, 5, 64. https://doi.org/10.3390/batteries5040064

5. Abraham, K. M., „How Comparable Are Sodium-Ion Batteries to Lithium-Ion Counterparts?“, American Chemical Society Energy Letters, 2020.

6. Erickson E., E. Markevich, G. Salitra, D. Sharon, D. Hirshberg, de la Llave E, I. Shterenberg, A. Rosenman, A. Frimer, D. Aurbach, „Review-development of advanced rechargeable batteries: a continuous challenge in the choice of suitable electrolyte solutions.“ Journal of The Electrochemical Society , Volume 162, 2015. https://doi.org/10.1149/2.0051514jes

7. Pham H., H. Lee, E. Hwang, Y. Kwon, S. Song, „ Non-flammable organic liquid electrolyte for high-safety and high-energy density Li-Ion batteries.“, Journal of Power Sources, Volume 404, 2018. https://doi.org/10.1016/j.jpowsour.2018.09.075

8. Jamalpour S, M. Ghahramani , S. Ghaffarian, M. Javanbakht, „The effect of poly(Hydroxyl Ethyl Methacrylate) on the performance of Pvdf/P(Mma-Co-Hema) hybrid gel polymer electrolytes for lithium ion battery application.“, Polymer, Volume 195, 2020. https://doi.org/10.1016/j.polymer.2020.122427

9. Chai J, Z. Liu, J. Zhang, J. Sun, Z. Tian, Y. Ji, K. Tang, X. Zhou, G. Cui, „A superior polymer electrolyte with rigid cyclic carbonate backbone for rechargeable lithium ion batteries.“, ACS Applied Materials & Interfaces, Volume 9, 2017. https://doi.org/10.1021/acsami.7b02844

10. Famprikis T., P. Canepa, J. Dawson, M. S. Islam, Ch. Masquelier, „Fundamentals of inorganic solid-state electrolytes for batteries.“, Nature Materials, Volume 18, 2019. https://doi.org/10.1038/s41563-019-0431-3

11. Gin Hyung Chun, Joon Hyung Shim, Seungho Yu., „Computational Investigation of the Interfacial Stability of Lithium Chloride Solid Electrolytes in All-Solid-State Lithium Batteries.“, ACS Applied Materials & Interfaces 2022, 14 (1) , . https://doi.org/10.1021/acsami.1c22104

12. Park K, K. Kaup, A. Assoud, Q. Zhang, X. Wu, L. Nazar, „High-voltage superionic halide solid electrolytes for all-solid-state Li-Ion batteries.“, ACS Energy Letter, Volume 5, 2020. https://doi.org/10.1021/acsenergylett.9b02599

13. Umesh B., P. Ch. Rath, J. Patra, R. Hernandha, S. Majumder, X Gao, D. Bresser, S. Passerini, H. Lai, T. Chang, J Chang, „High-Li+-fraction ether-side-chain pyrrolidinium–asymmetric imide ionic liquid electrolyte for high-energy-density Si//Ni-rich layered oxide Li-ion batteries.“, Chemical Engineering Journal, Volume 430, 2022. https://doi.org/10.1016/j.cej.2021.132693

14. Ahniyaz A., I. de Meatza, A. Kvasha, O. Garcia-Calvo, I. Ahmed, M. F. Sgroi, M. Giuliano, M. Dotoli, M. Dumitrescu, M. Jahn, N. Zhang, „Progress in solid-state high voltage lithium-ion battery electrolytes.“, Advances in Applied Energy, Volume 4, 2021. https://doi.org/10.1016/j.adapen.2021.100070

15. Takeiri, F., A. Watanabe, K. Okamoto, D. Bresser, S. Lyonnard, B. Frick, A. Ali, Y. Imai, M. Nishikawa, M. Yonemura, T. Saito, K. Ikeda, T. Otomo, T. Kamiyama, R. Kanno, G. Kobayashi , „Hydride-ion-conducting K2NiF4-type Ba–Li oxyhydride solid electrolyte“, Nature Materials, Article in press, 2022. https://doi.org/10.1038/s41563-021-01175-0

16. Zhang H., Sh. Ju, G. Xia, X. Yu, „Identifying the positive role of lithium hydride in stabilizing Li metal anodes.“, Science Advances, Volume 8, 2022. https://www.science.org/doi/10.1126/sciadv.abl8245

17. Zhang H., Sh. Ju, G. Xia, X. Yu, „Identifying the positive role of lithium hydride in stabilizing Li metal anodes.“, Science Advances, Volume 8, 2022. https://www.science.org/doi/10.1126/sciadv.abl8245

18. Min W., L. Dechong, L. Zhuxin, Y. Tang, Y. Ding, L. Yuejiao, W. Zhong-Shuai, Zh. Hong. „α-MnO2 MWCNTs as an electrocatalyst for rechargeable relatively closed system Li-O2 batteries.“ Chemical Communications, Volume 57, 2021. https://doi.org/10.1039/D1CC03814A

19. Liu LL, Guo HP, Fu LJ, et al., "Critical advances in ambient air operation of nonaqueous rechargeable Li-air batteries", Small, Volume 17,2019. https://doi.org/10.1002/smll.201903854

20. Bazlen S., P. Heugel, O. Kessel, W. Commerell, J. Tübke, „Influence of charging protocols on the charging capability and aging of lithium-ion cells with silicon-containing anodes“, Journal of Energy Storage, Volume 49, 2022. https://doi.org/10.1016/j.est.2022.104044

21. Zhang Y., B. Wu, Ge Mu, Ch. Ma, D. Mu, F. Wu, „Recent progress and perspectives on silicon anode: Synthesis and prelithiation for LIBs energy storage“, Journal of Energy Chemistry, Volume 64, 2022, https://doi.org/10.1016/j.jechem.2021.04.013.

22. Kong D.,Sh.Wang, P.Ping, „A novel parameter adaptive method for state of charge estimation of aged lithium batteries“, Journal of Energy Storage, Volume 44, 2021

23. Vezzini A., „Lithium-ion battery management.“, Lithium-Ion Batteries Advance and Applications, Elsevier, 2014. https://doi.org/10.1016/B978-0-444-59513-3.00015-7

24. Yusof M., S. Toha, N. Kamisan, N. Hashim, M. Abdullah, „Battery cell balancing optimisation for battery management system.“, International Conference on Mechanical, Automotive and Aerospace Engineering, 2016. https://doi.org/10.1088/1757-899X/184/1/012021

25. Hemavathi S., „Overview of cell balancing methods for Li-ion battery technology“, Energy Storage, Volume 3, 2021, https://doi.org/10.1002/est2.203

26. Falcone, M.; Palka Bayard De Volo, E.; Hellany, A.; Rossi, C.; Pulvirenti, B., „Lithium-Ion Battery Thermal Management Systems: A Survey and New CFD Results.“, Batteries 2021, Volume 7, https://doi.org/10.3390/batteries7040086

27. Luo J., D. Zou, Y. Wang, Sh. Wang, L. Huang, „Battery thermal management systems (BTMs) based on phase change material (PCM): A comprehensive review“, Chemical Engineering Journal, Volume 430, Part 1, February, 2022. https://doi.org/10.1016/j.cej.2021.132741

28. Zhang Q., Jh. Niu, Zh. Zhao, Q. Wang, „Research on the effect of thermal runaway gas components and explosion limits of lithium-ion batteries under different charge states.“, Journal of Energy Storage, Volume 45, 2022. https://doi.org/10.1016/j.est.2021.103759

29. Kapp E. Andrew, D. Wroth, J. Chapin, „Analysis of Thermal Runaway Incidents Involving Lithium Batteries in U.S. Commercial Aviation”, Journal of the Transportation Research Board, Volume 2674, 2020 https://doi.org/10.1177/0361198120947711

30. Jiang Z.Y., H.B. Li, Z.G. Qu, J.F. Zhang, „Recent progress in lithium-ion battery thermal management for a wide range of temperature and abuse conditions”, International Journal of Hydrogen Energy, Volume 48, 2022. https://doi.org/10.1016/j.ijhydene.2022.01.008

31. Menale C, F. D'Annibale, B. Mazzarotta, R. Bubbico, „Thermal management of lithium-ion batteries: an experimental investigation“, Energy, Volume 182, 2019. https://doi.org/10.1016/j.energy.2019.06.017

32. Rao Z., S. Wang, G. Zhang, „Simulation and experiment of thermal energy management with phase change material for ageing LiFePO4 power battery“, Energy Conversion and Management, Volume 52, 2011. https://doi.org/10.1016/j.enconman.2011.07.009

33. Liu W., Z. Jia, Y. Luo, W. Xie, T. Deng, „Experimental investigation on thermal management of cylindrical Li-ion battery pack based on vapor chamber combined with fin structure“, Applied Thermal Engineering, Volume 162, 2019. https://doi.org/10.1016/j.applthermaleng.2019.114272

34. Huang Y, W. Cheng, R. Zhao, „Thermal management of Li-ion battery pack with the application of flexible form-stable composite phase change materials“, Energy Conversion and Management, Volume 182, 2019. https://doi.org/10.1016/j.enconman.2018.12.064

35. Luo X., Q. Guo, X. Li, Z. Tao, S. Lei, J. Liu, L. Kang, D. Zheng, Z. Liu, „Experimental investigation on a novel phase change material composites coupled with graphite film used for thermal management of lithium-ion batteries“, Renewable Energy, Volume 145, 2020. https://doi.org/10.1016/j.renene.2019.07.112

An algorithm optimizing the geometric distribution of the stations in aeronautical multilateration systems.

Marin Marinov, Velislava Peneva

"Georgi Benkovski" Bulgarian Air Force Academy, Faculty of "Aviation", Dolna Mitropolia, Bulgaria, Email: mmarinov@af-acad.bg

"Georgi Benkovski" Bulgarian Air Force Academy, Faculty of "Aviation", Dolna Mitropolia, Bulgaria, Email: velislava_p_peneva@abv.bg

Abstract: The way of receiving stations placement in aeronautical multilateration systems is a key to achieving better accuracy. In this paper an algorithm, utilizing genetic algorithm for stations distribution optimization, is presented. An objective function that has to be minimized by the algorithm is defined on the bases of the Cramer-Rao lower bound and the error ellipsoid. The studies results in the paper show that the proposed algorithm provides better stations placement in the sense of the average geometric factor than the standard distributions.

Keywords: *MLAT, optimal distribution, geometric factor, GDOP*.

1. Introduction

In spite of a temporary cut in the aviation sector in the past two years, the EASA has estimated that the number of flights will grow by more than 40% to 2040 in comparison to 2017 [1]. This will require new routes and most probably there will be no radar coverage for part of them. Furthermore, the number of small aircraft flights in lower flight levels has been on the rise and many of them use airfields which are not equipped with surveillance radars. A proper solution to the radar coverage problem is the usage of aeronautical multilateration (MLAT) systems. Besides en-route tracking of aircraft, these systems are also used at the airports including for the purpose of airport surface surveillance [2,3,4,5,6]. Such systems can also be used for the positioning of drones if the latter are equipped with suitable transponders. The study of these systems has been particularly intensive in the last two decades [3,6].

MLAT systems are independent or dependent positioning system that use a set of ground stations, which receive radio signals from the aircraft radio equipment [2,7,8]. Most often they use signals from on-board secondary surveillance radar transponders. In aeronautical MLAT systems localization of aircraft is based basically on two types of measurements – time of arrival and time difference of arrival (TDOA) [2,7,9,10]. The focus of this paper is on MLAT systems, using TDOA measurements of received signals. These measurements are used to calculate the differences of distance between aircraft and receiving stations. The very determination of aircraft position is based on the calculated differences in distance. An TDOA measurement between two stations localizes the aircraft on the surface of a hyperboloid with the two stations at foci. This is why such systems are called hyperbolic. Different aspects of MLAT systems, based on TDOA measurement, have been studied [7,9,10,11]. In this paper, systems are considered in terms of their accuracy.

There are many factors impacting on the accuracy of aircraft positioning in MLAT systems. Their influence could be summarized in two types of errors [10,11,12,13]. The first type is the errors of distance measurements, which combines the impacts of receiver quality, noise in the radio channel, signals specifications, etc. The second one is the dilution of precision due to the mutual geometric position of an aircraft and ground stations, or so called system geometry [9,10,11,12,13,14]. In the aeronautical surveillance systems, it is not only the values of errors that are important, but also the probability that they will be lower than a given limit. The paper deals with the confidence ellipsoid and the impact of the system geometry on the positioning accuracy.

The usage of the major semi axis of the error ellipsoid (confidence ellipsoid) as a parameter to estimate the influence of MLAT system geometry on its accuracy is justified in the paper. Based on this parameter, a criterion for optimizing the geometric distribution of the stations is proposed. An objective function, that has to be minimized by a proper distribution of the stations, is obtained. This function allows a distribution of the stations for which the Cramer-Rao lower bound (CRLB) is the smallest to be obtained. An algorithm, incorporating genetic algorithm for objective function minimizing, is proposed. Various study results are presented, which show that the algorithm can be used to find solutions in diverse scenarios and for different number of stations. In the paper, comparisons between the obtained optimal distributions of the stations and the most used standard distributions are made, where possible. The results of comparisons show that the Cramer-Rao lower bound is smaller for optimal distributions of the stations.

2. Accuracy of hyperbolic MLAT systems

For an aircraft localization, using hyperbolic MLAT systems, the time differences of arrival of at least three pairs of stations have to be measured. One of the stations is normally assumed as a reference one and TDOA of all other stations are measured in relation to it [17,18,19,20]. The measurements are not precise and each of them contains errors that possess Gaussian distribution with zero mean and some standard deviation σ [16,21]. Hence, it can only be estimated that the aircraft is within a given volume, called "Uncertainty volume", with given probability. The vector of measurements $\mathbf{\Delta\xi}$ is given by:

$$\mathbf{\Delta\xi} = c\mathbf{\Delta t} + \mathbf{n} = \mathbf{\Delta r} + \mathbf{n}, \quad (1)$$

where $\mathbf{\Delta t}$ is the vector of time differences of arrival of the signal in the stations; c is the speed of light; $\mathbf{\Delta r} = c\mathbf{\Delta t}$ is the vector of the differences of distances between the aircraft and the receiving stations and $\mathbf{n}$ is the vector of measurement errors, which obeys Gaussian distribution with zero mean and covariation matrix $\mathbf{R}_{\Delta\xi}$ [10,16,20,21]:

$$\mathbf{R}_{\Delta\xi} = \begin{Vmatrix} \sigma_2^2 + \sigma_1^2 & \sigma_1^2 & \vdots & \sigma_1^2 \\ \sigma_1^2 & \sigma_3^2 + \sigma_1^2 & \vdots & \sigma_1^2 \\ \cdots & \cdots & \cdots & \cdots \\ \sigma_1^2 & \sigma_1^2 & \vdots & \sigma_K^2 + \sigma_1^2 \end{Vmatrix}, \quad (2)$$

σ_i^2 is the variation of distance measurement errors of the i-th receiving station; K is the number of the stations.

The differences of distance between the aircraft and the receiving stations are expressed by the following equation:

$$\Delta r_{\mathrm{i}} = \frac{1}{c}\sqrt{(x-x_i)^2+(y-y_i)^2+(z-z_i)^2} - \frac{1}{c}\sqrt{(x-x_1)^2+(y-y_1)^2+(z-z_1)^2}, \quad (3)$$

where x_1, y_1, z_1 are the known coordinates of the reference station; x_i, y_i, z_i (i>1) are the known coordinates of non-reference stations; x, y, z are unknown coordinates of the aircraft.

The CRLB is the asymptotically achievable lower bound of the error covariance matrix for every unbiased estimator, based on the measurements (1) [10,16,17,18,20]:

$$E\left[\left(\boldsymbol{\theta}-\widehat{\boldsymbol{\theta}}\right)\left(\boldsymbol{\theta}-\widehat{\boldsymbol{\theta}}\right)^T\right] \geq \mathbf{F}^{-1}, \quad (4)$$

where $\boldsymbol{\theta} = [x, y, z]^T$ is the vector of the true aircraft position; $\widehat{\boldsymbol{\theta}} = [\hat{x}, \hat{y}, \hat{z}]^T$ is the vector of the estimated aircraft position; $E[\cdot]$ is the operation of the expectation value determination; $\mathbf{F}$ is Fisher information matrix (FIM).

The FIM is given by [10,18,20,22]:

$$\mathbf{F} = E\left[\left(\nabla_{\boldsymbol{\theta}}\ln\left(p(\Delta\boldsymbol{\xi}/\boldsymbol{\theta})\right)\right)\left(\nabla_{\boldsymbol{\theta}}\ln\left(p(\Delta\boldsymbol{\xi}/\boldsymbol{\theta})\right)\right)^T\right], \quad (5)$$

where $p(\Delta\boldsymbol{\xi}/\boldsymbol{\theta})$ is the likelihood function.

On the assumption that errors are with Gaussian distribution, the likelihood function will be:

$$p(\Delta\boldsymbol{\xi}/\boldsymbol{\theta}) = \frac{1}{\sqrt{2\pi|\mathbf{R}_{\Delta\xi}|}}\exp\left[-\frac{1}{2}(\Delta\boldsymbol{\xi}-\boldsymbol{\theta})^T\mathbf{R}_{\Delta\boldsymbol{\xi}}^{-1}(\Delta\boldsymbol{\xi}-\boldsymbol{\theta})\right]. \quad (6)$$

By substituting (6) in (5) the following equation for FIM is obtained:

$$\mathbf{F} = \mathbf{J}^T\mathbf{R}_{\Delta\boldsymbol{\xi}}^{-1}\mathbf{J}, \quad (7)$$

where $\mathbf{J} = \begin{Vmatrix} \frac{x-x_2}{r_2}-\frac{x-x_1}{r_1} & \frac{y-y_2}{r_2}-\frac{y-y_1}{r_1} & \frac{z-z_2}{r_2}-\frac{z-z_1}{r_1} \\ \frac{x-x_3}{r_3}-\frac{x-x_1}{r_1} & \frac{y-y_3}{r_3}-\frac{y-y_1}{r_1} & \frac{z-z_3}{r_3}-\frac{z-z_1}{r_1} \\ \cdots & \cdots & \cdots \\ \frac{x-x_K}{r_K}-\frac{x-x_1}{r_1} & \frac{y-y_K}{r_K}-\frac{y-y_1}{r_1} & \frac{z-z_K}{r_K}-\frac{z-z_1}{r_1} \end{Vmatrix}$; $r_i = \sqrt{(x-x_i)^2+(y-y_i)^2+(z-z_i)^2}$ is the distance between the aircraft and i-th station.

It can be accepted that the variances σ_i^2 of measurement errors in each station are one and the same [10,18,20]. Thus using (7) the following form of the CRLB is obtained:

$$\mathbf{F}^{-1} = \sigma^2\left(\mathbf{J}^T\begin{Vmatrix} 0.75 & 0.25 & \vdots & 0.25 \\ 0.25 & 0.75 & \vdots & 0.25 \\ \cdots & \cdots & \cdots & \cdots \\ 0.25 & 0.25 & \vdots & 0.75 \end{Vmatrix}\mathbf{J}\right)^{-1} = \mathbf{G}\sigma^2, \quad (8)$$

where

$$(9)\quad \mathbf{G} = \left(\mathbf{J}^T \begin{Vmatrix} 0.75 & 0.25 & \vdots & 0.25 \\ 0.25 & 0.75 & \vdots & 0.25 \\ \cdots & \cdots & \cdots & \cdots \\ 0.25 & 0.25 & \vdots & 0.75 \end{Vmatrix} \mathbf{J} \right)^{-1}.$$

The elements of the matrix **J** depend only on the spatial distribution of the aircraft and stations and consequently the influence of the system geometry on the CRLB is taken into account through the matrix **G**. The axes of the error ellipsoid are determined by the eigendecomposition of a matrix $\mathbf{F^{-1}}$:

$$(10)\ \mathbf{F}^{-1} = \sigma^2 \mathbf{Q\Lambda Q}^{-1},$$

where $\mathbf{\Lambda}$ is the diagonal matrix whose diagonal elements are the corresponding eigenvalues of **G** and **Q** is the matrix whose columns are the eigenvectors of **G**:

$$(11)\ \mathbf{\Lambda} = \mathbf{Q}^{-1}\mathbf{GQ} = \begin{Vmatrix} \lambda_1 & 0 & 0 \\ 0 & \lambda_2 & 0 \\ 0 & 0 & \lambda_3 \end{Vmatrix}.$$

The elements $\lambda_1, \lambda_2, \lambda_3$ in (11) are the eigenvalues of **G** and their square roots are the values of the semi axes of the error ellipsoid. In the aeronautical MLAT systems it's necessary to determine the error ellipsoid at a certain level of probability. The values of the semi-axes of an ellipsoid at level of probability *P* are obtained by multiplying the eigenvalues in (11) by a factor of *k*:

$$(12)\ k = F_{\chi^2}^{-1}(P, 3),$$

where $F_{\chi^2}^{-1}(\cdot)$ is the inverse function of the cumulative distribution function (CDF) of the chi-square distribution, $F_{\chi^2}(x, \nu) = \int_0^x \frac{t^{\frac{\nu}{2}-1} e^{-\frac{t}{2}}}{2^{\frac{\nu}{2}}\,\Gamma\left(\frac{\nu}{2}\right)} dt$ is the CDF of the chi-square distribution with ν degrees of freedom; $P = F_{\chi^2}(k, 3)$ is the given probability level.

Using (11) and (12) the semi-axes of the error ellipsoid are obtained:

$$(13)\ a = \sqrt{k\lambda_1},\ \ b = \sqrt{k\lambda_2},\ \ c = \sqrt{k\lambda_3}.$$

As the elements of the matrices, **J**, **G** and $\mathbf{\Lambda}$ are dimensionless it's convenient to use relative (normalized) values of the coordinates and distances instead of their absolute ones. Normalization is done by a specific dimension of the area in which the stations are placed.

In Fig. 1 the error ellipsoids at two levels of probability for two aircraft positions and the standard square configuration of stations with coordinates (0,0,0), (-1,-1,0), (-1,1,0), (1,1,0), (1,-1,0) are shown.

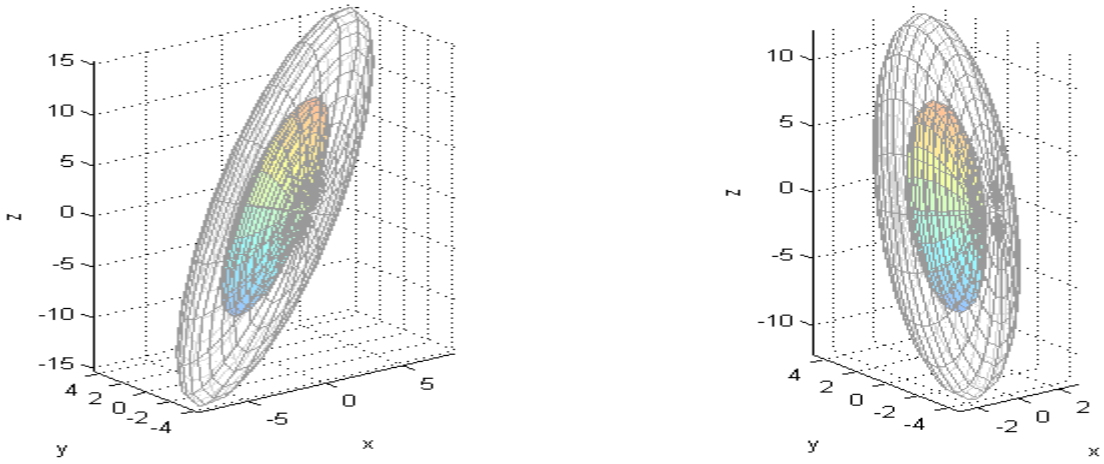

a) *Aircraft position 1.* b) *Aircraft position 2.*

Figure 1. Error ellipsoids at levels of probability P=0.5 and P=0.95.

The relative coordinates of the first position of the aircraft are (1.32, 0.48, 1), whereas the relative coordinates of the second position are (0.34, 0.94, 1). In Fig. 1 the inner ellipsoids are at probability level 0,5, whereas the outer ones are at probability level 0.95. Despite the fact that the heights of the aircraft at the two positions are equal, the values and the orientations of the ellipsoids axes are different.

The values of the ellipsoids axes (*a*, *b*, *c*) and the angles between the semi-major axes and z-axis of coordinate system (γ) are summarized in Table 1.

Table 1. *Error ellipsoids parameters*.

Probability levels	P = 0,5				P = 0,95			
Ellipsoid parameters	*a*	*b*	*c*	γ [deg]	*a*	*b*	*c*	γ [deg]
Aircraft position 1	9.64	2.10	1.47	28.87	17.52	3.83	2.66	28.87
Aircraft position 2	7.13	1.36	1.67	18.36	12.96	2.47	3.03	18.36

Table 1 shows that the semi-axes *a* and *b* of ellipsoids for the first aircraft position are greater than these of ellipsoids for the second aircraft position, whereas the semi-axes *c* for the position 1 are smaller than that for the position 2. The inclination of the semi-major axis with respect to the z-axis is greater for the first aircraft position.

The values of the ellipsoid axes in meters are obtained by multiplying the right sides of the equations (11) with the standard deviation of distance measurements σ:

(14) $a[m] = \sigma\sqrt{k\lambda_1},\ \ b[m] = \sigma\sqrt{k\lambda_2},\ \ c[m] = \sigma\sqrt{k\lambda_3}.$

Because of different orientations of the error ellipsoid, the value of the semi-major axis is accepted to be the measure of the system geometry impact on the accuracy of the system in this paper. Thus it's guaranteed that probability level of errors is at least 0.95. For convenience the semi-major axis of the error ellipsoid is called geometric factor (GF) further in this paper.

3. Algorithm optimizing geometric distribution of the stations

Before synthesizing any optimization algorithm an optimality criterion has to be defined. Usually only a specific sector of the airspace is of interest to the aeronautical surveillance systems. This sector is defined by a horizontal region with specific shape and a certain range of heights. It has been shown above that errors are different at the different points of the sector and this is why the average GF in the horizontal region at given height is proposed as an optimality criterion.

Equations (7) - (13) show that it is impossible to derive a direct relation between the GF and the coordinates of the points in the surveillance sector, which makes it impossible to average the GF through integration. An algorithm, using the values of the GF at discrete points in the sector, is used to find the objective function. First a grid of N_p points in the horizontal region is generated. In the next step the geometric factors GF_i of all grid points are calculated. In the last step the average GF is obtained:

(15) $f_{obj} = \frac{\sum_{i=1}^{N_p} GF_i}{N_p}$.

The equation (15) describes mathematically the objective function that has to be minimized by a proper distribution of the stations. As this is a non-analytic function it's appropriate to use a genetic algorithm [23,24,25,27,28]

The optimal distribution of the stations, for which the function (15) has minimal value, is obtained by the algorithm shown in Fig. 2.

The horizontal region of the surveillance sector is defined by the coordinates (x_i^{SR}, y_i^{SR}) of its vertices. The minimal and maximal values of these coordinates are obtained:

(16) $x_{min}^{SR} = min(x_i^{SR}); \quad x_{max}^{SR} = max(x_i^{SR}); \quad y_{min}^{SR} = min(y_i^{SR}); \quad y_{max}^{SR} = max(y_i^{SR})$.

Using the obtained coordinates a rectangle with vertices $(x_{min}^{SR}, y_{min}^{SR})$, $(x_{min}^{SR}, y_{max}^{SR})$, $(x_{max}^{SR}, y_{max}^{SR})$, $(x_{max}^{SR}, y_{min}^{SR})$ is formed. A grid of N_g evenly distributed points in the rectangle is generated and after that the N_p points of them, which are inside the horizontal region are chosen to calculate the objective function.

The deployment area is defined as a convex polygon with the coordinates (x_i^{DA}, y_i^{DA}) of its vertices. The sides of the polygon are the boundaries of the deployment zone, each of which is a part of a straight line described by the following general equation:

(17) $y = k_i x + c_i, \quad 1 \leq i \leq N_{DA}$,

where k_i and c_i are constants and N_{DA} is the number of the vertices.

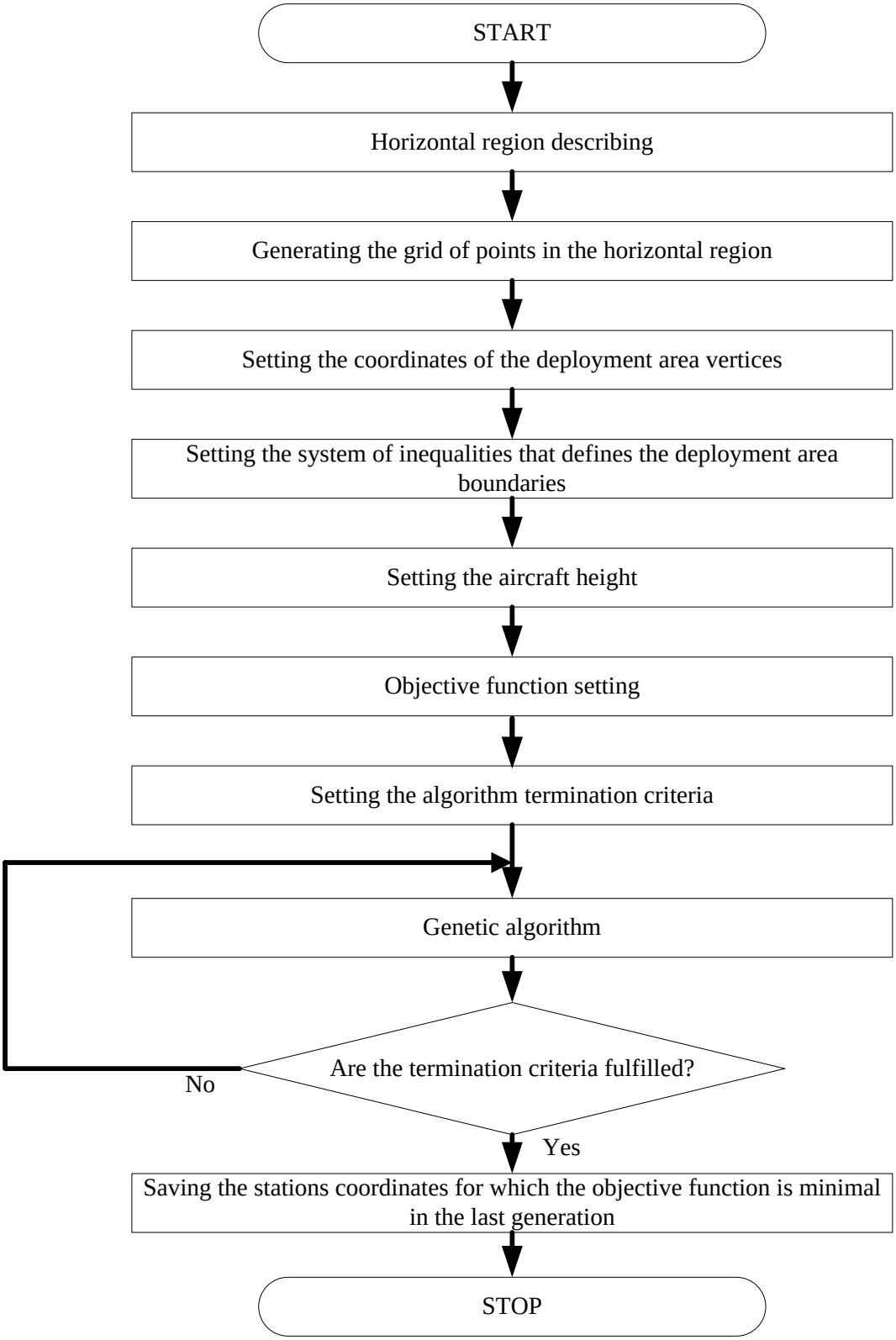

Figure 2. *Algorithm optimizing geometric distribution of the stations*.

The constants in (17) are obtained by the following equations:

$$(18)\quad \begin{matrix} k_i = \frac{y_{i+1}^{DA} - y_i^{DA}}{x_{i+1}^{DA} - x_i^{DA}}; & c_i = y_i^{DA} - k_i x_i^{DA}; & i \le 1 \div N_{DA} - 1; \\ k_{N_{DA}} = \frac{y_1^{DA} - y_{N_{DA}}^{DA}}{x_1^{DA} - x_{N_{DA}}^{DA}}; & c_i = y_{N_{DA}}^{DA} - k_{N_{DA}} x_{N_{DA}}^{DA} & \end{matrix} .$$

If the *y*-coordinates of the straight line are smaller than the *y*-coordinates of the points inside the deployment area, than the following inequality is fulfilled:

(19) $y \ge k_i x + c_i \implies k_i x - y \le -c_i.$

If the *y*-coordinates of the straight line are greater than the *y*-coordinates of the points inside the deployment area, than the following inequality is fulfilled:

(20) $y \le k_i x + c_i \implies -k_i x + y \le c_i.$

The inequalities (19) and (20) can be summarized in one:

(21) $-k_i l_i x + l_i y \le l_i c_i.$

where the value of l_i is 1 if the inequality (20) is valid and its value is -1 if the inequality (19) is valid.

Taking in account the constraints of all sides of the polygon a system of linear inequalities is found:

(22) $\mathbf{A\eta} \le \mathbf{c}_l$,

where: $\mathbf{A} = \|-\mathbf{k}_l \quad \mathbf{l}\|$; $\boldsymbol{\eta} = \|x \quad y\|^T$; $\mathbf{c}_l = \|c_1 l_1 \quad c_2 l_2 \quad \cdots \quad c_{N_{DA}} l_{N_{DA}}\|^T$;

$\mathbf{l} = \|l_1 \quad l_2 \quad \cdots \quad l_{N_{DA}}\|^T$ and $\mathbf{k}_l = \|k_1 l_1 \quad k_2 l_2 \quad \cdots \quad k_{N_{DA}} l_{N_{DA}}\|^T$.

The inequalities (22) define the linear constraints for the genetic algorithm that control the forming of individuals in each generation. Thus it's guaranteed that each station is inside the desired area.

Two termination criteria are set in the algorithm:

1. The algorithm stops if the average relative change in the best fitness function value over 50 generations is less than or equal to 10^{-5}.
2. The algorithm stops if the number of generations in genetic algorithm reaches 100.

In every step the genetic algorithm generates a new population with size of 200 individuals. Two individuals of each generation, called elite, are guaranteed to survive to the next generation. It is set that 60% of the individuals, not including the elite children, in the next generation are produced by crossover. It is set that 20% of the individuals migrate to a different subpopulation. The genetic algorithm creates a random initial population with a uniform distribution.

The algorithm finds the optimal distribution of the stations for which the value of objective function (15) is minimal. In all studies that have been done the algorithm finds a solution and the termination of algorithm is always due to the fulfilment of the first criterion.

4. Results and discussions

Some results of studies about GF for different shapes of the deployment area and of the surveillance region are presented in the paper. Firstly, studies about a square shaped deployment area have been conducted, which allows comparison between the obtained optimal distributions of the stations and the standard distributions. A normalizing is done by dividing all coordinates, distances and heights by the half of the length of the side of the square deployment area. Thus the deployment area is described by the vertices with relative coordinates (-1,-1), (-1,1), (1,1), (1,-1). The horizontal surveillance region is a square with relative coordinates of the vertices (-1.5,-1.5), (-1.5,1.5), (1.5,1.5), (1.5,-1.5). A grid of 900 equally distributed points inside this region is generated to calculate the objective function.

Obtained optimal distributions of stations for 3 different heights *h* are shown in Fig. 3. The standard Y and triangle distributions are also shown in the figure.

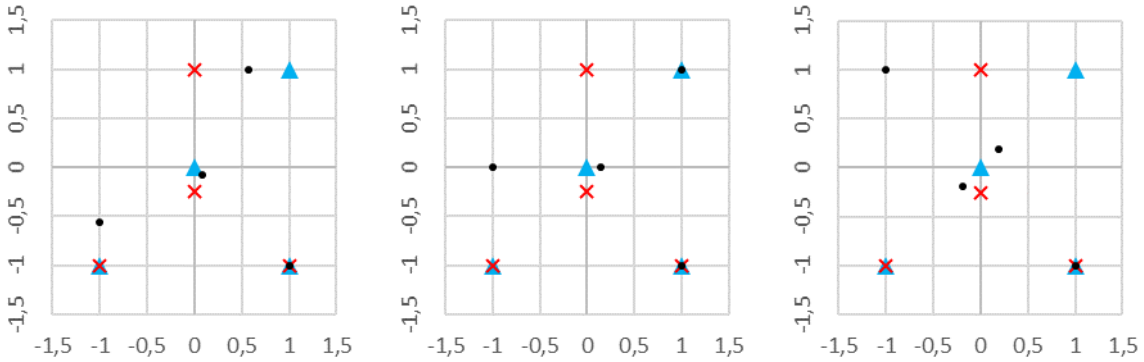

a) *h*=0.01 b) *h*=0.3 c) *h*=2

Figure 3. Optimal (•), Y (×) and triangle (◢) distributions of 4 stations.

The results of studies show that the optimal distribution for each height is different. Whereas the optimal distributions for *h*=0.01 and *h*=0.3 are similar to rotated Y-distribution, the optimal distribution for *h*=2 is totally different from standard distributions. To compare the different distributions some studies of the GF for different relative heights have been done.

The contours of GF at height 2 for different distributions are shown in Fig. 4. The deployment area is also shown with red dashed line as well as the surveillance region is shown as a gray polygon.

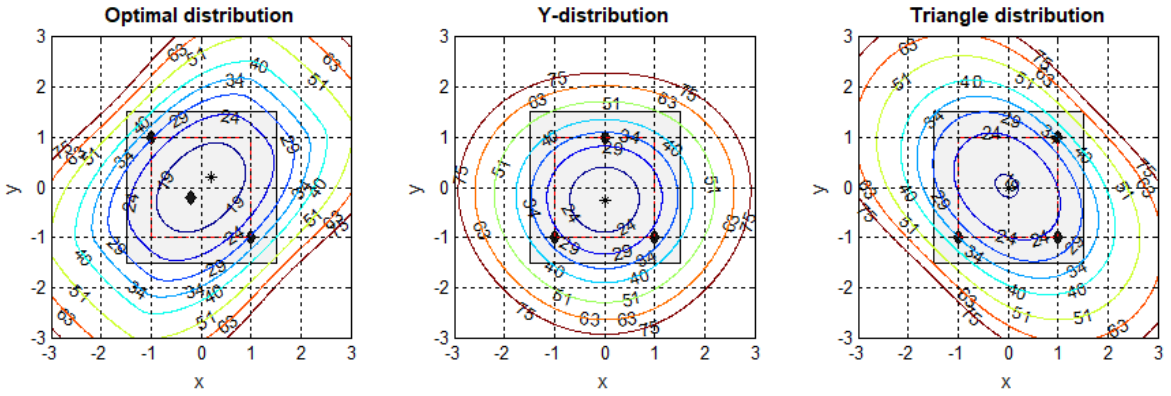

Figure 4. Geometric factor for different distributions of 4 stations at h=2.

A diversity of contours shapes can be seen for the different distributions shown in Fig. 4 The area of the contour at level of GF 29 is the smallest for the optimal distribution and the greatest for the Y-distribution.

The average GF in the surveillance region is used as a measure of the accuracy provided by the distributions. The improvement of the average GFs of the optimal distributions in comparison to the standard distributions of 4 stations is shown in Fig. 5. The improvement is calculated as a ratio between the average GF of an optimal distribution and corresponding average GF of a given standard distribution.

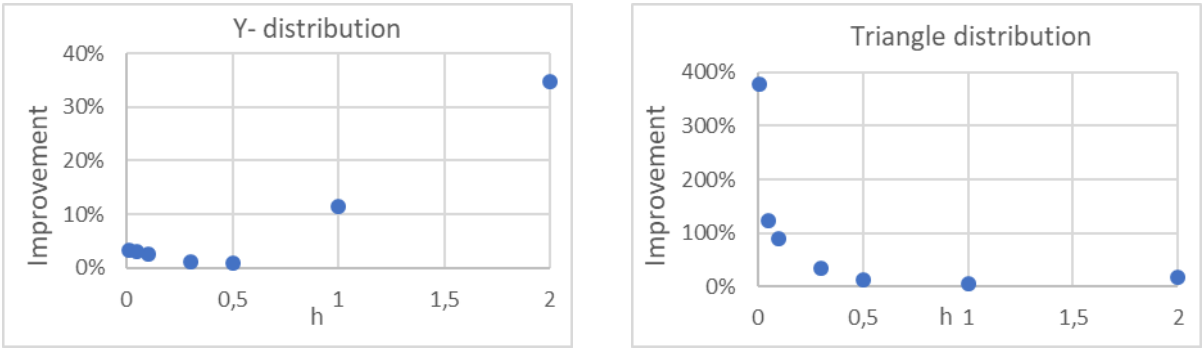

Figure 5. *Average GF of optimal distributions of 4 stations compared to standard distributions*.

The improvement in the average GF, compared to the triangle distribution, is greater at the greater heights, whereas compared to the Y-distribution it is greater at the smaller heights. There is a minimal improvement of 0.96% over the Y-distribution at height 0.5 whereas the maximal improvement is 34.76% at height 2. For the triangle distribution the minimal improvement is 4.81% at height 1 whereas the maximal improvement is over 350% at height 0.01.

Similar researches have been done about a MLAT system with 5 receiving stations. A part of the results is shown in Fig. 6.

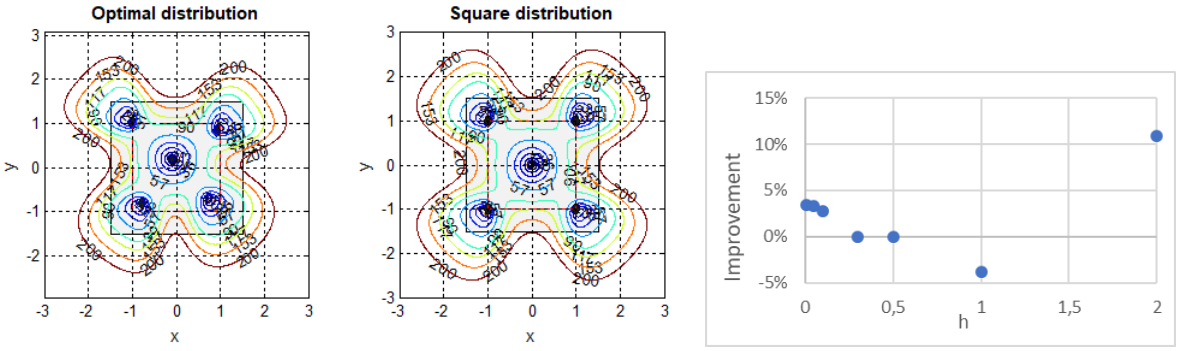

Figure 6. *The GF at h=0.05 and average GF of optimal distributions of 5 stations compared to square distribution*.

As a whole the improvement in the average GF for the optimal distributions compared to the standard square distribution is less than in the cases of 4 stations. The study results proved that as a whole the

optimal distributions, obtained by the proposed algorithm, provide better GF in comparison to the standard distributions even in the case of a square deployment area and a square surveillance region.

In many cases there are constraints on the shape of the deployment area due to the characteristics of the terrain, some infrastructure problems, ect., which in many practical cases lead to non-square shape of the area. Some studies of GF for different shapes of the deployment area and the same square surveillance region as in the previous cases have been done. The results for a triangle deployment area with vertices (-1,-0.8), (0.1,0.9), (1,-1) and 4 stations are shown in Fig. 7. To obtain the standard distributions, first a square with maximal possible side, inscribed in the deployment area, is found and next the stations are deployed in the Y and triangle configurations inside it.

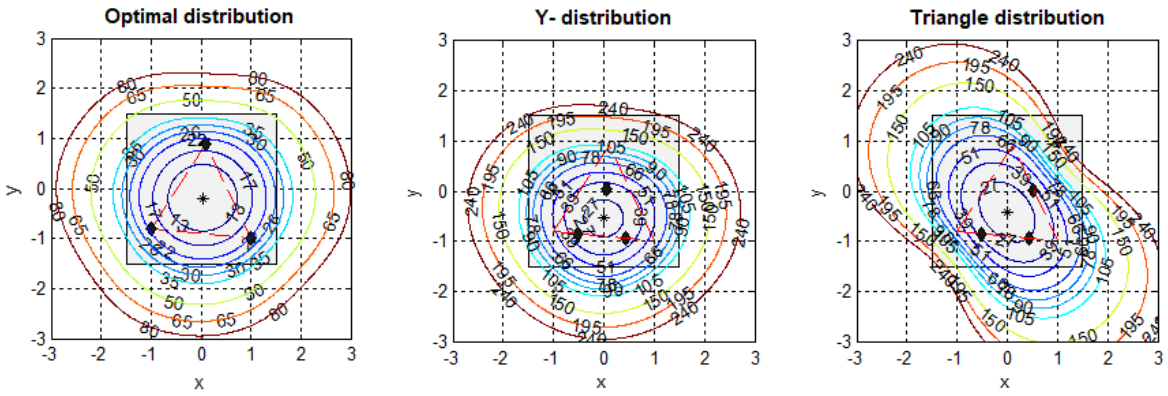

Figure 7. *Geometric factor for 4 stations in a triangle deployment area at h=1.*

The figure shows that the values of the contours inside the surveillance region are smallest for the optimal distribution.

The improvements of the average GFs of the optimal distributions in comparison to the standard distributions of 4 stations for the triangle deployment area are shown in Fig. 8.

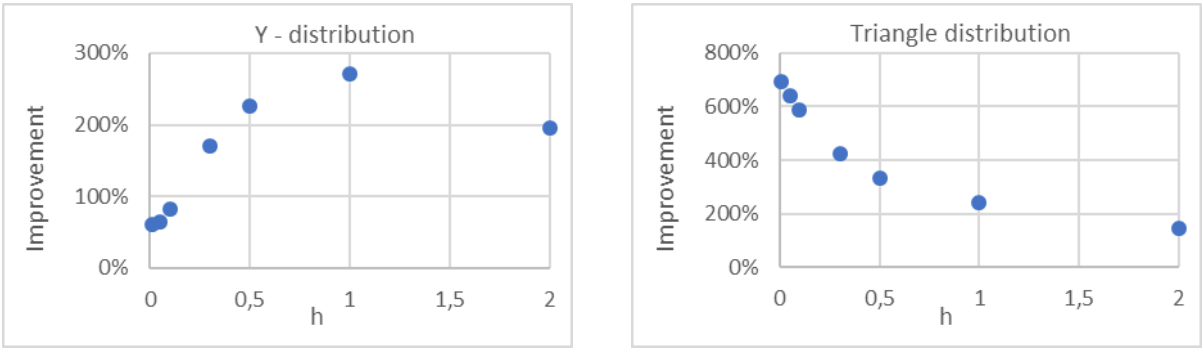

Figure 8. *Average GF of optimal distributions of 4 stations compared to standard distributions for a triangle deployment area.*

The improvement in the average GF, compared to the triangle distribution, is greater at the smaller heights, whereas compared to the Y-distribution it is greater at the middle heights. The minimal

improvement is 60% over the Y-distribution at height 0.01 and it is 145% over the triangle distribution at height 2. The maximal improvement is 270.8% over the Y-distribution at height 1 and it is 694.3% over the triangle distribution at height 0.01.

Researches of a MLAT system with 6 receiving stations for the triangle deployment area have been done. The results of comparison between the average GFs of the optimal distributions with 4, 5 and 6 stations are shown in Fig. 9. The average, minimal and maximal improvements in the average GF in the case of 5 stations over the case of 4 stations are respectively 24.44%, 11.44% and 33.02%. These improvements for the case of 6 stations over the case of 4 stations are respectively 38.24%, 26.32% and 46.52%. The results of the comparison between the case of 6 and the case of 5 stations show that the minimal improvement in the average GF is 12.93%, the maximal improvement is 22.70% and the average improvement is 18.36%. Consequently, the more stations are used the less the average GF is.

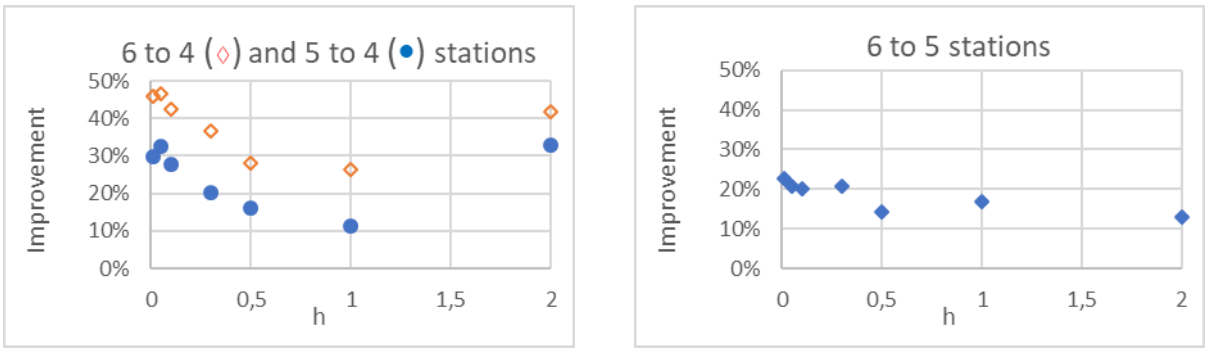

Figure 9. Comparison between the average GFs of the optimal distributions of 4, 5 and 6 stations for a triangle deployment area.

Each increase in the number of stations leads to the less average improvement, compared to the previous one which makes the usage of more than 6 stations in the regarded case inappropriate. Studies for other shapes of the deployment area have been done and obtained results lead to the same conclusions as that done above.

In some cases, there is no need to provide good accuracy in all directions around the MLAT system but only in a particular sector of the airspace. Studies for different shapes of the surveillance region have been done using the square deployment area, described before. The results show that in all cases of optimal distributions of 4 and 5 stations there is improvement over the standard distributions. The minimal improvement is over 16% whereas the maximal improvement is more than 220%. The conclusions about the impact of the number of stations are the same as in the previous case.

Sets of different shapes of surveillance region and deployment area have been studied. The part of the obtained results is shown in the paper. In Fig. 10 GF at height 1 for MLAT systems with 4, 5 and 6 stations in case of arbitrary deployment area and a trapezoidal surveillance region are shown.

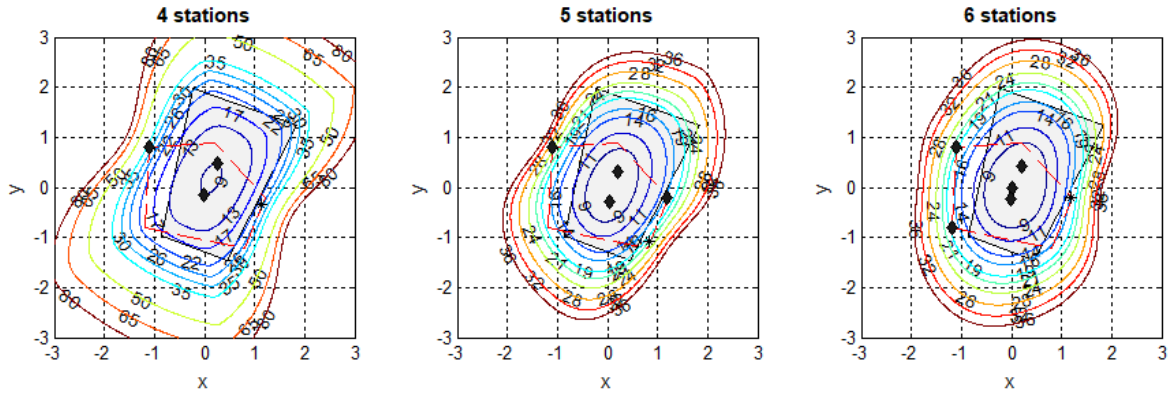

Figure 10. Geometric factor at h=1 for an arbitrary deployment area and a trapezoidal surveillance region.

The figure shows that the values of the contours inside the surveillance region are smallest when 6 stations are used and they are largest when 4 stations are used.

The results of comparison between the average GFs of the optimal distributions with 4, 5 and 6 stations are shown in Fig. 11.

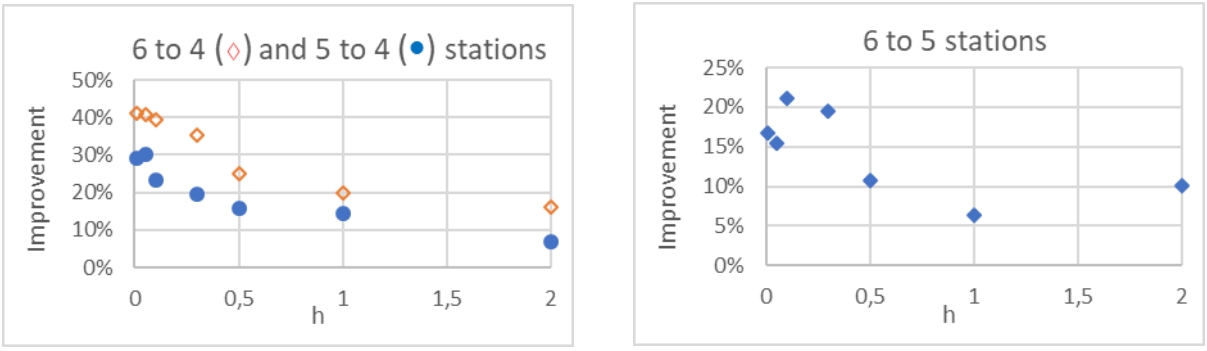

Figure 11. Comparison between the average GFs of the optimal distributions of 4, 5 and 6 stations for an arbitrary deployment area and a trapezoidal surveillance region.

The average, minimal and maximal improvements in the average GF in the case of 5 stations over the case of 4 stations are respectively 19.87%, 6.73% and 29.98%. The corresponding improvements for the case of 6 stations over the case of 4 stations are respectively 31.07%, 16.17% and 40.97%. The results of the comparison between the case of 6 and the case of 5 stations show that the minimal improvement in the average GF is 6.34%, the maximal improvement is 21.07% and the average improvement is 14.28%. The improvement in GF when the number of stations is increased from 5 to 6 is smaller than the improvement in the case of using 5 stations instead of 4 stations. The results show that the more stations are used the less the average GF is. The studies of a MLAT system with 7 stations have been done. The results show that the increase of the number of stations to 7 leads to the less average improvement, which makes the usage of more than 6 stations in the regarded cases inappropriate.

5. Conclusions

In this paper an algorithm optimizing deployment of MLAT system stations is proposed. The Cramer-Rao lower bound is used to formulate an optimality criterion. The semi-major axis of the error ellipsoid is defined as a geometric factor that takes into account the impact of system geometry on the accuracy of the aircraft positioning. A non-analytic objective function that finds the average geometric factor inside a given horizontal surveillance region at certain height is derived. The proposed algorithm minimizes this function utilizing a genetic algorithm. A system of inequalities that defines the constraints on population of each generation in genetic algorithm is derived. The algorithm doesn't impose any restrictions on the shapes of the stations deployment area and surveillance region as long as they are properly defined. This algorithm can be used for deployment of different number of stations.

The various studies of the algorithm are presented in the paper. The results for different shapes of the stations deployment area and surveillance region are obtained. Comparison to the standard distributions of stations shows that the proposed algorithm provides better stations placement in the sense of the average geometric factor inside a given surveillance region. The studies have proved that the algorithm works steadily and always finds a proper solution.

As a final conclusion it can be stated that, although the algorithm has been synthesized for aircraft in the air, it is not hard to be modified for aircraft on the airport surface.

References

1. European Aviation Environmental Report 2019, EASA, EEA, EUROCONTROL, 2019, ISBN 978-92-9210-214-2.

2. Ning Xu; Rick Cassell et al., „Performance assessment of Multilateration Systems - a solution to nextgen surveillance", 2010 Integrated Communications, Navigation, and Surveillance Conference (ICNS 2010), Herndon, VA, U.S.A., 11-13 May 2010, p. D2-1-D2-8, ISBN 978-1-4244-7459-2.

3. Mantilla-Gaviria. I., M. Leonardi, G. Galati,·and et al., „Localization algorithms for multilateration (MLAT) systems in airport surface surveillance", Signal, Image and Video Processing, Springer-Verlag London, 2014, ISSN 1863-1703.

4. Rayapu M., S. Talari, G. Indira Priya Darshini, „Multilateration With ADS-B a Boon in Civil Aviation Application", International Conference on Electrical, Electronics, Communication, Computer and Optimization Techniques (ICEECCOT), pp. 545-550, February 2017, ISBN:978-1-5386-2361-9

5. Penev P., „Possibilities for increasing the air traffic management efficiency in the area of aviation facilities ",6th International conference "Smart defence solutions and technologies, 2012, p. I-101- I-111, ISSN 1312-2916 (In Bulgarian).

6. Penev P., „Surface movement guidance and control system – conception and development",Chief Information Officer journal, ICT Media, Sofia, 2011, ISSN 1312-5605 (In Bulgarian).

7. Badgaiyan T. D., R. Tiwari, „A review paper on localization algorithm for multilateration system", International journal for research in technological studies Vol. 5, Issue 5, April 2018, ISSN (online): 2348-1439, pp. -3-6.

8. Badgaiyan T. D., R. Tiwari, „Localization Algorithm for Multilateration System Using Hyperbolic Localizations", International Journal of Advanced Research in Electronics and

9. Castro A. C. M. F, „Optimisation of Ground Stations Location in Aeronautical Multilateration Systems", Thesis to obtain the master of science degree in electrical and computer engineering, Lisbon, Portuguese, 2016

10. El-Ghoboushi M., A. Ghuniem, A. H. Gaafar, H. E. D. Abou-Bakr „Geometry effect on a multilateration air traffic surveillance system performance", Japan-Africa Conference on Electronics, Communications and Computers (JAC-ECC), 2017, pp. 136-143, ISBN:978-1-5386-1359-7

11. Fresno J. M., G. Robles, J. Martínez-Tarifa and et al., „Survey on the Performance of Source Localization Algorithms“, Survey on the performance of source localization algorithms. Sensors, 17 (11), 2017, ISSN 1424-8220

12. Banelli P., „Non-Linear Transformations of Gaussians and Gaussian-Mixtures with implications on Estimation and Information Theory“, IEEE Transactions on Information Theory Vol. 59, Issue: 4, April 2013, ISSN: 1557-9654

13. Bar-Shalom Y., X. Rong Li, and T. Kirubarajan, „Estimation with Applications to Tracking and Navigation“, John Wiley & Sons, Inc., 2001, ISBN 9780471221272.

14. Bedin, D. „Localization with Several Instants of Signal Transmission in Multilateration Systems“, IFAC-PapersOnLine, Vol. 51 Issue 32, pp. 659-662, 2018, ISSN: 2405-8963

15. Bishop A. N., B. Fidan, B. D. O. Anderson, K. Dogancay, P. N. Pathirana, „Optimality analysis of sensor-target localization geometries“, Automatica, Vol. 46, Issue 3, pp. 479-492, March 2010, ISSN: 0005-1098.

16. Bishop A. N., B. Fidan, B. D. O. Anderson, P. N. Pathirana, K. Dogancay, „Optimality analysis of sensor-target geometries in passive localization: Part 1 - Bearing-only localization“, IEEE 3rd International conference on intelligent sensors, sensor networks and information processing (ISSNIP), Melbourne, Australia, December 2007, ISBN:978-1-4244-1501-4.

17. Galati G., M. Leonardi, J. V. Balbastre-Tejedor, I. A. Mantilla-Gaviria, „Time-difference-of-arrival regularised location estimator for multilateration systems“, IET Radar, Sonar & Navigation, vol. 8, no. 5, pp. 479–489, Jun. 2014, ISSN 1751-8792

18. Isaacs J.T., D.J. Klein, and J.P. Hespanha, „Optimal Sensor Placement For Time Difference of Arrival Localization“, Proc. of 48th IEEE Conf. on Decision and Control, Shanghai, China, Dec. 2009, p. 7878-7884, ISBN 978-1-4244-3871-6

19. Jin B., X. Xu, T. Zhang, „Robust time-difference-of-arrival (TDOA) localization using weighted least squares with cone tangent plane constraint“, Journal Sensors Vol. 18 Issue 3, March 2018, MDPI, China, EISSN 1424-8220

20. Tichonov, V. I., V. N., Harisov, „Statistical analysis and synthesis of radio engineering devices and systems“, Moscow: Radio i svyaz' Publ, 1991, ISBN 5-256-00789-0. (in Russian)

21. Kaune R., „Accuracy studies for TDOA and TOA localization“, 15th International Conference on Information Fusion, IEEE Singapore, 2012, pp. 408-415, ISBN:978-0-9824438-4-2.

22. Bishop A. N., B. Fidan, B. D. O. Anderson, P. N. Pathirana, K. Dogancay, „Optimality analysis of sensor-target geometries in passive localization: part 2 - Time-of-arrival based localization“, IEEE 3rd International conference on intelligent sensors, sensor networks and information processing (ISSNIP), Melbourne, Australia, December 2007, ISBN:978-1-4244-1501-4.

23. Arkhipov D., D. Wu, T. Wu, „A parallel genetic algorithm framework for transportation planning and logistics management“. IEEE Access Vol. 8, pp. 106506 – 106515, May 2020, eISSN: 2169-3536

24. Alia L., A. Italiano, F. Pozzi, „Advanced Tools to analyze the expected performance of multilateration and wide area multilateration“, Tyrrhenian International Workshop on Digital Communications - Enhanced Surveillance of Aircraft and Vehicles (TIWDC/ESAV) 2014, pp. 82-86, ISBN:978-1-4799-3094-4

25. Al-Oqaily AT, G. Shakah, „Solving non-linear optimization problems using parallel genetic algorithm“, International Conference on Computer Science and Information Technology (CSIT), Amman, pp. 103–106, 2018, DOI:10.1109/CSIT.2018.8486176

26. Bo L., Z. Xuejun, Z. Shuang, „Multilateration station location study based on genetic algorithm“, 2010 International Symposium on Computational Intelligence and Design (ISCID), Hangzhou, October, pp. 60-63, 2010, ISBN:978-1-4244-8094-4.

27. Ruiz-Mojica R. F., I. A. Mantilla-Gaviria and at al., „A genetic algorithm and local search for the automated calculation of dilution of precision of mode-S multilateration systems at airports“, Tyrrhenian International Workshop on Digital Communications - Enhanced Surveillance of Aircraft and Vehicles, October 2011, pp. 259-263, ISBN:978-88-903482-3-5

Detecting and Tracking Asteroids in The International Astronomical Search Collaboration Science Program

Milen Simeonov, Veselka Radeva

Georgi Benkovski Bulgarian Air Force Academy, Faculty of Aviation, Dolna Mitropoliya, Bulgaria, Email: msimeonov@af-acad.bg

Nikola Vaptsarov Bulgarian Naval Academy, Naval Astronomical Observatory and Planetarium, Varna, Bulgaria, Email: v.radeva@naval.eu

Abstract: The article presents the work and the results of a group of lecturers, teachers, cadets and students in the International Astronomical Search Collaboration science program. The main stages of the astrometric processing of the astronomical images, in which, asteroids are detected and followed up, are addressed. With the help of a NASA's Jet Propulsion Laboratory software, are calculated the orbital elements and are presented the orbital diagrams of the new asteroids, discovered by the teams of Georgi Benkovski Bulgarian Air Force Academy.

Keywords: *IASC, asteroids, astronomical observations, orbital elements, Astrometrica*

1. Introduction

The Astronomical Community carries out research in order to study and understand the nature of the astronomical objects, as well as, protect the humankind from cosmic dangers. One of those dangers, which life on our planet has faced, is collisions with asteroids and comets. These objects date back to the formation of our Solar System, 4.6 billion years ago. One of the largest planetary catastrophes was caused by an asteroid, which fell in the area of Yucatán, Mexico. At that time, 64 million years ago, 95% of Earth's biosphere had vanished. Astronomers who study the Minor Bodies in the Solar System organize, manage and participate in various scientific and research programs. One of the most successful programs is the International Astronomical Search Collaboration (IASC). This scientific program enables cadets, students and pupils from universities and colleges to make real astronomical discoveries and search for and follow up asteroids, that are already known. Over 1 113 500 asteroids had been discovered by the end of 2021. The discoveries were made by professional astronomers, amateur-astronomers, cadets, students and pupils from universities and colleges from all over the world.

A group of lecturers, cadets and students from Georgi Benkovski Bulgarian Air Force Academy (BAFA) have been taking part in the IASC program, since 2020. They have taken part in several observational research campaigns. They have followed up hundreds of asteroids and have discovered four new asteroids, which are part of the Main Asteroid Belt, located between Mars and Jupiter.

2. Scientific and Research Process in The International Astronomical Search Collaboraion Science Program

International Astronomical Search Collaboration was started in October, 2006 by a group of lecturers from Hardin-Simmons University (HSU), Abilene, Texas and is organized and sponsored by National Aeronautics and Space Administration (NASA). Since then, Program Director has been the Professor of Mathematics and Astronomy – Dr. Patrick Miller, who also teaches introductory astronomy and astronomical research methods at HSU.

The IASC is a program, mainly oriented towards cadets, students, pupils and their lecturers and teachers from all around the world. Participants in the IASC program have access to astronomical data from observations, carried out with large professional telescopes. The participants process the data with the help of *Astrometrica* professional interactive software tool for scientific grade astrometric data reduction of Charge-Coupled Devices (CCD) images (*Figure 1*). This gives them the opportunity to make real astronomical discoveries of new objects – asteroids, to contribute to specifying of the orbital elements of the observed objects – asteroids, comets and trans-Neptunian objects [1].

The participants in the program undergo training, which is focused on the study of the basics of spherical astronomy and, in particular, equatorial coordinate system. This is necessitated by the need of a better understanding of the Astrometrica interactive software tool working principle, and the correct identification of the moving objects, discovered in the astronomical images.

The work of the teams, which take part in the IASC program is organized and divided into observational campaigns with varying durations from 20 to 45 days each. The participants receive astronomical images in an Internet space, which is different for each team. The sets of images contain a minimum of three images, most commonly four, captured in sufficiently short time intervals by large telescopes, equipped with CCD. For the fulfillment of the scientific tasks of the IASC program, are used the large telescopes of the international astronomical programs Catalina, Pan-STARRS and Faulkes Telescopes. The program is supported by NASA [2]. Among the IASC program partners is Rozhen National Astronomical Observatory. The sets of images are processed with the help of Astrometrica professional astronomical software tool (*Figure 1*).

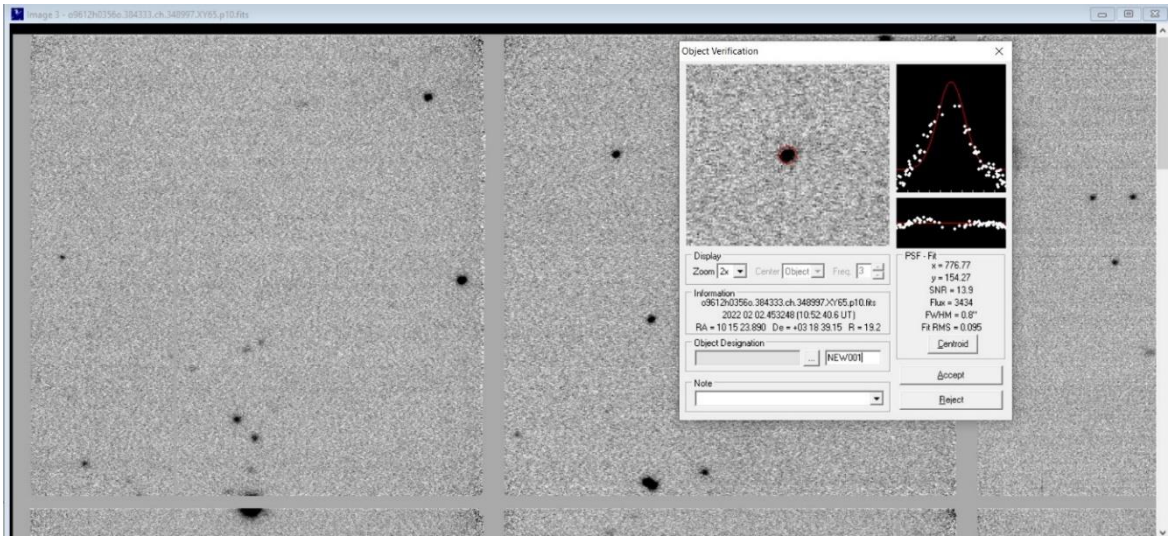

Figure 1. Processing of astronomical images with Astrometrica professional interactive software tool

This is an astronomical tool which facilitates the comparing of astronomical images, in order to search for, follow up and discover moving objects. The stars in the astronomical images are identified using the Positions and Proper Motions Star Catalogue (PPM Star Catalogue). The discovered object is compared and matched to the objects in the Minor Planet Center (MPC) database at Harvard-Smithsonian Center for Astrophysics. Regardless of the moving object being a new or already discovered asteroid, its equatorial coordinates – Right Ascension (*RA*) $\boldsymbol{\alpha}$ and Declination (*De*) $\boldsymbol{\delta}$ – are calculated. A text file (*.txt*) containing the calculated coordinates is then prepared to be included in the MPC database. This MPC report is sent to the IASC program database, which in turn sends it to the MPC database. The astrometrical observations performed by the participants, are included in the MPC database to be used for further refinement of the orbital elements of the asteroids, and defining the orbits of the new asteroids. A large number of preliminary discoveries of new asteroids are made, by the participants during each observational campaign [3]. After these asteroids have been monitored for a period of 5-7 years, their orbital elements are refined and these discoveries are designated as provisional. Then, an opportunity is given to the people who have discovered them to name them in accordance with the requirements of the International Astronomical Union (IAU) Division F Working Group for Small Bodies Nomenclature.

Bulgarian teams of students from secondary schools in Varna and Shumen, as well as, students from The University of Shumen, have taken part in the program, since 2008. Teams of cadets and students from Nikola Vaptsarov Bulgarian Naval Academy have participated in the IASC program, since 2017, and a group of lecturers, cadets and students from Georgi Benkovski Bulgarian Air Force Academy – since 2020.

So far, several thousand asteroids have been followed up by Bulgarian participants, over 200 preliminary and 24 provisional discoveries have been made, 4 of which have come as a result of the work of Georgi Benkovski Bulgarian Air Force Academy's teams.

3. Participation of Georgi Benkovski Bulgarian Air Force Academy in The International Astronomical Search Collaboration Science Program

The Aerospace Society of Georgi Benkovski Bulgarian Air Force Academy joined the IASC program in May 2020. Aerospace Society is the name of the group of lecturers, cadets and students from Georgi Benkovski Bulgarian Air Force Academy who take part in the program. Each year, the society participates in more than 10 observational campaigns.

Each cadet or student undergoes basic training on working with the Astrometrica interactive software tool for image processing. The participants in the IASC program receive a license to work with the Astrometrica software tool. Each cadet or student processes all image sets and sends them to the Team Leader – eng. Milen Simeonov. The team leader then checks all calculations and prepares a Report, containing the most precise and accurate calculations. The report is sent to the Program Coordinator. A summary report of all teams is sent for publication in the MPC's Circular at Harvard-Smithsonian Center for Astrophysics. Following their participation in each of the observational campaigns, the cadets and

the students receive Certificate for participation and/or Certificate for discovery (preliminary discovery) of a new asteroid (*Figure 2*).

Figure 2. Certificates for participation in various campaigns of The International Astronomical Search Collaboration science program

The new asteroids are given preliminary temporary designations. After their following up and refinement of their orbital elements, the asteroids are assigned a permanent number (are linked) and they could be named. The following up of the newly discovered asteroids makes it possible for their orbits to be refined.

Aerospace Society – Georgi Benkovski Bulgarian Air Force Academy has participated in different types of campaigns of the International Astronomical Search Collaboration program, as follows:

- International Asteroid Search Campaigns (IASC) – the teams of Student Space Society – Bulgarian Air Force Academy (SSS) and Space Cadets – Bulgarian Air Force Academy (SC). More than 150 teams from universities and colleges from all over the world participate in this campaign, on a monthly basis;

- All Bulgaria Asteroid Search Campaigns (All BG ASC) – the teams of Student Space Society – Bulgarian Air Force Academy (SSS) and Space Cadets – Bulgarian Air Force Academy (SC). This is a campaign that is carried out once every two months and only Bulgarian teams from Georgi Benkovski Bulgarian Air Force Academy, Nikola Vaptsarov Bulgarian Naval Academy, Secondary School of Mathematics, Varna, Secondary Schools from Shumen and Veliko Tarnovo take part in it;

- Target Near-Earth Objects! Campaign (Target NEOs!) – the teams of Aerospace Society – Bulgarian Air Force Academy (ASS). Only the most experienced teams, which are able to

perform the most accurate and precise image processing and orbital elements calculations, participate in this campaign. Its aim is to search for close to Earth and hazardous asteroids!

The members of the Aerospace Society – Georgi Benkovski Bulgarian Air Force Academy are Milen Simeonov, Veselka Radeva, Kiril Kambushev, Mihail Yordanov, Kristiyana Nikolova, Nikolay Manev, Aneliya Bliznakova, Radina Bodurova, Borislav Ivanov, Aleks Sandev and Svetoslav Ivanov.

The periods of the campaigns, in which cadets, students and lecturers from Georgi Benkovski Bulgarian Air Force Academy have participated, are as follows:

- September 11 – October 06, 2020 – International Asteroid Search Campaign;
- October 9 – November 3, 2020 – All Bulgaria Asteroid Search Campaign;
- February 4 – March 1, 2021 – International Asteroid Search Campaign;
- March 5 – March 30, 2021 – International Asteroid Search Campaign;
- April 5 – April 30, 2021 – All Bulgaria Asteroid Search Campaign;
- November 1 – November 26, 2021 – All Bulgaria Asteroid Search Campaign and Target NEOs! Asteroid Search Campaign;
- January 28 – February 22, 2022 – All Bulgaria Asteroid Search Campaign.

4. Following Up and Discovering Asteroids in The International Astronomical Search Collaboration Science Program

The participation of the Aerospace Society – Georgi Benkovski Bulgarian Air Force Academy in the IASC program has been extremely successful. The members of the BAFA Aerospace Society have processed thousands of astronomical images and have made dozens of preliminary discoveries, as well as, four provisional discoveries. This means that, the teams of Georgi Benkovski Bulgarian Air Force Academy have discovered four new objects in the Solar System and the orbit of a large number of new asteroids is yet to be confirmed.

Table 1: *Summarized results of the individual teams' work in the astronomical campaigns for the period May 2020 – March 2022*

Year	Campaigns	Processed images	Preliminary discoveries	Provisional discoveries	Participants
2020	IASC	> 600	12	0	SSS / SC
2021	IASC All BG ASC	> 2350 in total	19	**2021 FE21** **2021 EM8** **2021 GK117** **2021 GH154**	SSS / SC
2021	Target NEOs!	> 100	10	0	ASS
2022	All BG ASC	> 200	3	0	SSS / SC

Note: The data is as at 23h59min59sec on March 15, 2022. The scientific and research work of the Georgi Benkovski Bulgarian Air Force Academy teams continues uninterrupted and new astronomical images are being processed. New preliminary and provisional discoveries are being made, as well.

In Table 1, the results of the scientific and research work of the Georgi Benkovski Bulgarian Air Force Academy's individual teams, are summarized and presented for the period May 2020 – March 2022.

In Figure 3 Certificates certifying the discovery of the four new asteroids, part of the Main Asteroid Belt, located between Mars and Jupiter, are presented.

Figure 3. Certificates for the discovery of the four new asteroids (chronologically)

5. Orbial Elements of the Four New Asteroids Discovered by the Georgi Benkovski Bulgarian Air Force Academy's Individual Teams

The orbital elements make it possible to calculate the ephemeris of the object, which means that, it can be observed and followed up at any time. The accuracy of the astrometric calculations affects the accuracy of the calculated orbital elements. Accurately calculated orbital elements, allow an accurate ephemeris to be made (table with object coordinates). The correct ephemeris will show the exact position of the object in the sky, which will allow it (the object) to be observed with telescopes. As a result of these observations, it will be possible to obtain a new image of the asteroid with the CCD matrix of the telescope.

Because of that, very accurate and precise calculations of the positions of asteroids have to be made.

The orbital elements that determine the position of an asteroid in the Solar System, are:

- ***Length of the Major Semi-axis of the Ellipse – a.*** It is measured in *astronomical units (AU)* (1 *AU* = 149 597 870 km);

- ***Perihelion Distance – q***. This is the distance from the Sun to the nearest point of the asteroid from the cometary orbit *p*. It is also measured in *astronomical units (AU)*;

- ***Orbital Eccentricity – e.*** This is a parameter which describes the type of the orbit. Eccentricity is the distance from the center of the ellipse to the Sun, divided by the major semi-axis of the ellipse;

- ***Orbital Inclination – i***. This is the inclination of the plane of the comet's orbit relative to the plane of the Earth's (ecliptic) plane. It is measured in *degrees (deg)*;

- ***Longitude of the Ascending Node – node; Argument of Perihelion – peri.*** This is the angle locked between the line connecting the Sun with the ascending node and the line connecting the Sun with the perihelion point *p* of the asteroid's orbit. This angle is read from the ascending node in the direction of the asteroid's motion. The perihelion argument describes the orientation of the celestial body's orbit in its own plane. The angle lies in the orbital plane of the body;

- ***Period of the Body's Orbiting the Sun – P.*** It is measured in *years*. The exact moment, a comet or an asteroid passes through its perihelion, i.e., through the point ***p (Date and Time of Perihelion) – Tp;***

- ***Anomaly – M –*** the position of the asteroid in a certain period of time;

- ***The Distance Between the Asteroid and the Sun – Q*** at the farthest point from its orbit – ***aphelion.***

The asteroids, discovered by the teams of Georgi Benkovski Bulgarian Air Force Academy, are part of the Main Asteroid Belt, located between Mars and Jupiter.

Chronologically, the asteroids were discovered, as follows:

- **2021 FE21** – discovered by the members of the Student Space Society – Bulgarian Air Force Academy, citizen scientists V. Radeva, M. Simeonov, K. Kambushev, M. Yordanov, K. Nikolova and N. Manev;

- **2021 EM8** –discovered by the members of the Student Space Society – Bulgarian Air Force Academy, citizen scientists V. Radeva and M. Simeonov;

- **2021 GK117** – discovered by the members of the Student Space Society – Bulgarian Air Force Academy, citizen scientists M. Simeonov, V. Radeva, K. Kambushev, M. Yordanov, N. Manev and K. Nikolova;

- **2021 GH154** – discovered by the members of the Space Cadets – Bulgarian Air Force Academy, citizen scientists M. Simeonov, V. Radeva, K. Kambushev, M. Yordanov, N. Manev and K. Nikolova.

With the help of Orbit Viewer software of NASA's Jet Propulsion Laboratory (JPL), implemented using two-body methods, the orbital elements and the orbital diagram of each of the newly discovered asteroids, are calculated and presented.

The orbital elements of the asteroid **2021 FE21**, are presented in Figure 4.

Osculating Orbital Elements

Epoch 2459600.5 (2022-Jan-21.0) TDB
Reference: JPL 1 (heliocentric **IAU76/J2000** ecliptic)

Element	Value	Uncertainty (1-sigma)	Units
e	0.09004610193781928	.00023167	
a	2.684468877142602	.00015856	au
q	2.442742918982516	.00064388	au
i	6.501092542322341	.0010261	deg
node	280.7817035353619	.0087211	deg
peri	266.8190416087637	.19299	deg
M	76.38153550920481	.14698	deg
tp	2459259.643271950654 2021-Feb-14.14327195	.66506	TDB
period	1606.51944582833 4.398410529304121	.14234 3.8971e-4	d y
n	0.2240869234012801	1.9854E-5	deg/d
Q	2.926194835302689	.00017284	au

Miscellaneous Details

solution date	2021-May-04 17:05:47
# obs. used (total)	18
data-arc span	28 days
first obs. used	2021-03-18
last obs. used	2021-04-15
planetary ephem.	DE441
SB-pert. ephem.	SB441-N16
condition code	5
norm. resid. RMS	.46616
source	JPL
producer	Otto Matic
Earth MOID	1.45497 au
Jupiter MOID	2.09133 au
T_jup	3.360

*Figure 4. Osculating Orbital Elements of the asteroid **2021 FE21** (image: Solar System Dynamics, NASA Jet Propulsion Laboratory)*

The orbital diagram of the asteroid **2021 FE21**, is presented in Figure 5.

The asteroid **2021 FE21** was discovered by the members of the Student Space Society – Bulgarian Air Force Academy, citizen scientist V. Radeva, M. Simeonov, K. Kambushev, M. Yordanov, K. Nikolova and N. Manev.

The asteroid **2021 FE21** is part of the Main Asteroid Belt, located between Mars and Jupiter.

The discovery was made using astronomical images, taken on March 18, 2021. The orbital elements were calculated on the base of 18 astronomical images. As a result of the processing of these astronomical images and the calculated equatorial coordinates, it is determined that the period of the asteroid **2021 FE21** orbiting the Sun is 4.3984105 years.

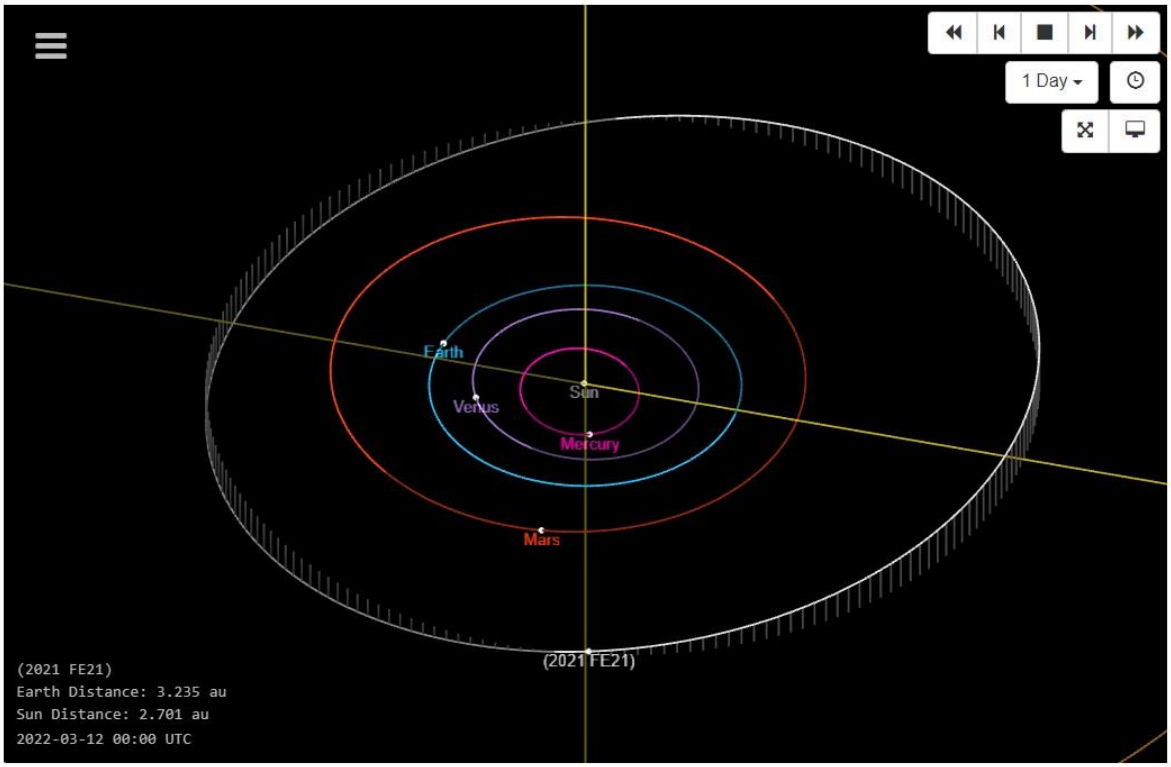

*Figure 5. Orbit of the asteroid **2021 FE21** at 00h00min UTC, 2022-03-12 (image: Solar System Dynamics, NASA Jet Propulsion Laboratory)*

The team that made the discovery, has prepared a proposal for the Name of the asteroid, which will be sent to the IASC Program Director – the Professor of Mathematics and Astronomy – Dr. Patrick Miller, for submission to the IAU Division F Working Group for Small Bodies Nomenclature. The asteroid will be named "Benkovski", after the name of Georgi Benkovski (pseudonym of Gavril Gruev Hlatev) – a Bulgarian revolutionary and leading figure in the organization and direction of the Bulgarian Anti-Ottoman April Uprising of 1876, and Apostle of its 4th Revolutionary District. Georgi Benkovski is also the Patron of Georgi Benkovski Bulgarian Air Force Academy!

The orbital elements of the asteroid **2021 EM8**, are presented in Figure 6.

Osculating Orbital Elements

Epoch 2459600.5 (2022-Jan-21.0) TDB
Reference: JPL 2 (heliocentric IAU76/J2000 ecliptic)

Element	Value	Uncertainty (1-sigma)	Units
e	0.1179994229220146	2.1729E-6	
a	2.634877565554463	1.3509E-7	au
q	2.323963533348874	5.6161E-6	au
i	5.667148464378872	1.1669E-5	deg
node	295.642162909326	.00017968	deg
peri	275.4054732227148	.00061375	deg
M	53.32693840058328	.00041547	deg
tp	2459369.089406367039 2021-Jun-03.58940637	.0017876	TDB
period	1562.208823654399 4.277094657506910	.00012014 3.2893e-7	d y
n	0.2304429437018986	1.7722E-8	deg/d
Q	2.945791597760052	1.5103E-7	au

Miscellaneous Details

solution date	2021-May-21 23:49:39
# obs. used (total)	34
data-arc span	4807 days (13.16 years)
first obs. used	2008-03-11
last obs. used	2021-05-09
planetary ephem.	DE441
SB-pert. ephem.	SB441-N16
condition code	1
norm. resid. RMS	.47983
source	JPL
producer	Otto Matic
Earth MOID	1.32745 au
Jupiter MOID	2.06503 au
T_jup	3.381

*Figure 6. Osculating Orbital Elements of the asteroid **2021 EM8** (image: Solar System Dynamics, NASA Jet Propulsion Laboratory)*

The orbital diagram of the asteroid **2021 EM8**, is presented in Figure 7.

The asteroid **2021 EM8** was discovered by the members of the Student Space Society – Bulgarian Air Force Academy, citizen scientist V. Radeva and M. Simeonov.

The asteroid **2021 EM8** is part of the Main Asteroid Belt, located between Mars and Jupiter.

The discovery was made using astronomical images, taken on March 11, 2008. The orbital elements were calculated on the base of 34 astronomical images. As a result of the processing of these astronomical images and the calculated equatorial coordinates, it is determined that the period of the asteroid **2021 EM8** orbiting the Sun is 4.1686652 years.

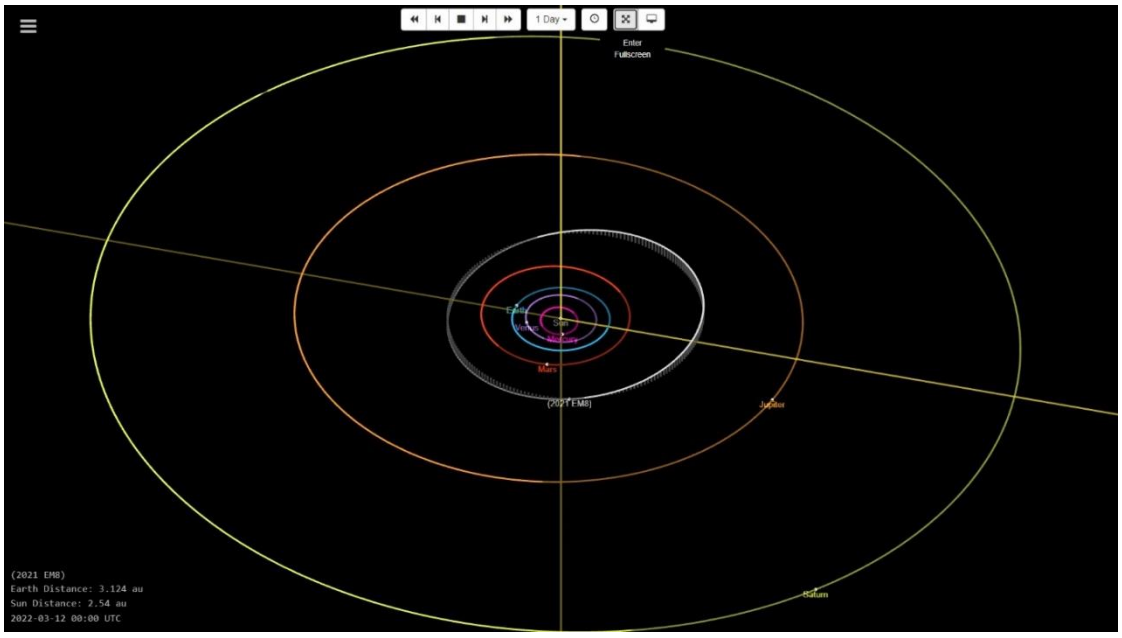

*Figure 7. Orbit of the asteroid **2021 EM8** at 00h00min UTC, 2022-03-12 (image: Solar System Dynamics, NASA Jet Propulsion Laboratory)*

The team that made the discovery, has prepared a proposal for the Name of the asteroid. The asteroid will be named "Yordanov" – after the name of Assen "Jerry" Jordanoff (born Asen Hristov Yordanov) – a Bulgarian-American inventor, engineer, and aviator. Jordanoff is considered to be the founder of Aeronautical Engineering in Bulgaria, as well as a contributor to the development of aviation

in the United States. The proposal will be sent to the IASC Program Director – the Professor of Mathematics and Astronomy – Dr. Patrick Miller, for submission to the IAU Division F Working Group for Small Bodies Nomenclature.

The orbital elements of the asteroid **2021 GK117**, are presented in Figure 8.

Osculating Orbital Elements

Epoch 2459600.5 (2022-Jan-21.0) TDB
Reference: JPL 1 (heliocentric IAU76/J2000 ecliptic)

Element	Value	Uncertainty (1-sigma)	Units
e	0.1861766160348929	1.071E-7	
a	2.428335537505881	3.6979E-8	au
q	1.976236244535764	2.8117E-7	au
i	4.120431775591388	1.6208E-5	deg
node	215.5766876138728	.00010218	deg
peri	75.91027757068744	.00019679	deg
M	20.81627105608044	.00013401	deg
tp	2459520.578816978365 2021-Nov-02.07881698	.00051362	TDB
period	1382.170025086436 3.784175291133295	3.1571E-5 8.6437e-8	d y
n	0.2604599965749416	5.9494E-9	deg/d
Q	2.880434830475999	4.3863E-8	au

Miscellaneous Details

solution date	2021-Jul-02 01:46:20
# obs. used (total)	36
data-arc span	6977 days (19.10 years)
first obs. used	2002-05-05
last obs. used	2021-06-11
planetary ephem.	DE441
SB-pert. ephem.	SB441-N16
condition code	0
norm. resid. RMS	.54912
source	JPL
producer	Otto Matic
Earth MOID	.966104 au
Jupiter MOID	2.30531 au
T_jup	3.482

*Figure 8. Osculating Orbital Elements of the asteroid **2021 GK117** (image: Solar System Dynamics, NASA Jet Propulsion Laboratory)*

The orbital diagram of the asteroid **2021 GK117**, is presented in Figure 9.

The asteroid **2021 GK117** was discovered by the members of the Student Space Society – Bulgarian Air Force Academy, citizen scientist M. Simeonov, V. Radeva, K. Kambushev, M. Yordanov, N. Manev and K. Nikolova.

The asteroid **2021 GK117** is part of the Main Asteroid Belt, located between Mars and Jupiter, as well.

The discovery was made using astronomical images, taken on May 5, 2002. The orbital elements were calculated on the base of 36 astronomical images. As a result of the processing of these astronomical images and the calculated equatorial coordinates, it is determined that the period of the asteroid **2021 GK117** orbiting the Sun is 3.7841753 years.

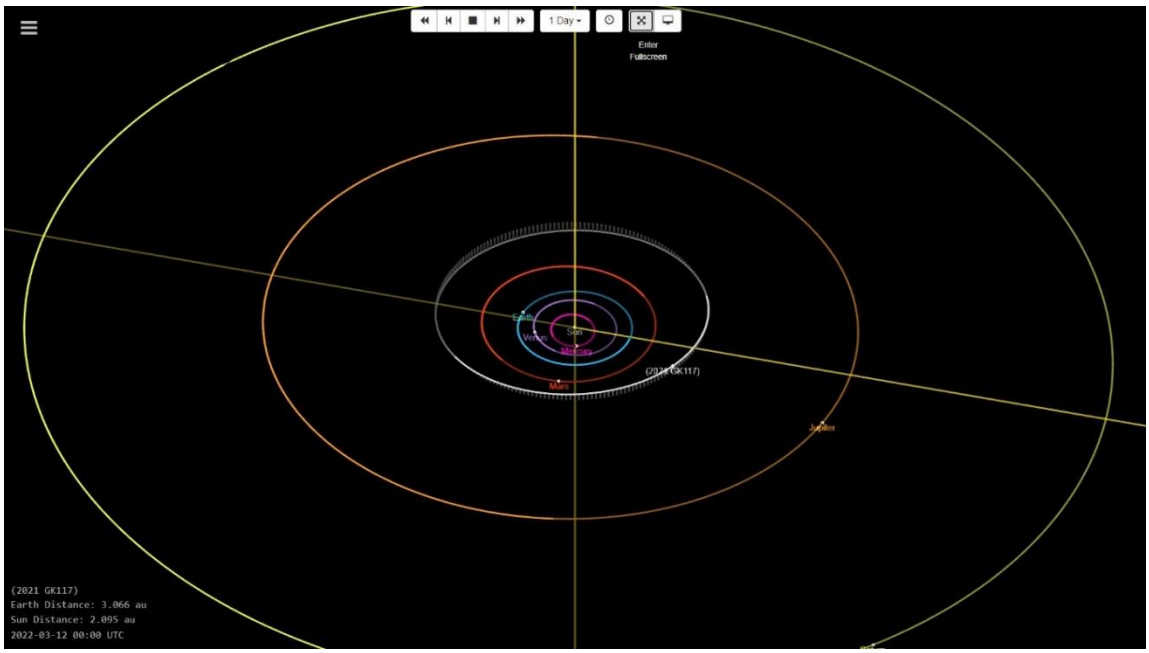

*Figure 9. Orbit of the asteroid **2021 GK117** at 00h00min UTC, 2022-03-12 (image: Solar System Dynamics, NASA Jet Propulsion Laboratory)*

The team that made the discovery, has prepared a proposal for the Name of the asteroid. The asteroid will be named "Spisarevski" – after the name of Dimitar Svetozarov Spisarevski – a Bulgarian fighter

pilot known for taking down an American bomber by ramming it during the bombing of Sofia, in World War II. The proposal will be sent to the IASC Program Director – the Professor of Mathematics and Astronomy – Dr. Patrick Miller, for submission to the IAU Division F Working Group for Small Bodies Nomenclature.

The orbital elements of the asteroid **2021 GH154**, are presented in Figure 10.

Osculating Orbital Elements

Epoch 2459600.5 (2022-Jan-21.0) TDB
Reference: JPL 1 (heliocentric IAU76/J2000 ecliptic)

Element	Value	Uncertainty (1-sigma)	Units
e	0.1668910517292669	8.729E-5	
a	2.2421580437295	.00016273	au
q	1.867961929668248	.00015759	au
i	5.027811850290158	.00095133	deg
node	142.25240508689	.0077817	deg
peri	152.2954079816067	.027905	deg
M	13.52960362634005	.039757	deg
tp	2459554.412799126839 2021-Dec-05.91279913	.13174	TDB
period	1226.302911198146 3.357434390686231	.1335 3.6550e-4	d y
n	0.293565314664601	3.196E-5	deg/d
Q	2.616354157790752	.00018989	au

Miscellaneous Details

solution date	2021-Jul-09 18:04:53
# obs. used (total)	10
data-arc span	32 days
first obs. used	2021-04-06
last obs. used	2021-05-08
planetary ephem.	DE441
SB-pert. ephem.	SB441-N16
condition code	5
norm. resid. RMS	.449
source	JPL
producer	Otto Matic
Earth MOID	.85482 au
Jupiter MOID	2.5723 au
T_jup	3.610

*Figure 10. Osculating Orbital Elements of the asteroid **2021 GH154** (image: Solar System Dynamics, NASA Jet Propulsion Laboratory)*

The orbital diagram of the asteroid **2021 GH154**, is presented in Figure 11. This is the last discovered asteroid from the members of the Aerospace Society – Georgi Benkovski Bulgarian Air Force Academy as at 23h59min59sec on March 15, 2022 in the IASC scientific and research program.

The asteroid **2021 GH154** was discovered by the members of the Student Space Society – Bulgarian Air Force Academy, citizen scientist M. Simeonov, V. Radeva, K. Kambushev, M. Yordanov, N. Manev and K. Nikolova.

The asteroid **2021 GH154** is part of the Main Asteroid Belt, located between Mars and Jupiter, as well.

The discovery was made using astronomical images, taken on April 6, 2021. The orbital elements were calculated on the base of 10 astronomical images. As a result of the processing of these astronomical images and the calculated equatorial coordinates, it is determined that the period of the asteroid **2021 GH154** orbiting the Sun is 3.3574344 years.

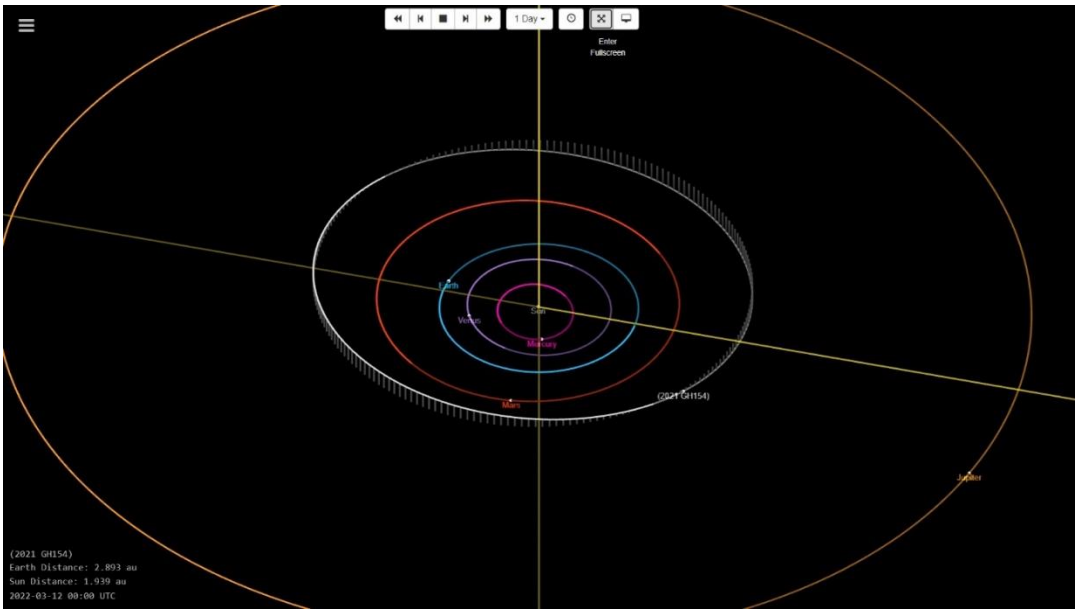

*Figure 11. Orbit of the asteroid **2021 GH154** at 00h00min UTC, 2022-03-12 (image: Solar System Dynamics, NASA Jet Propulsion Laboratory)*

The team that made the discovery, has prepared a proposal for the Name of the asteroid. The asteroid will be named "Drangov" – after the name of Boris Stoyanov Drangov – a Bulgarian colonel and warfare pedagogue. In honor of Boris Drangov, three Bulgarian settlements have been named Drangovo – Drangovo, Blagoevgrad district, Drangovo, Kardzhali district and Drangovo, Plovdiv district. Boris Drangov has been also named Drangov Peak in Antarctica. The proposal will be sent to the IASC Program Director – the Professor of Mathematics and Astronomy – Dr. Patrick Miller, for submission to the IAU Division F Working Group for Small Bodies Nomenclature.

6. Conclusions

The search for and discovery of new asteroids in the Solar System is an important part of the process of its study. Following up already discovered asteroids helps for better understanding of their motion.

The participation of lecturers, cadets and students from the Aerospace Society – Georgi Benkovski Bulgarian Air Force Academy in the International Astronomical Search Collaboration science program is a contribution to the study of asteroids in the Solar System, as a whole. In this way, Earth-hazardous objects can be detected and also followed up long before a catastrophic collision with our planet Earth occurs.

In addition, the opportunity given to students to be an active part of the astronomy research process, motivates them to expand their knowledge of Astronomy.

Understanding each activity in the process of work, discussing emerging problems, self-checking the results and their analysis – these are important steps in mastering the difficult process of scientific knowledge and research.

By participating in the International Astronomical Search Collaboration research program, supported by NASA, the teams of Aerospace Society – Georgi Benkovski Bulgarian Air Force Academy contribute to the protection of the Earth from space hazards.

References

1. Miller, J. P., International Astronomical Search Collaboration: An Online Outreach Program in Astronomical Discovery for High School & College Students, Robotic Telescopes, *Student Research and Education Conference*, San Diego, California, June 18-21, 2017, Proceedings Conference, 2018, vol. 1, no. 1, p. 193-199, ISBN 978-0-6483996-0-5.
2. Miller, J. P., J. W. Davis, et al., An International Asteroid Search Campaign, *Astronomy Education Review*, 2008, vol. 7, no. 1, p. 57-83, ISSN 15391515.
3. Miller, J. P., International Astronomical Search Collaboration, *Space News*, Issue 60, June 2016.

Heuristic procedure for optimal structural design of a subsonic aircraft wingbox

Nikolay Kanchev

Bulgarian Air Force Academy, Aviation Faculty, Dolna Mitropolia, Bulgaria, nkanchev@af-acad.bg

Abstract: The wingbox optimal design is characterized by the intrinsic non-linearity and large scale of the optimization procedures, as well as the inevitable presence of multiple imposed constraints, which limit the capabilities of the gradient optimization methods. Using a parametric finite element model this paper proposes a heuristic structural-optimization algorithm suitable for the stage of detailed design of a wingbox. The approach is demonstrated by solving an optimization problem for the minimum mass of a subsonic jet tapered wing's load-bearing structure while adhering to the constraints of not exceeding the maximum von Mises stress and providing a margin of structural stability. The final evaluation and assessment of the optimization process, as well as the obtained results, revealed that the proposed procedure effectively converges to global minima while taking all of the imposed constraints into account.

Keywords: *wingbox, structural optimization, PSO, FEM, adaptive penalization, subsonic jet*.

1. Introduction

The wingbox design process must balance the opposing requirements of low mass and high structural stiffness. Traditionally, beam finite element models are used to idealize the load-bearing structure of large aspect ratio wings during the early phases of design [21]. The process of determining the needed number of spars, stringers, and ribs, as well as their dimensions, cross sections, structural materials, and relative placements, is defined as initialization of the basic wingbox. At this stage of the design process, relevant statistics or internal layout considerations are frequently used to drive decisions. The acquired results enable for the creation of a more complete finite element model in the future [22, 23].

The required cross-sectional areas and thicknesses of the load-bearing structural components are estimated applying appropriate sizing optimization methods with the objective of minimizing structural mass while not exceeding the material's maximum von Mises stress and maintaining structural stability.

The majority of structural optimization problems are nonlinear, constrained and large in scale, which limits the application of gradient optimization methods [4]. As a result, many heuristic and metaheuristic optimization strategies, as well as optimality criteria approaches, are frequently used. The sizing structural optimization procedure is often referred to as a process for estimating of the optimal values for a large number of structural design variables under a variety of functional and box constraints.

Heuristic optimization methods are best suited for problems with high dimensionality, multimodality or lack of gradient information, mainly because in these kind of methods the extremum is searched stochastically. The ability of these optimization methods to mimic processes and phenomena observed in nature is one of their distinguishing characteristics. Typical heuristic methods for optimization are the

genetic algorithms [7, 11], the optimization with simulated annealing model [14], etc. Common drawback of the genetic optimization methods is their requirement for design variables and objective encoding/decoding, as well as the challenges associated with the handling of the constraints. Another type of heuristic optimization procedures replicate the social interaction between individuals with common interests inside a distinct group. Typical examples in nature are the fish schooling, the flock of birds or the bee swarm (Fig. 1). These optimization approaches allow for parametric manipulation of the group's individual and collective intelligence. The most well-known examples of this family of algorithms include optimization methods based on an ant colony model [5] or on a swarm of intelligent particles, known as Particle Swarm Optimization or PSO [13].

Figure 1. Some heuristic algorithms replicate the social interaction between individuals in a group

The primary benefit of the heuristic approach to structural optimization lies in its ability to perform direct global optimization. The main challenge in heuristic optimization methods is taking into consideration all of the imposed functional and box constraints. Several strategies for eliminating this issue have been proposed as a result of numerous studies in this field. Among the most commonly used are the penalty method, the constraint aggregation method, the method of the combined KS-function [15, 16], etc. The efficient handling of the imposed constraints generally depends on the level of control over the optimization process. As a result, the current paper investigates the concept of heuristic sizing optimization of load-bearing structural components for the wingbox of a tapered wing by structural optimization approach based on a swarm of intelligent particles (PSO).

2. Methodology

The method of optimization by a swarm of intelligent particles is based on the notion that social exchange of information among individuals in a specific group provides an evolutionary advantage [13]. The approach has been used at different stages of design in electronics, automation, energy, and mechanical engineering. Particle swarm optimization is one of the most popural and state-of-the-art research methods in the field of aircraft structural optimization [2,3,6,8,12,19,20].

The optimization process is stochastic in nature and is carried out by updating the positions of each particle by a velocity vector, the magnitude and direction of which are determined according to the individual and collective achievements of the particles in the swarm (Fig. 2). Convergence to the extremal value is achieved by moving particles within the boundaries of the feasible search space via mutual sharing of information based on individual and collective memory. As a result, the position of

each particle is updated depending on the social behavior of the entire swarm, which adjusts itself to the search space, concentrating on the areas with the best values of the objective function.

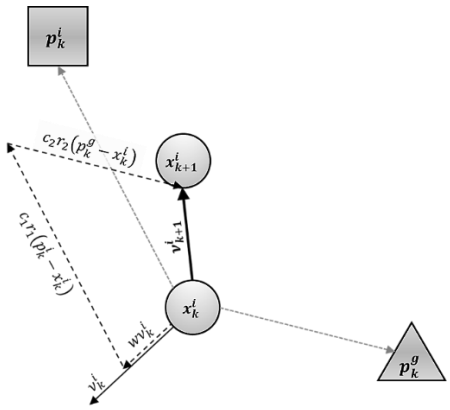

Figure 2. Basic principle of updating the position and velocity of each of the particles in the swarm.

In the *N*-dimensional search space, the position of each particle is represented by an *N*-dimensional vector $\boldsymbol{x} = \{x_1, x_2, \dots, x_i, \dots, x_N)^T$ and its velocity by another *N*-dimensional vector $\boldsymbol{v} = \{v_1, v_2, \dots, v_i, \dots, v_N)^T$.

Mathematically, the position x of the particle i in the iteration $k + 1$ is determined as follows:

$$x_{k+1}^i = x_k^i + v_{k+1}^i \Delta t \,, \tag{1}$$

where v_{k+1}^i is the updated velocity vector of the particle, Δt is the time step of the process, which is assumed to be equal to one.

The velocity vector of the particle is updated according to the following expression:

$$v_{k+1}^i = w v_k^i + c_1 r_1 \frac{p_k^i - x_k^i}{\Delta t} + c_2 r_2 \frac{p_k^g - x_k^i}{\Delta t}, \tag{2}$$

where v_k^i is the velocity vector at iteration k; p_k^i and p_k^g represent, respectively, the best position of the particle i and the best position achieved by the whole swarm in the boundaries of the search space up to the current iteration; r_1 and r_2 are uniformly distributed random numbers from 0 to 1; c_1 is the so-called cognitive parameter which indicates the degree of confidence in the individual achievements of the particles; c_2 is the so-called social parameter that indicates the degree of trust in the collective achievement of the swarm; w represents the so-called inertia coefficient, which scales the velocity vector throughout the optimization procedure.

In order to maintain the dynamic stability of the swarm, the sum of the coefficients c_1 and c_2 must not exceed 4 [13, 17].

In order to account for the imposed functional constraints, an adaptive parameterless penalty function approach has been applied [17]. The penalty coefficient p_j is based on the arithmetic mean of the objective function and the degree of violation of each of the constraints in the current iteration:

(3) $$f'(x_k) = \begin{cases} f(x_k), if\ x_k\ is\ feasible \\ f(x_k) + \sum_{j=1}^{m} p_j \hat{g}_j(x_k)\ , if\ x_k\ is\ not\ feasible \end{cases}$$

(4) $$p_j = \left|\bar{f}(x_k)\right| \frac{\bar{g}_j(x_k)}{\sum_{l=1}^{m}[\bar{g}_l(x_k)]^2}$$

(5) $$\bar{g}_j(x_k) = \frac{1}{n}\sum_{k=1}^{n} \max\left[0, \hat{g}_j(x_k)\right]$$

where $\bar{f}(x_k)$ is the arithmetic mean of the objective function in the swarm at iteration k, $\bar{g}_j(x_k)$ is the arithmetic mean of the j-th functional constraint in the swarm at iteration k. Thus the penalty coefficients are distributed in the swarm in such a way that those particles that have violated the imposed constraints the most will be sanctioned more than others.

Flowchart of the algorithm for heuristic sizing structural optimization of the wingbox of a tapered wing by a swarm of intelligent particles is presented in Fig. 3.

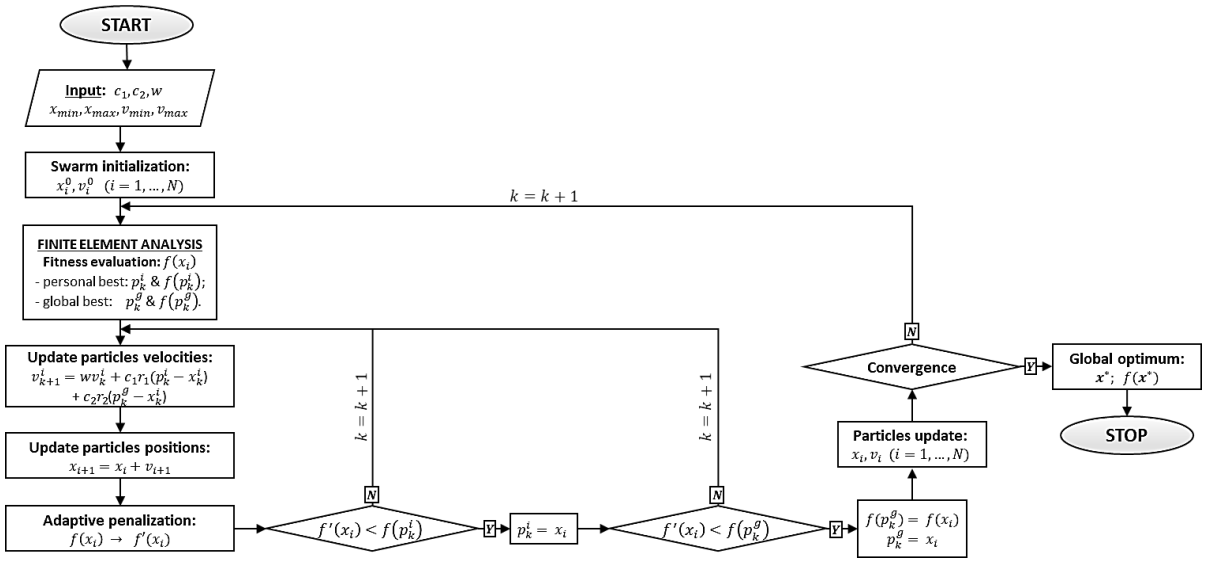

Figure. 3 Flowchart of the heuristic sizing structural optimization procedure for wingbox detail design

3. Numerical experiment

The proposed structural optimization procedure is demonstrated by applying it at the stage of detailed design of a wingbox for the tapered wing of a subsonic jet aircraft with specific wing load 585 kg/m^2. The aerodynamic load is distributed approximately according to an elliptical law and corresponds to the conditions at steady level flight with cruising speed $V = 750\ km/h$ (Fig.10). Fig. 4 shows the values of the basic geometric parameters of the wing.

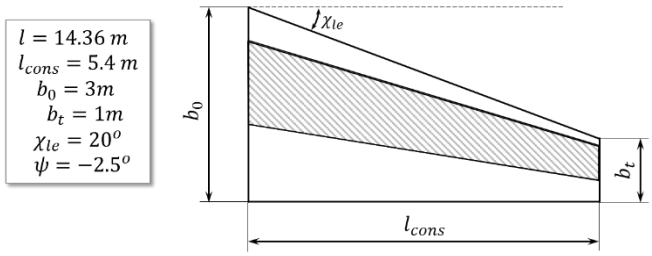

Figure 4. Wing planform basic parameters

The stress and strain evaluation of the wingbox structure is performed by the finite element method. A parametric finite element model was synthesized using the APDL programming language. The model is numerically validated in accordance with [1]. Table 1 shows the structural materials, the selected types of finite elements and the variable parameters in model of the wingbox and its load-bearing components.

Table 1: Basic parameters of the load-bearing components.

Load-bearing component	**Structural material**	**Finite element**	**Variable parameter**
Front spar flange	2618	3-D 2-node BEAM	$0.01 \leq R_{fl.fr} \leq 0.08$
Front spar web	2618	3-D 4-node SHELL	$0.001 \leq \delta_{web.fr} \leq 0.01$
Rear spar flange	2618	3-D 2-node BEAM	$0.01 \leq R_{fl.r} \leq 0.08$
Rear spar web	2618	3-D 4-node SHELL	$0.001 \leq \delta_{web.r} \leq 0.01$
Upper skin panels	7075-T6	3-D 4-node SHELL	$0.001 \leq \delta_{skin.up} \leq 0.005$
Upper skin stringers	7075-T6	3-D 2-node BEAM	$0.005 \leq R_{str.up} \leq 0.01$
Bottom skin panels	2024-T3	3-D 4-node SHELL	$0.001 \leq \delta_{skin.bot} \leq 0.005$
Bottom skin stringers	2024-T3	3-D 2-node BEAM	$0.005 \leq R_{str.bot} \leq 0.01$
Ribs	2024-T3	3-D 4-node SHELL	$\delta_{\text{реб}} = 0.003$

A structural optimization problem is defined with the objective of minimizing the wingbox mass while satisfying the compatibility condition between the nodal loads and their deflections, as well as the imposed functional constraints on equivalent stresses and the buckling load factor and also the box constraints on design variables:

$$
\begin{gathered}
\min m_{wingbox} \\
KU = F \\
\sigma_{v\,max} - \sigma_{allowed} \leq 0 \\
\lambda_I \geq 2.5 \\
0.001 \leq \delta_{skin.bot} \leq 0.005 \\
0.001 \leq \delta_{skin.top} \leq 0.005 \\
0.001 \leq \delta_{web.fr} \leq 0.01 \\
0.001 \leq \delta_{web.r} \leq 0.01 \\
0.005 \leq R_{str.bot} \leq 0.01 \\
0.005 \leq R_{str.up} \leq 0.01 \\
0.01 \leq R_{fl.fr} \leq 0.08 \\
0.01 \leq R_{fl.r} \leq 0.08 \\
\sigma_{allowed} = 400\ MPa
\end{gathered} \tag{6}
$$

A swarm of 20 particles with a cognitive coefficient $c_1 = 1.5$ and a social coefficient $c_2 = 0.5$ was initialized. The inertia coefficient w changes dynamically from 0.9 to 0.4 during iterations. The convergence criteria for of the optimization procedure is the variation σ^2 of the objective function in the swarm. The optimization procedure converges to a global extremum at a point in the search space, characterized by the following values for the vector of design variables:

Optimal design variables

- $R_{fl.fr} = 38.86\ mm$
- $\delta_{web.fr} = 10\ mm$
- $R_{fl.r} = 10.2\ mm$
- $\delta_{wall.r} = 14.9\ mm$
- $\delta_{skin.up} = 3\ mm$
- $R_{str.up} = 15\ mm$
- $\delta_{skin.bot} = 8\ mm$
- $R_{str.bot} = 2.84\ mm$

Optimal wingbox parameters

- $m_{wingbox\,min} = 529.3\ kg$
- $\sigma_{z\,max} = 202.6\ MPa$
- $\sigma_{z\,min} = -275.6\ MPa$
- $\sigma_{v\,max} = 382.3\ MPa$
- $u_{y\,max} = 0.1916\ m$
- $\lambda_I = 2.795$

Fig. 5, 6, 7 and 8 present the plots for the change of the objective function and its variation in the swarm, as well as the values of the functional constraints for each particle of the swarm during the optimization procedure. The final assessment of the optimization process, as well as the obtained results, reveal that the proposed procedure converges to global minima while satisfying all of the imposed constraints.

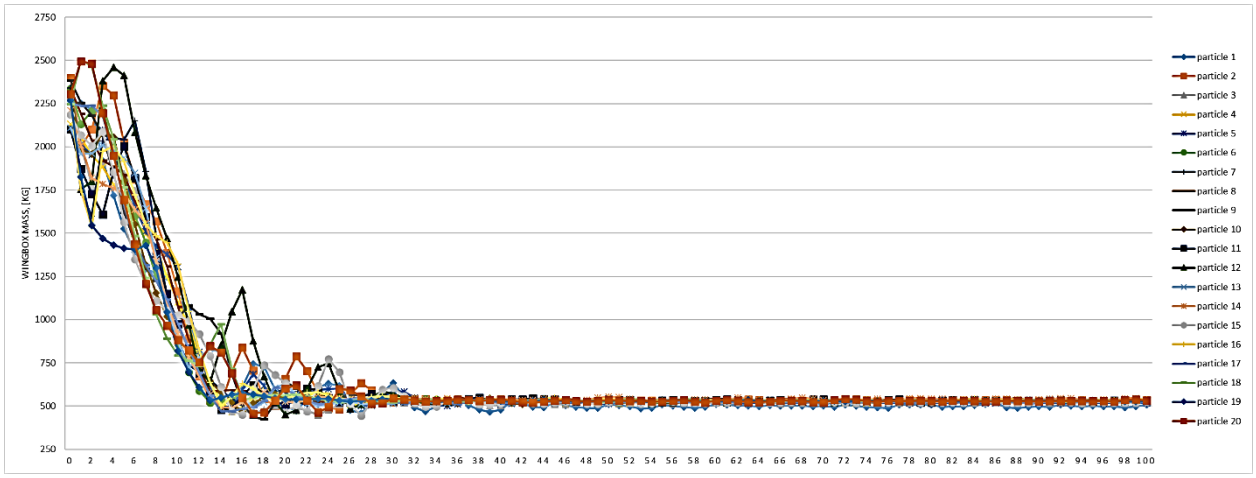

Figure 5. Convergence of the objective function: wingbox minimal mass, [kg]

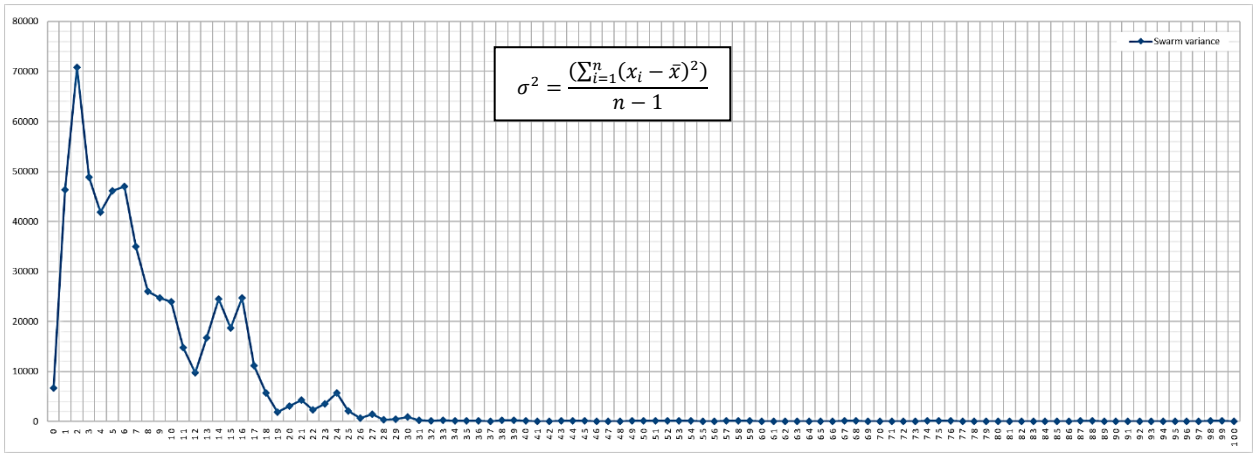

Figure 6. Change in the variation σ^2 of the objective function in the swarm.

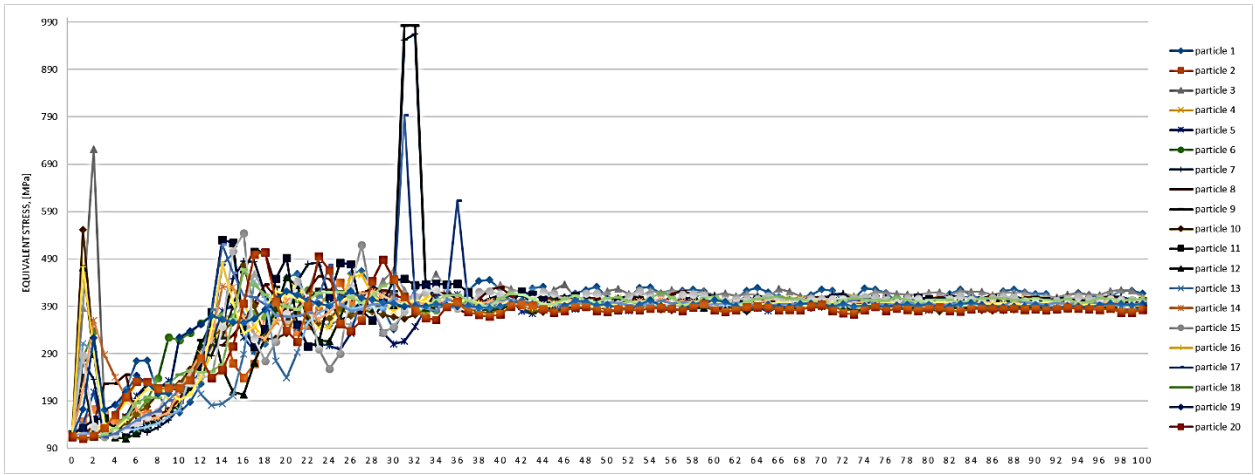

Figure 7 Convergence of the maximum von Mises stress $\sigma_{v\,max}$ towards the imposed constraint.

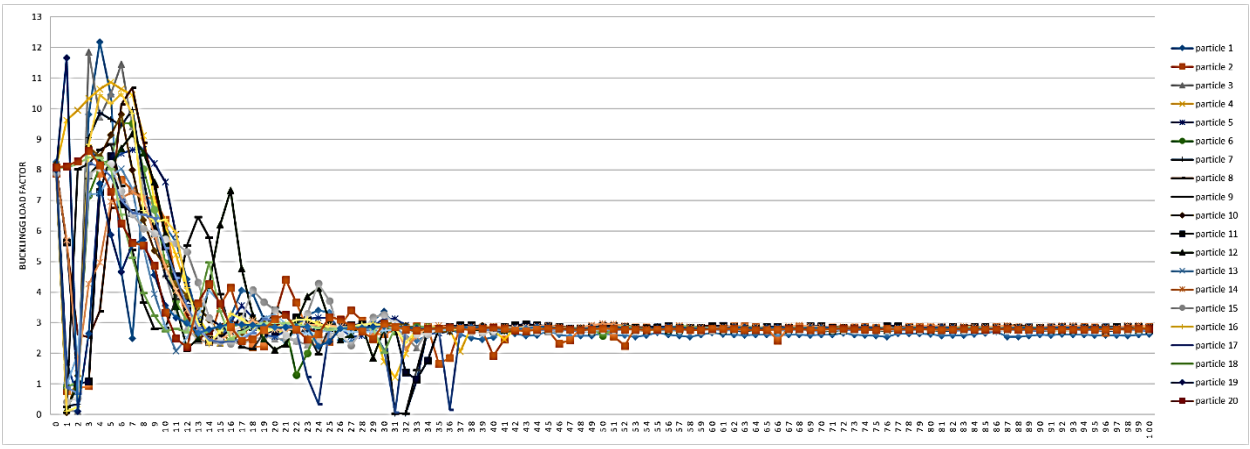

Figure 8. Convergence of the buckling load factor λ_{min} towards the imposed constraint

Fig. 9 shows the obtained optimal wingbox. The boundary conditions for the finite element analysis are visualized in Fig. 10. The vertical displacements, normal and equivalent stresses as well as the distribution of the buckling load factor in the optimal wingbox as a result of the applied boundary conditions are presented in Fig. 11.

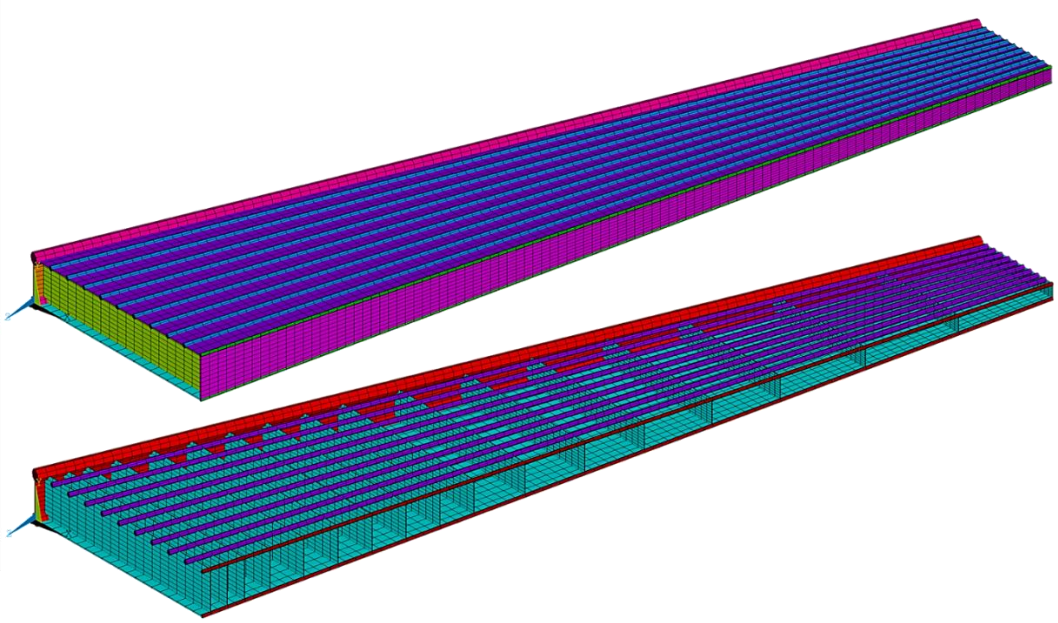

Figure 9 Optimal wingbox load-bearing structure.

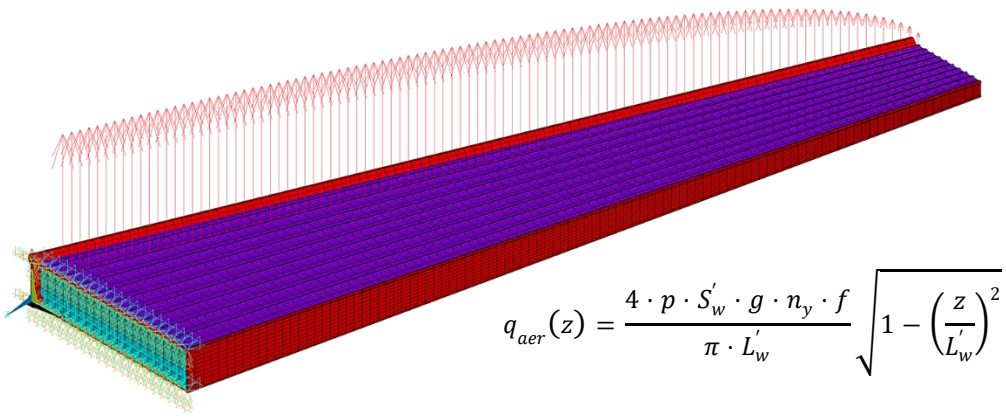

$$q_{aer}(z) = \frac{4 \cdot p \cdot S_w^{'} \cdot g \cdot n_y \cdot f}{\pi \cdot L_w^{'}} \sqrt{1 - \left(\frac{z}{L_w^{'}}\right)^2}$$

Figure 10 Boundary conditions for the finite element analysis.

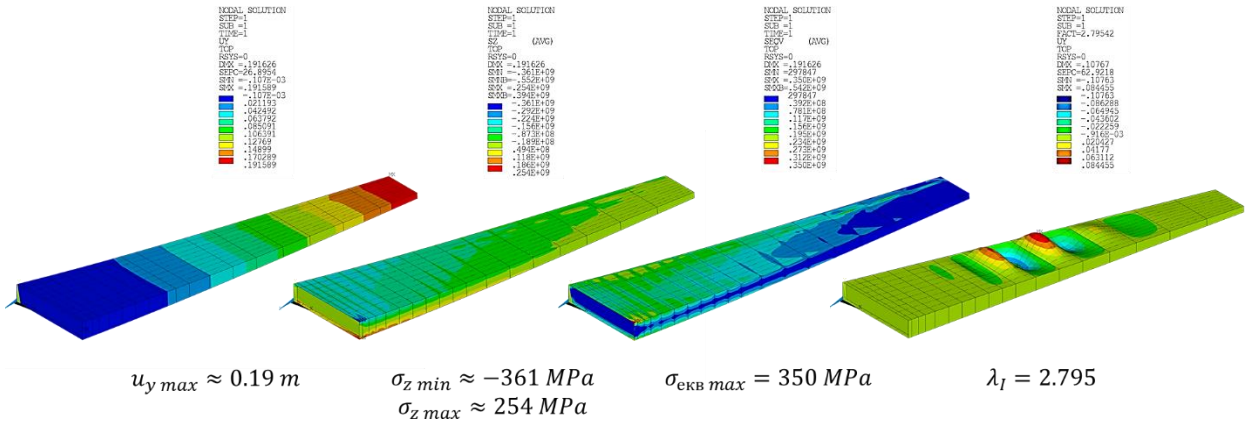

Figure 11. *Vertical displacements, normal and equivalent stresses, distribution of the buckling load factor in the optimal wingbox.*

4. Conclusion

A heuristic technique based on a swarm of intelligent particles is suggested for structural optimization of a wingbox. Based on a parametric finite element model, an optimization procedure for the minimum mass of the load-bearing structure is implemented under the condition of not exceeding the maximum allowable equivalent stress and providing a margin of stability for the structure by varying the values of eight design variables. The key issue for the heuristic structural optimization approach was to account for all of the constraints. For this reason, the algorithm modifies the objective values of the individual particles using a parameterless adaptive penalization technique. The optimization process and the results demonstrate that the proposed method takes into consideration all of the specified constraints and successfully converges to a global minimum.

The proposed heuristic structural-optimization procedure can be further developed in the future through research on the following topics:

- investigation of the influence of cognitive and social coefficients on the efficiency of the optimization procedure;

- investigation of the possibility for estimation of the required number of spars, ribs, and stringers as a result of heuristic layout optimization considering different internal layout requirements;

- investigation of the possibility for simultaneous handling of boundary conditions for more than one load case;

- integration of topology optimization procedure for optimal distribution of structural material in the load-bearing components.

References

1. ASME V&V 10.1-2012: An Illustration of the Concepts of Verification and Validation in Computational Solid Mechanics.

2. Chang, N., Wang, W., Yang, W., & Wang, J. (2010). Ply stacking sequence optimization of composite laminate by permutation discrete particle swarm optimization. Structural and Multidisciplinary Optimization, 41(2), 179-187.

3. Chollom, T. D., Ofodile, N., & Ubadike, O. (2016, September). Application Techniques of Multi-objective particle swarm optimization: Aircraft flight control. In 2016 UKACC 11th International Conference on Control (CONTROL) (pp. 1-6). IEEE.

4. Christensten, P. W., & Klarbring, A. (2008). An introduction to Structural Optimization. Springer Science & Business Media

5. Dorigo M, Maniezzo V, and Colorni A. (1996). The ant system: optimization by a colony of cooperating agents, IEEE Trans Syst Man Cybernet B, Vol. 26, No. 1, pp. 29–41.

6. El Afia, A., & Sarhani, M. (2017, March). Particle swarm optimization for model selection of aircraft maintenance predictive models. In Proceedings of the 2nd international Conference on Big Data, Cloud and Applications (pp. 1-12).

7. Goldberg D. (1989). Genetic algorithms in search, optimization, and machine learning. Addison-Wesley, New York, NY.

8. Gümüşboğa, İ., & İftar, A. (2019). Aircraft trim analysis by particle swarm optimization. Journal of Aeronautics and Space Technologies, 12(2), 185-196.

9. Haftka R, and Gurdal Z. (1992). Elements of structural optimization, 3rd ed. Kluwer Academic Publishers.

10. Haug E, and Arora J. (1979). Applied optimal design, Wiley, New York, NY. Hu X, Eberhart R, and Shi Y. (2003). Engineering optimization with particle swarm, IEEE Swarm intelligence symposium (SIS 2003),Indianapolis, IN, pp. 53–57.

11. Holland, J. (1992). Genetic Algorithms. Scientific American, 66-72.

12. Kathiravan, R., & Ganguli, R. (2007). Strength design of composite beam using gradient and particle swarm optimization. Composite structures, 81(4), 471-479.

13. Kennedy J, and Eberhart R. (1995). Particle swarm optimization, IEEE international conference on neural networks, Vol. IV, Piscataway, NJ, pp. 1942–1948.

14. Kirkpatrick S, Gelatt C, and Vecchi M. (1983). Optimization by simulated annealing. Science, Vol. 220, No. 4598, pp. 671–680

15. Kreisselmeier, G., & Steinhauser, R. (1979). Systematic control design by optimizating a vector performance index. IFAC Computer Aided Design of Control Systems.

16. Martins, J. R. R. A., & Poon, N. M. (2005, June). On structural optimization using constraint aggregation. In VI World Congress on Structural and Multidisciplinary Optimization WCSMO6, Rio de Janeiro, Brasil.

17. Perez, R. E., & Behdinan, K. (2007). Particle swarm optimization in structural design. Swarm intelligence: Focus on ant and particle swarm optimization, (532).

18. Sobester, A., Forrester, A., & Keane, A. (2008). Engineering design via surrogate modelling: a practical guide. John Wiley & Sons.

19. Venter G, and Sobieszczanski-Sobieski J. (2004). Multidisciplinary optimization of a transport aircraft wing using particle swarm optimization, Struct Multidiscip Optimiz, Vol. 26, No. 1–2, pp. 121–131.

20. Zadeh, P. M., Fakoor, M., & Mohagheghi, M. (2018). Bi-level optimization of laminated composite structures using particle swarm optimization algorithm. Journal of Mechanical Science and Technology, 32(4), 1643-1652.

21. Бирюк, В.И. Методы проектирования конструкций самолётов Текст] / В. И. Бирюк, Е. К. Липин, В.М. Фролов. - М. : Машиностроение, 1977.-232 с.

22. Егер С. М. , Лисейцев Н. К. § Самойлович О. С. , Основы автоматизированного проектирования самолетов., М.: Машиностроение, 1986.

23. Фролов К.В., Том IV-21. Книга 2. Машиностроение. Энциклопедия в сорока томах. Самолеты и вертолеты. Проектирование, конструкции и системы самолетов и вертолетов, М.: Машиностроение, 2004.

Numerical Analysis of Flow around Wing Sections PIL15M825 and PIL12M850

Konstantin Metodiev

Space Research and Technology Institute, Bulgarian Academy of Sciences

Abstract: Current study objective is to compute aerodynamic coefficients of Pilatus PC-9M wing sections. Upon numerical analysis completion, plausible results are expected to emerge such as lift, drag, and pitching moment coefficients as well as a neutral point location along the section chord. The analysis has been carried out by means of a software right to solving problems in computational fluid dynamics. Besides aforementioned quantities, another essential outcome is a polar curve in terms of section form drag, i.e. drag due to both pressure and shear stress. Obtained results at different Reynolds numbers and angles of attack are depicted and discussed thoroughly.

Key words: *Pilatus PC-9M, airfoil, xFoil, drag polar, neutral point*

1. Introduction

Lack of a comprehensive knowledge, widely available to the public, as to what aerodynamic characteristics of above-noted wing sections might be motivated the research completion. The wing sections are said to have been used for designing the wing of Pilatus PC-9M (and that of Beechcraft T-6 Texan II). However, little to no aerodynamic data, limited to a few articles, is available for reference, let alone the wing sections themselves. Huang, [1] somehow assumed in advance that NACA4312 was a good replacement to the original airfoil (PIL15M825) for analysis because both wing sections had very similar aerodynamic characteristics. Snowden et al., [2] developed a flight dynamics model of PC-9/A by means of flight test data. Values of longitudinal derivatives were obtained for complete aircraft configuration. Looking up further in sites containing airfoil coordinates databases, such as UIUC, [3] and Airfoil Tools, [4] yielded no results. Questions regarding wing sections under consideration were posted in public forums by many enthusiasts to no avail.

The wing has following geometrical characteristics: section PIL15M825 at root, PIL12M850 at tip, quarter-chord sweepback 1°, dihedral 7° from center-section, incidence 1° at root, twist -2°, [5]. The

wing sections were solely encountered in article [6] and subsequently borrowed for the current research needs with a strong belief that the section geometries are genuine and correct.

2. Materials and Methods

The project algorithm is further described in succession.

2.1. Fluid solver brief description

To carry out computational fluid dynamics research, xFoil, [7] was believed to be appropriate. The bundle contains a solver "for viscous / inviscid analysis and mixed-inverse design of subcritical airfoils … with a Karman-Tsien compressibility correction," [8]. A two-dimensional panel method is employed by superposing discrete vortices and sources with constant strength along both wing section and wake. After applying Kutta condition, the algorithm boils down to solving numerically a linear non-homogenous algebraic system. Eventually, the iterative process finishes as soon as a certain convergence criterion is met.

xFoil does not provide a graphical user interface. Instead, a sequence of commands must be fed by the user to the console. The reader is referred to the appendix section to gain a general insight into a simple xFoil session. It is solely important to note that the wing section geometry has been derived by means of a trial version of AutoCAD, [9] and an auxiliary autoLISP script.

2.2. Neutral point location

Consider wing section shown in Fig. 1 (respect to Dr. F. H. Lutze, [10]). Aerodynamic forces are equal at either point along the chord including A and B:

(1) $L_A = L_B = L$

$D_A = D_B = D$

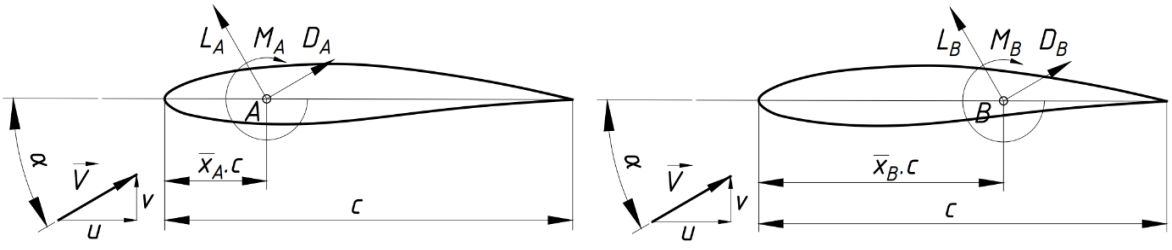

Figure 1. Aerodynamic forces and moments acting onto an airfoil

It is required to work out value of moment at point A given forces and moment at point B. To this purpose, one may compute equilibrium moment at an arbitrary point along the chord. For instance, moment at the leading edge, due to forces and moments acting at points A and B, is following:

(2) $M_{LE} = M_A - L \cdot \bar{x}_A \cdot c \cdot cos(\alpha) - D \cdot \bar{x}_A \cdot c \cdot sin(\alpha)$

$M_{LE} = M_B - L \cdot \bar{x}_B \cdot c \cdot cos(\alpha) - D \cdot \bar{x}_B \cdot c \cdot sin(\alpha)$

In eq. (2), both right hand sides are equal, hence the following equality

(3) $M_A = M_B + L \cdot (\bar{x}_A - \bar{x}_B) \cdot c \cdot cos(\alpha) + D \cdot (\bar{x}_A - \bar{x}_B) \cdot c \cdot sin(\alpha)$

On condition that angle of attack is small, $\sin(\alpha) \approx \alpha$, $\cos(\alpha) \approx 1$, and drag is much less than lift. Consequently, the rightmost term in (3) is second order of accuracy and might be omitted. After dividing by $0.5\rho V2Sc$ and assuming simplification mentioned, following dimensionless equation, also known as Rule for Transferring Moments, is obtained:

(4) $C_{m,A} \approx C_{m,B} + C_l(\bar{x}_A - \bar{x}_B)$

Rule (4) provides a mean for developer to change location of the reference point and recompute the pitching moment in succession. What is more, the rule is suited for calculating location of a particular point, namely neutral point a.k.a. aerodynamic center. An essential property of the neutral point is that the moment does not vary with regard to altering angle of attack. Having differentiated rule (4), it yields:

(5) $\frac{dC_{m,AC}}{d\alpha} = \frac{dC_{m,B}}{d\alpha} + \frac{dC_l}{d\alpha}(\bar{x}_{AC} - \bar{x}_B) = 0$

Therefore, the neutral point is located at (dimensionless fraction of section chord)

(6) $\bar{x}_{AC} = \bar{x}_B - \frac{dC_{m,B}}{dC_l}$

2.3. Reynolds number influence over drag polar

Reynolds number is an important factor affecting drag polar outline. Broadly speaking, as the Reynolds number becomes bigger, so does the lift coefficient, and so the drag coefficient declines slightly. This phenomenon might be accounted for by boundary layer transition, [11]. The laminar boundary layer is notable for low kinetic energy and prone strongly to separation and vortex formation. In this case, a smooth flow around the airfoil is less likely to be observed. The drag is high and the lift is low. Whenever Reynolds number exceeds a critical value, the transition zone moves to a new location well ahead of the separation point. The flow sticks onto the airfoil surface and lift increases.

3. Validation

xFoil is held in high esteem and regard for achieved computational accuracy and precision. In current research, testing the solver against exact flow cases is thought to be rather redundant with good reason. xFoil is supposed to have been validated prior to release. In addition, some test results were already compared with wind tunnel data at different Reynolds numbers by means of four noteworthy wing sections. The results might be found in page [12].

Given basic assumptions, the used numerical solver is accurate and precise enough. Hence, the exposé goes on to find numerical solution of the main problem.

4. Results

In xFoil, reference area of 1 m2 is assumed in advance while Reynolds number and chord length are to be explicitly filled in. The chord length might be set to 1 by toggling NORM command. The center of rotation is placed at section leading edge (XYCM dialog).

In following Table 1, values of aerodynamic coefficients, obtained after numerical analysis completion, might be found with regard to both wing sections.

Table 1. Aerodynamic coefficients at various angles of attack

	PIL15M825, Re = 0.250E+06			PIL12M850, Re = 0.250E+06		
alpha, deg	**CL**	**CD**	**CM**	**CL**	**CD**	**CM**
-5	-0.3433	0.01244	0.023	-0.2269	0.01373	-0.0358
-4	-0.2102	0.01185	-0.0139	-0.1024	0.01179	-0.0701
-3	-0.0853	0.01133	-0.0469	0.0112	0.01193	-0.0975
-2	0.0291	0.01105	-0.0755	0.1186	0.012	-0.1224
-1	0.1389	0.01097	-0.1022	0.2258	0.0121	-0.1473
0	0.2489	0.01091	-0.1291	0.3342	0.01223	-0.1731
1	0.3551	0.01098	-0.1544	0.4428	0.01229	-0.199
2	0.4635	0.01101	-0.1805	0.5528	0.01229	-0.2259
3	0.566	0.01092	-0.2038	0.6624	0.01228	-0.2524
4	0.6649	0.01071	-0.2249	0.7712	0.01267	-0.2787
5	0.8352	0.0109	-0.2792	0.8772	0.01305	-0.3037
6	0.888	0.01175	-0.2803	0.9757	0.01292	-0.3249
7	0.9186	0.01432	-0.2727	1.0596	0.01324	-0.3398
8	0.9574	0.01657	-0.2694	1.0919	0.01873	-0.3365
9	0.9914	0.01998	-0.266	1.1161	0.02365	-0.3296
10	1.0173	0.02473	-0.2611	1.1435	0.02905	-0.3263

In Fig. 2, drag polar is depicted (blue), so is the pitch moment coefficient (orange), for wing section PIL15M825. The angle of attack varies within -5° to 10°. In Fig. 3, similar graph is shown for PIL12M850. Maximum lift-to-drag ratio 76 … 80 is achieved at angle of attack 5° … 7°. Exact values are shown in the graphs.

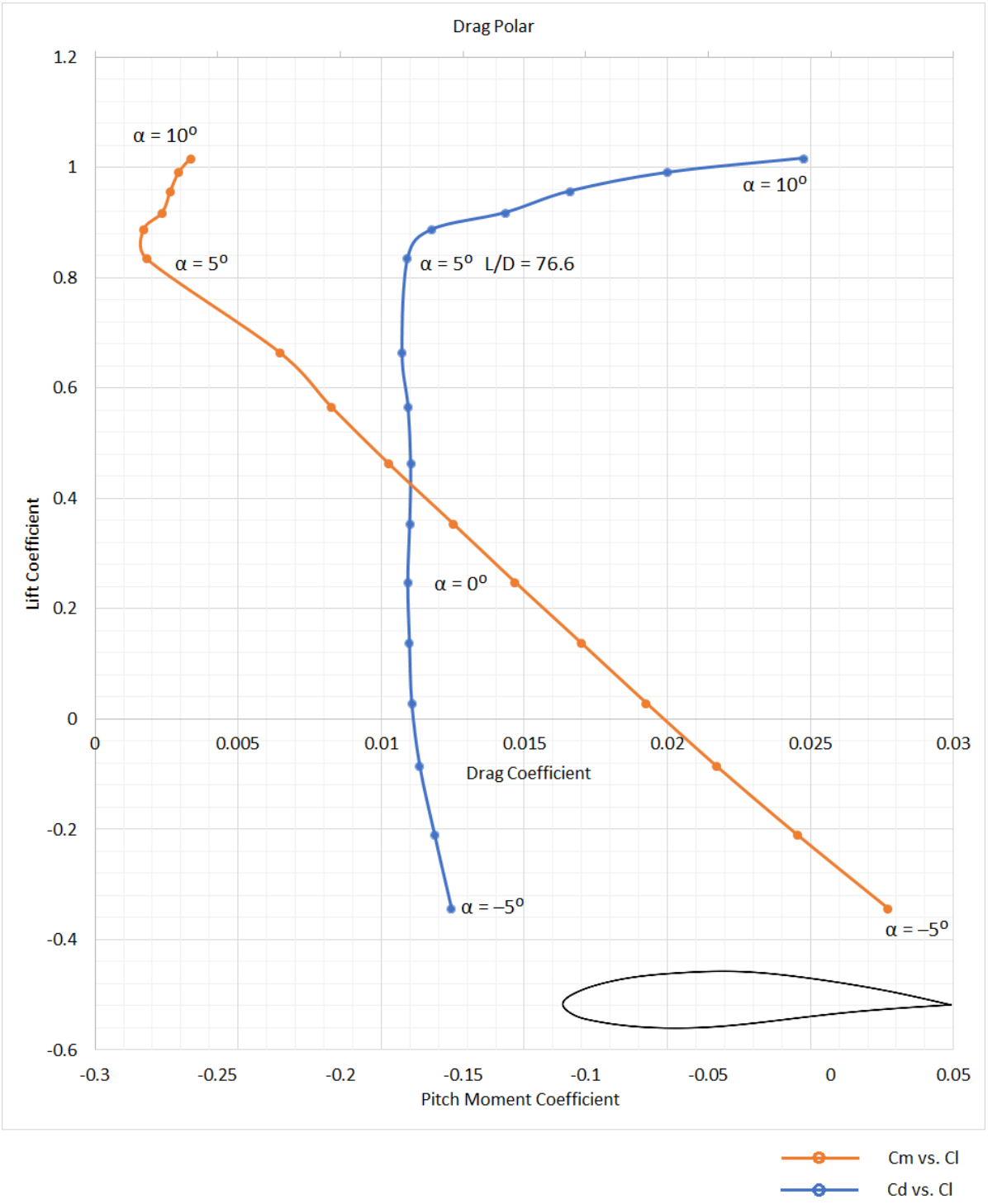

Figure 2. Drag polar, PIL15M825, Re = 0.250E+06

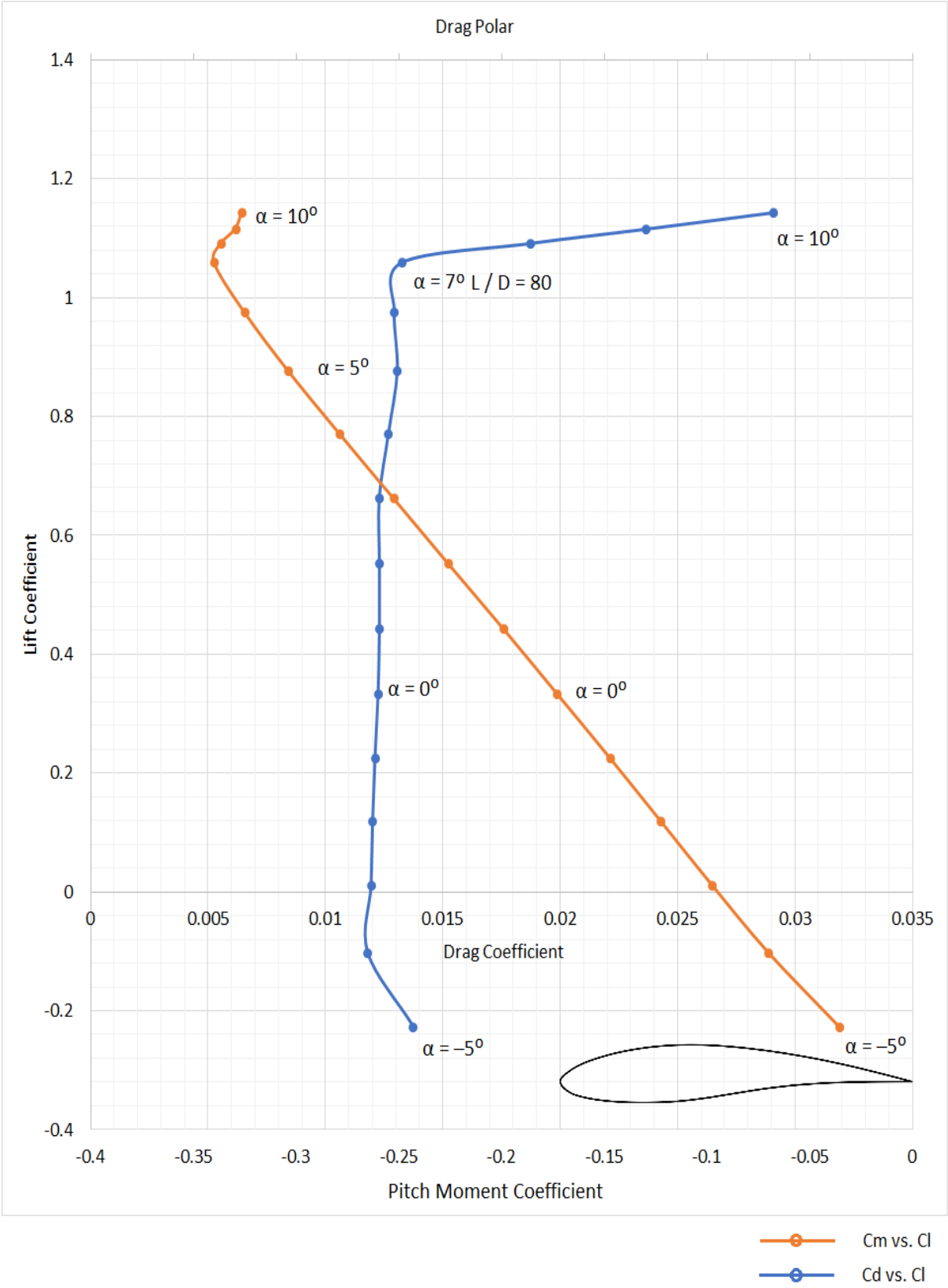

Figure 3. Drag polar, PIL12M850, Re = 0.250E+06

In Fig. 4, drag polar graphs are depicted at different Reynolds numbers for PIL15M825 wing section.

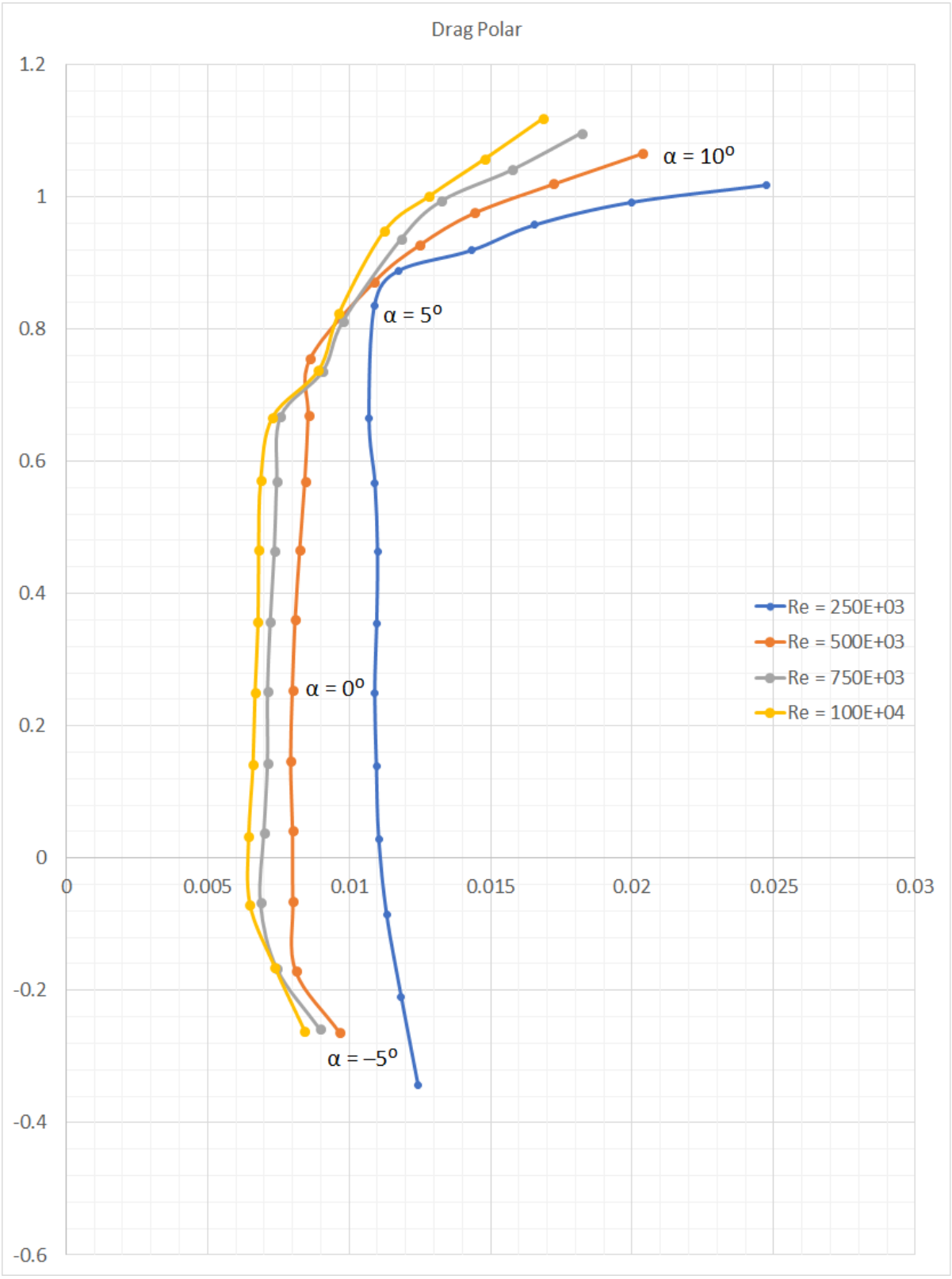

Figure 4. Drag polar curves with reference to Reynolds number, PIL15M825

In following Table 2, location of neutral point is reported. Both values were computed according to eq. (6). The reference center of rotation is $x,\bar{}_B = 0$. It was possible to work out value of derivative dCm/dCl for the simple reason that pitching moment coefficient changes linearly within wide range of values of angle of attack.

Table 2. Neutral point location

	PIL15M825	**PIL12M850**
$x,\bar{}_{AC}$ (times chord)	0.247	0.232

In following Fig. 5, static pressure coefficient contours are shown, Re = 250E+03. The angle of attack varies within -5° … 10° interval, hence multiple graphs. Abruptly changing curvature of the wing section contour (i.e. osculating circle radii raised to a power of -1) explains small ripples arising along each graph. In Fig. 5, positions of free transitions (top Xtr, bot Xtr) from laminar to turbulent boundary layer are displayed, so is transition criterion Ncr.

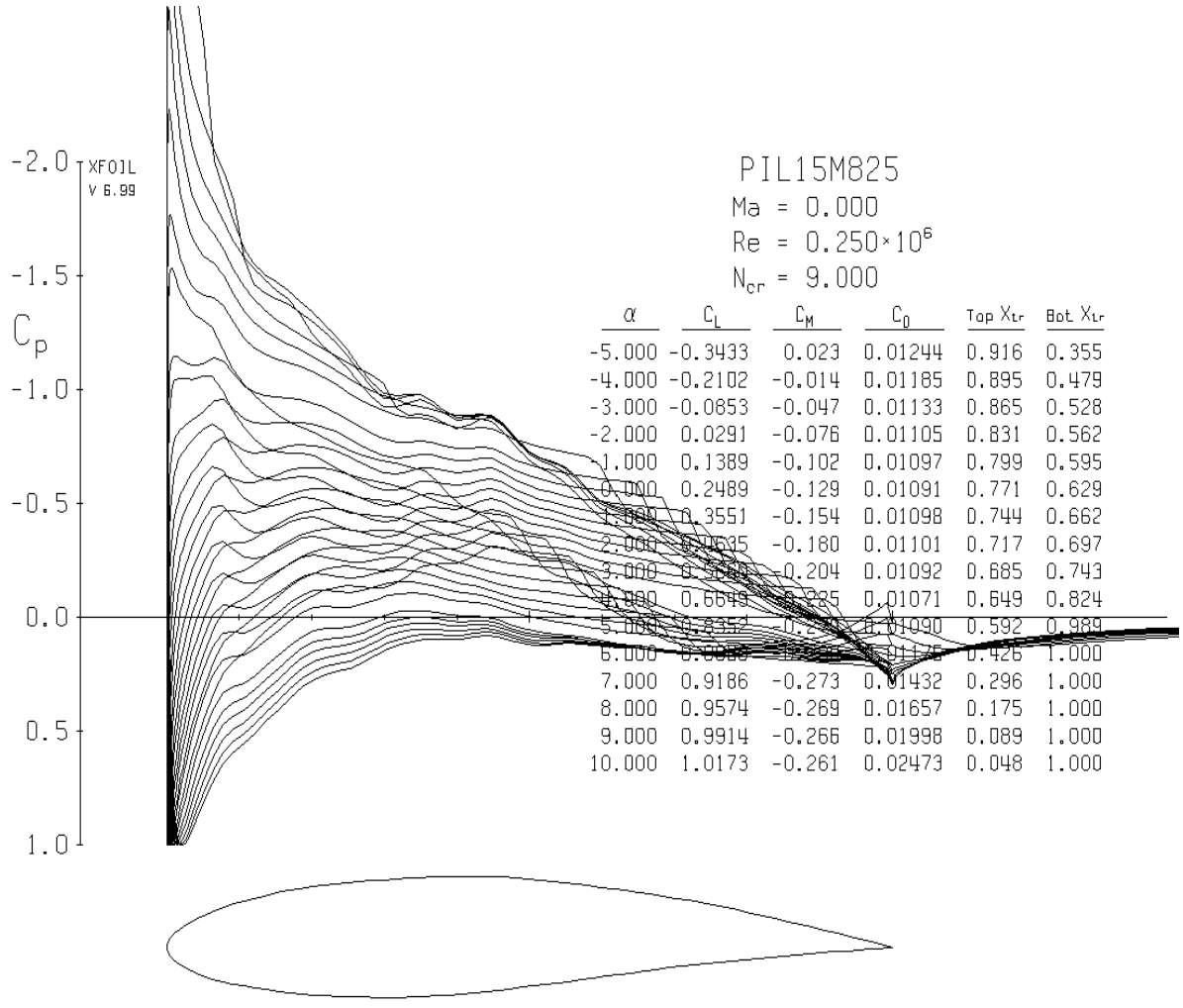

Figure 5. Pressure coefficient contours at various angles of attack, PIL15M825

5. Discourse

To decide to accept the leading edge (from among other points) as a reference point of rotation proved to be the best choice. According to experience, derivative dCm/dCl is liable to change its sign intensively as long as the reference point closes in on the neutral point location approximately at 0.25 times chord.

Prediction of boundary layer transition is another remarkable ability of xFoil. Two transition modes are supported: forced and free. In current case study, latter mode was adopted for obvious reason. Therefore, it is somewhat desirable for the project to keep on growing by experimenting with forced transition locations in terms of real surface roughness.

The research aimed to fill in the gaps currently existing in publicly available knowledge about Pilatus PC-9M aircraft.

References

1 Huang, A., Aircraft Load Models for a Pilatus PC-9 Based on Wind Tunnel Testing, A98-31707, para. 2.1, ICAS-98-7,6,1, AIAA, 1998
http://www.icas.org/ICAS_ARCHIVE/ICAS1998/PAPERS/761.PDF
2. Snowden, A., H. Keating, N. van Bronswijk, J. Drobik, A Correlation between Flight Determined Longitudinal Derivatives and Ground-based Data for the Pilatus PC 9/A Training Aircraft in Cruise Configuration, DSTO-TR-0937, AR № AR-011-205, 2000
https://apps.dtic.mil/sti/pdfs/ADA376020.pdf
3. https://m-selig.ae.illinois.edu/ads/coord_database.html
4. http://airfoiltools.com/
5. https://janes.migavia.com/che/pilatus/pc-9m.html
6. White paper, PC-9M, The Advanced Trainer Model Building Plan 1:25, Pilatus Aircraft Ltd.
7. https://web.mit.edu/drela/Public/web/xfoil/
8. Drela, M., xFoil: An Analysis and Design System for Low Reynolds Number Airfoils, Low Reynolds Number Aerodynamics, Springer – Verlag, Lec. Notes in Eng. 54, 1989
9. https://www.autodesk.com/products/autocad/free-trial
10. http://www.dept.aoe.vt.edu/~lutze/AOE3104/airfoilwings.pdf
11. Popov, M., Hydrodynamics, 2nd edition, “Technics” Publishing House, 1962, p. 323, in Bulgarian
12. https://aerofoilengineering.com/Validation.php

Nomenclature

V – free stream velocity
u, v – Cartesian components of V
ρ – fluid density
alpha – angle of attack
c – section cord
S – planform area
x – longitudinal coordinate
L – lift
D – drag
M – pitching moment
Cl – lift coefficient
Cd – drag coefficient
Cm – pitching moment coefficient

Superscripts:
– dimensionless value

Appendix. An exemplary xFoil session (abridged)

```
XFOIL c> load pil15m825.prn
...
XFOIL c> ppar
...
Change what? (<cr> if nothing else) c> N 160
...
XFOIL c> norm
Loaded airfoil will be normalized
XFOIL c> xycm
Enter new CM reference X r> 0
Enter new CM reference Y r> 0
XFOIL c> oper
OPERi c> iter
Current iteration limit: 10
Enter new iteration limit i> 400
OPERi c> visc
Enter Reynolds number r> 250000
...
OPERv c> aseq -5 10 1
```

Analysis of cyber vulnerabilities in civil aviation and recommendations for their mitigation

Evgeni Andreev, Dimitar Dimitrov

Naval Academy "Nikola Vaptsarov", Asst. Prof. in Department of Information Technology, Faculty of Engineering, Varna, Bulgaria, e.andreev@naval-acad.bg

Naval Academy "Nikola Vaptsarov", Cybersecurity student, Varna, Bulgaria, dimitar@gmx.us

Abstract: The article reviews the main attacks which affect aviation. The weaknesses in protocol codes and the threats are highlighted. Trends related to security problems and vulnerabilities at airports and air bases are presented. An overview and analysis of some of the most notorious aviation hacking attacks and their consequences is reported. The paper focuses on a possible man in the middle attack which can compromise the link between the aircraft and the communication base. A demonstration of man in the middle with the ASTERIX protocol is presented. As a result of the problem analysis, recommendations are proposed to mitigate these vulnerabilities and their impact. Innovative protection methods involving artificial intelligence and machine learning are outlined.

Keywords: *aviation, protocols, cybersecurity, cyber attacks, artificial intelligence*

1. Introduction

Although the COVID-19 pandemic has affected tourist aviation for years to come, together with all other branches of aviation, a total of $3.5 trillion is still generated to the world GDP. GDP is expected to grow by another $750 billion in 2021 [1]. Aviation is one of the main engines of the modern economy and one of the main pillars of any country's development. Aviation has various branches, both in the business industry and in the commercial, military, humanitarian, tourism and research industries. The success of aviation in business, tourism and commerce over other methods of transportation is due to the speed with which it is carried out the intended and many times faster, compared to sea transport. One of the most important factors in the efficiency of aviation in these areas is the advanced technology that enables its development. As technology advances, the logistical overload of ground control involving human intervention decreases. This allows for optimal air transport transfers so as to save time. Before the advent of modern technologies for air traffic control and logistics operations, additional time was needed to calculate and reconfigure flight plans. The advent of technology also brings risks of new threats that security professionals face every day. The risks of a technology outage or hacker attack could be fatal to some of the companies that rely entirely on technology and could result in tens of billions of dollars in losses. The speed at which malware and methods are improving leads to them quickly adapting to countermeasures taken by security professionals. These threats threaten both the metaverse and the physical world. If radar systems are

compromised, tracking aircraft will be uncertain and dangerous. A solution to the problem is the creation of new protocols and data encryptions to limit the interference of malicious actors.

2. Common attacks in aviation.

Frequency eavesdropping is common as the tools needed to do so are easily available. Communication channels are standardized on known frequencies, these are publicly available in aeronautical information publications. Since VHF radio communication is not encrypted, VHF communications are vulnerable to eavesdropping. Such as the main protocol in aviation Automation Device Specification – Broadcast (ADS-B) uses an unencrypted way to broadcast the information and is a publicly known protocol [2]. The unencrypted information allows sites such as flightradar24.com in Figure 1 and planefinder.net to make information about a large amount of public and military aircraft available online. This in itself is not dangerous, but provides the necessary information for malicious activities.

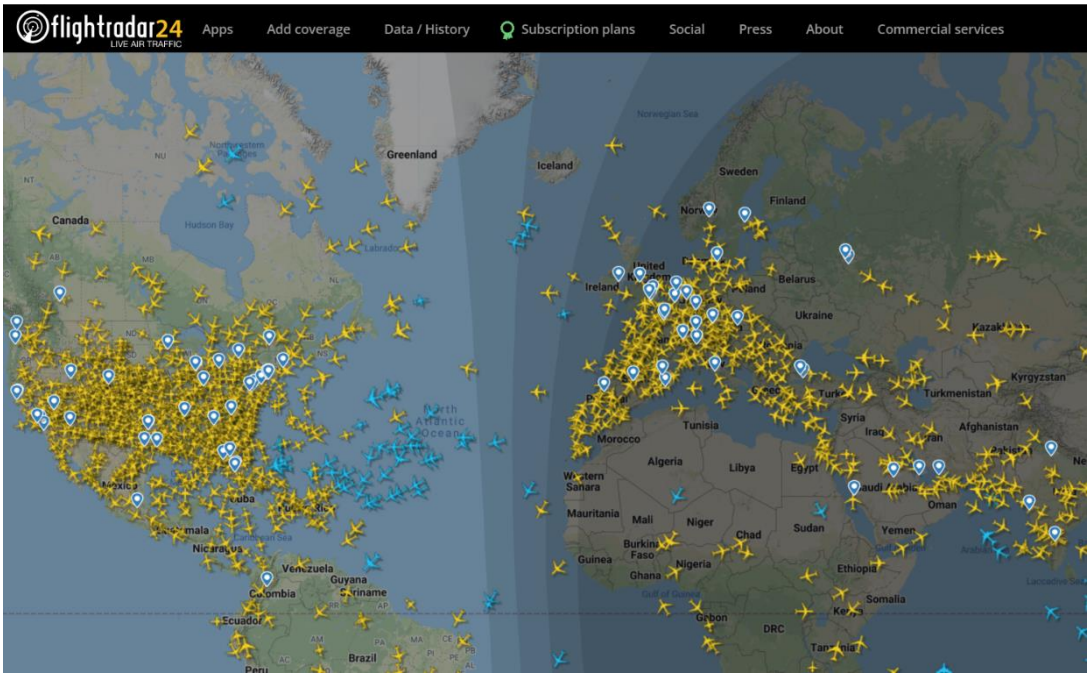

Figure 1. The website flightradar24.com, where a large number of civilian aircraft and some military aircraft can be tracked.

Jamming is another attack that is easy to perform. The requirements for implementing this attack are that it be executed from approximately close range to the communications base they intend to jam, or needs a strong power supply. This attack works by the method of Denial-of-Service (DoS) attacks - sending a continuous and large number of high frequency signals that fill the memory of the communication elements that try to process each signal [3]. As a consequence of filling the working memory with malicious and "junk" information and overloading it with processing, radar systems cease operation. It can affect most secondary radar systems as well as most non-military primary radar systems. Localization of this type of attack is done quickly because the frequency it emits is obvious to sensors and can be traced to the primary source. It is also possible to do this through an unmanned aircraft type system, which would also leave fewer traces. Such an attack was executed in

2015 by the Russian state-sponsored APT (advanced persistent threat) group Pawn Storm [4]. The consequences were hundreds of planes unable to take off in a 5 day period as the Swedish ATS (air traffic control) was constantly jammed.

One of the most dangerous attacks is Man in the middle. This is the attack that detects the connection between aircraft and ground control, modifies the connection and sends malicious code. Some of the most common methods of Man in the middle attacks are: ARP poisoning, DNS Spoofing, GPS Spoofing, Port Stealing and DHCP Spoofing. Spoofing attacks send a signal with information that works on the same principle as the data transmission protocol. The difference is that it sends fake information by impersonating the real sender. The GPS Spoofing method is one of the most impactful attacks as it a more intelligent form than jamming and jamming. This type of attacks aims to make the receiver take wrong coordinates, which makes it confuse the aircraft navigation system completely [5]. Data link layer has no implemented methods for identification and authentication of received command signals. This allows a spoofing attack to be carried out on the radio transmitters located nearby, sending false GPS signals into the target receiver. In this way, the attacker can control the navigation system of the aircraft and set his own target courses.

In combination with spoofing attacks and message deletion attacks it is possible to manipulate the ATC (Air Traffic Control) console. When a jamming signal is sent fast enough to cause constructive interference, it causes a large enough number of errored bits so that the received message is detected as corrupt and deleted. By overlaying the spoofed message with a higher power, this enables a spoofing attack to be sent.

Fake websites and phishing attacks related to airlines are the most common cyber attacks in 2020, accounting for 87% of reported cyber attacks in the airline industry, as can be seen in Figure 2. They are cheap, easy to spread and successful. Their main purpose is to steal data and sensitive information from airports and airbases, and from people who are lured by phishing sites. Phishing attacks can also spread malware that is more dangerous to an airport's IT infrastructure. In a ransomware attack, this could paralyze an airport's operations for days, even weeks.

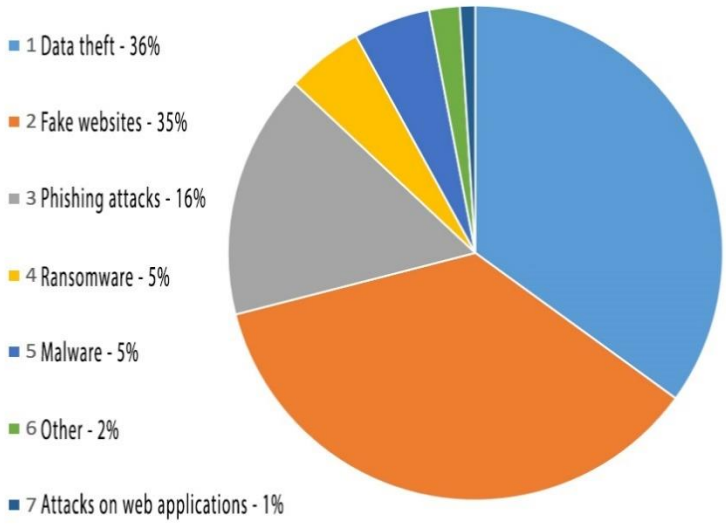

Figure 2. Chart of the most common attacks in the airline industry in 2020 [6].

3. Analysis of attack types and problems in civil aviation.

One of the first examples of a hacker attack that disrupted flights was in 2015. Following a DDoS attack on LOT Airport in Poland [7], many of the systems responsible for important flight operations were taken offline. The attack resulted in the suspension of 10 flights and directly affected over 1500 passengers. There is no evidence of data leakage or compromise of internal systems.

One of the most recent attacks on aviation infrastructure has been recorded in 2019 at the European International Airport. While installing a new Cyberbit anti-virus program, the Monero malware was detected, the purpose of which is to use the victim's computer configuration to be added to cryptocurrency mining cluster programs. After the Cyberbit report, it is found that more than 50% of the airport's systems are infected with this malware. In order to evade the airport's defenses, the Monero crypto malwareer uses PAExec, a version of Microsoft's PsExec, a program for remotely executing processes on other systems. This enables the malwareer to execute as a system mode, allowing it to gain maximum user privileges, i.e., use the full allowed resources of the airport's systems. Another feature that PAExec gives is priority over other programs to use the resources of the computer systems. In order to evade antivirus programs at the airport, a Reflective Dynamic-Link Library (DLL) type attack is used. It allows the injection of a malicious Dynamic-Link Library that is loaded into memory rather than the hard disk. This allows stealth persistence and evasion of antivirus sensors. The malicious activity detection data shown in Figure 3 and Figure 4 were taken using Google's online virus scanning tool, VirusTotal. VirusTotal scans files across many antivirus companies, indicating how many of them detect malicious activity and what type it is. An experiment was done by scanning the crypto malware Monero through VirusTotal. Figure 3 shows the result from the fall of 2019 where more than 57 antivirus did not detect malicious activity and only 16 were able to detect the malicious file . Figure 4 shows how as the number of incidents related to the Monero malware increases, the number of antiviruses not detecting malicious activity is 26 out of 69 as of March 2022. According to official data, the consequences of this attack are a slowdown of computer systems and an increase in power consumption. However, this malware is classified as a medium-level attack vector as it enables the attacker to perform a wide range of actions. It enables downloading other malicious payloads and compromising entire networks. In the worst case, this type of attack would compromise critical operational networks, from runway lights to the airport transportation system.

Figure 3. Malware file analysis by VirusTotal. September 2019 [8].

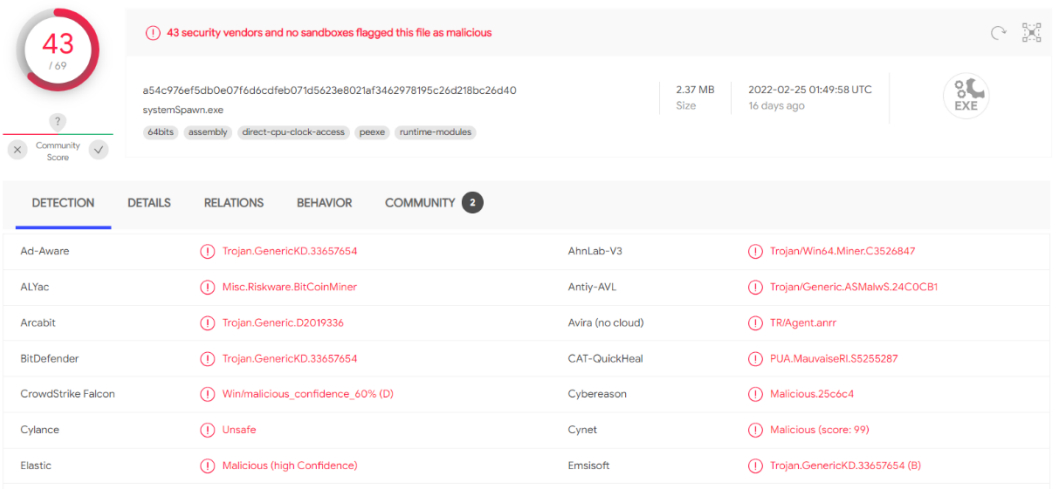

Figure 4. Malware file analysis by VirusTotal. March 2022.

A sample file [9] for eavesdropping traffic over the ASTERIX protocol is examined. The file has been analyzed using Wireshark network protocol analyzer and capture software. In order for an attacker to be able to read the information transmitted between an aircraft and the control center, they must tap into the network between them. The aircraft sends information to the ground radar. The information is processed and sent, via the ASTERIX protocol (All Purpose STructured Eurocontrol SuRveillance Information Exchange) through many network devices to its final destination - the control center. There the information is processed and displayed to make decisions. The problem arises in the communication path from the encapsulation of the information, via the ASTERIX protocol, to the decapsulation of this information. Traffic from one point to the other can be intercepted. Figure 5 shows eavesdropped traffic containing information sent in ASTERIX packet format. Initially the information is encrypted and cannot be understood, for the reason that Wireshark displays the information transmitted through the UDP(User datagram protocol) data transmission protocol. From the file it is possible to understand the IP from which the packets come and the IP to which they are destined. All addresses use different UDP ports for communication and are of different sizes.

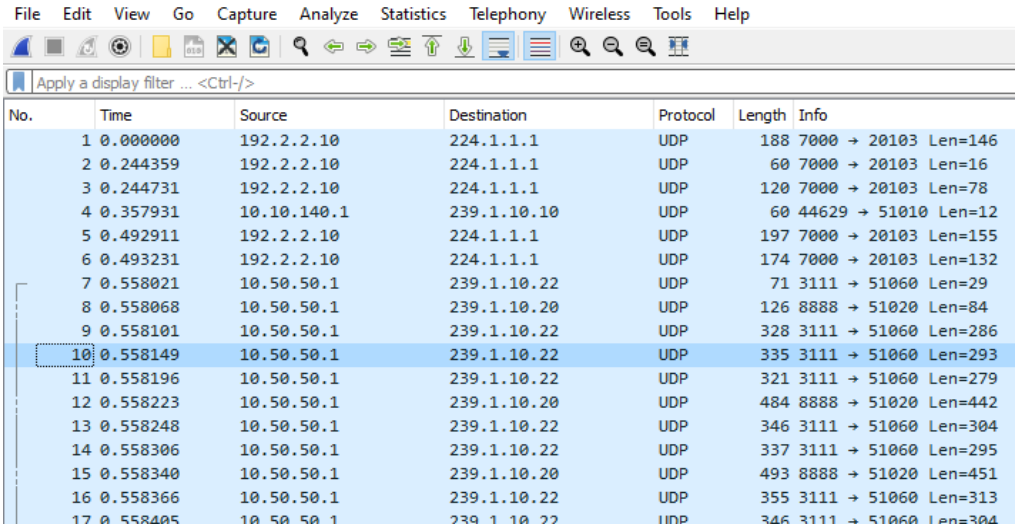

Figure 5. Eavesdropped traffic containing a message encoded using the ASTERIX protocol.

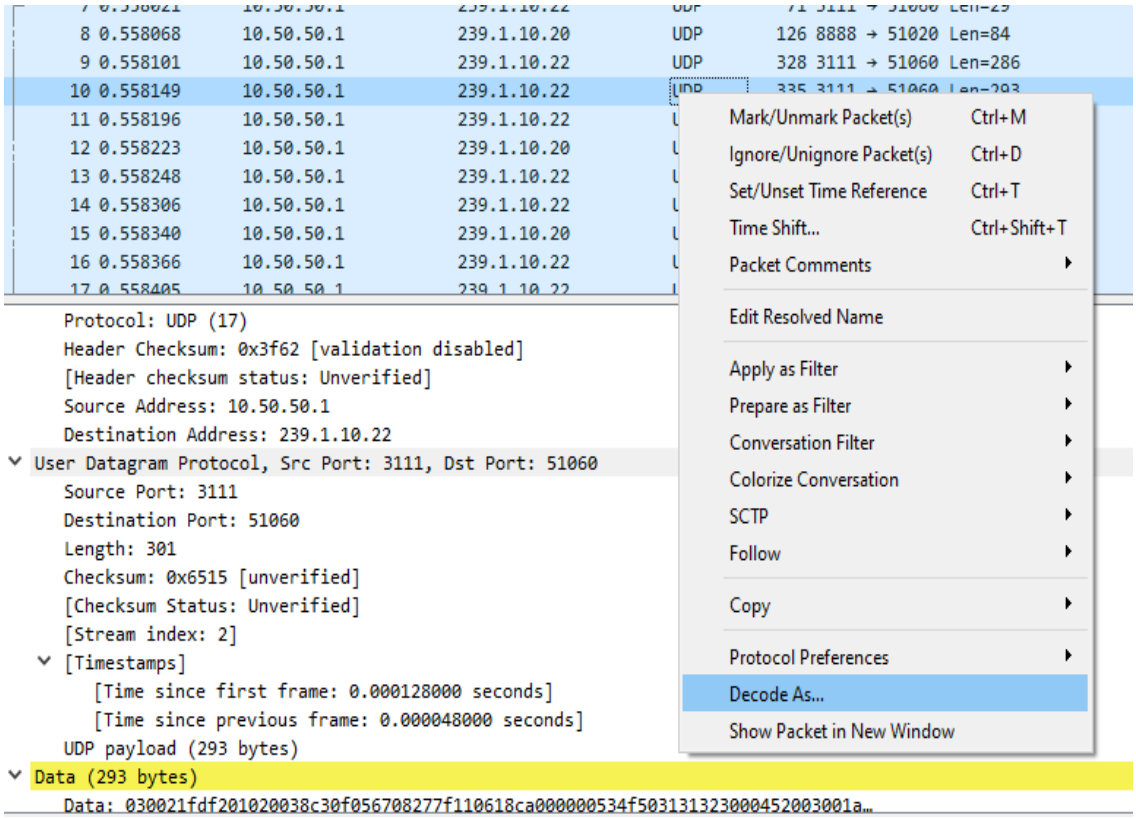

Figure 6. Selection of functionality for information decoding.

Figure 6 shows the ability to decode information from UDP to the ASTERIX protocol. The information contained in the tenth packet is completely unreadable. Using the decoding functionality of Wireshark, we choose to convert it to the ASTERIX protocol.

Figure 7 shows how Wireshark's decoding functionality converts UDP protocols into ASTERIX protocols.

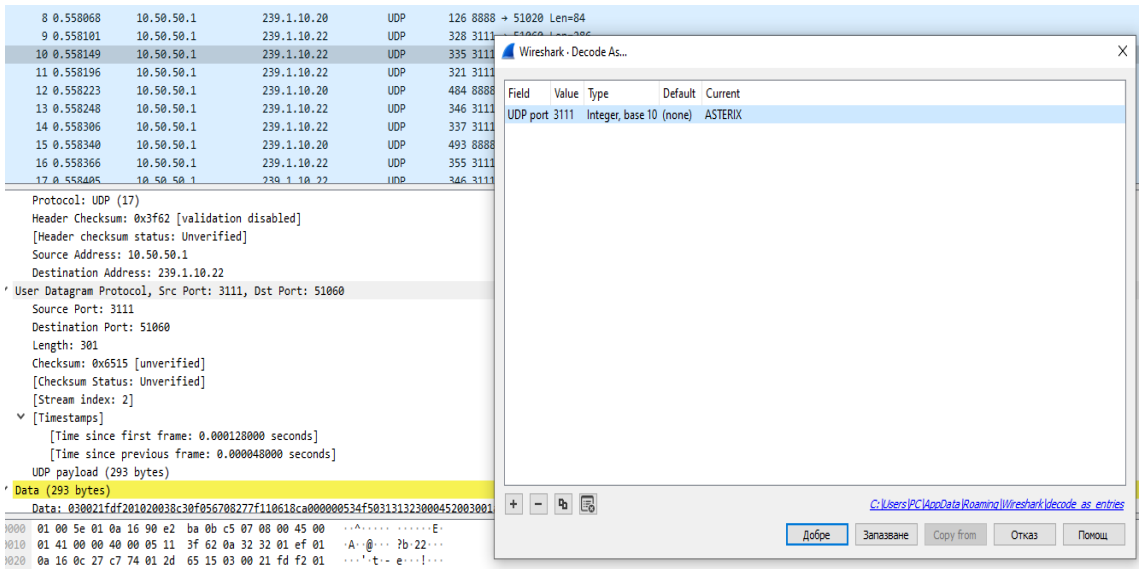

Figure 7. Decoding a UDP packet to the ASTERIX protocol.

After decoding, the filtered information can be converted to ASTERIX format. The detail information that has been transmitted, can be seen to be analyzed, changed and resent in Figure 8.

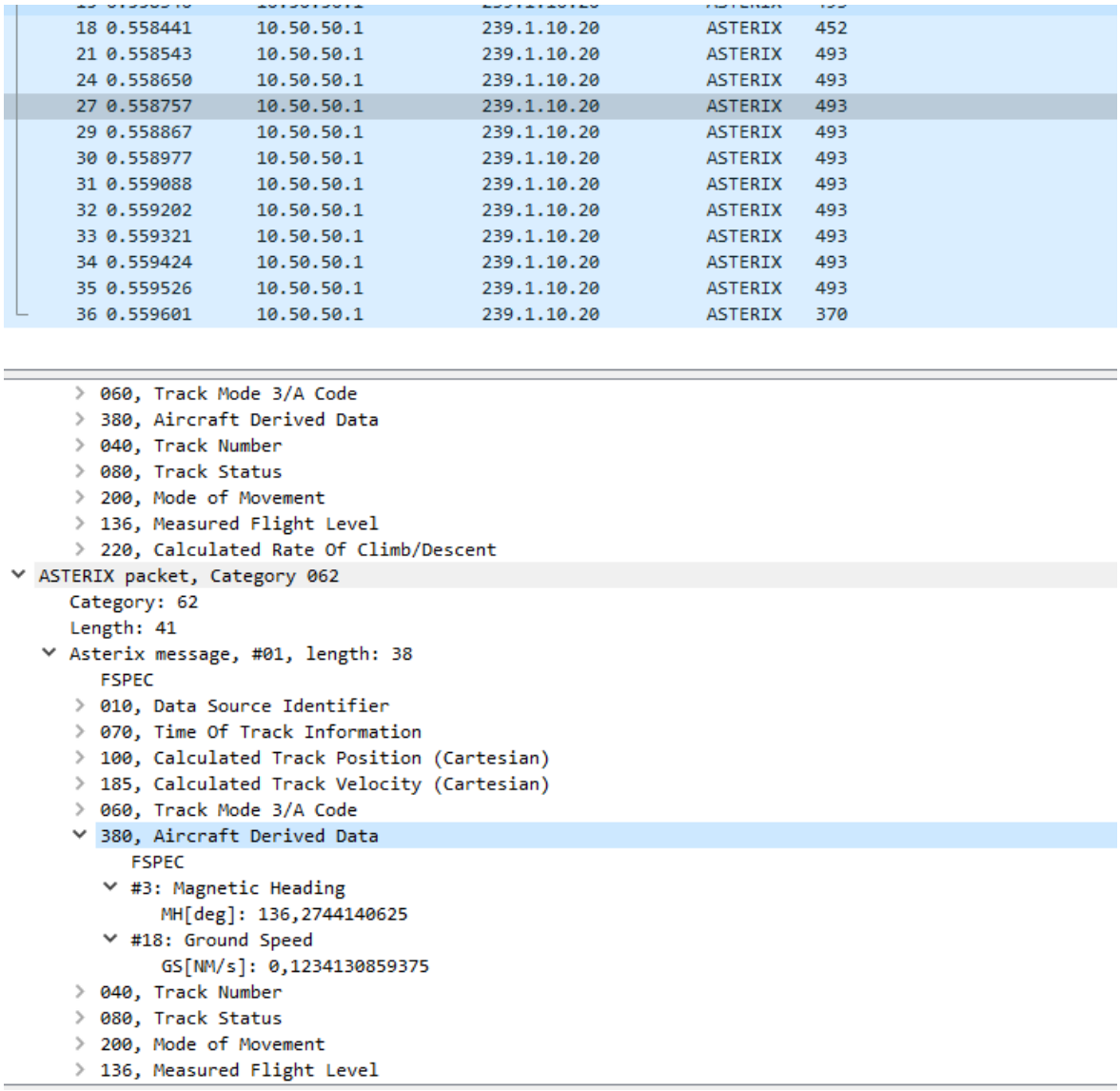

Figure 8. Detailed analysis of the ASTERIX package.

The data shown in Figure 9 has been filtered to show only from category 062 [10]. This makes it possible to filter the network packets only by packets that are for the aircraft system report.

Some of the problems do not come directly from attacks, but from problems in the software code. An example of this is the July 2020 bug in the UK airline TUI's software that confused the naming of "Miss" and "Ms" [11]. This gives a systematic error that identifies people who use the Miss designation as children and sets their weight at times less than the actual weight. This is a prerequisite for confusing the calculations of aircraft load in flight and gives the possibility of fatal consequences.

Examples of miscalculated aircraft loads ending in fatality include Cubana de Aviación's Field 972 in 2018 and a Fine Air Douglas DC-8 flight in 1997.

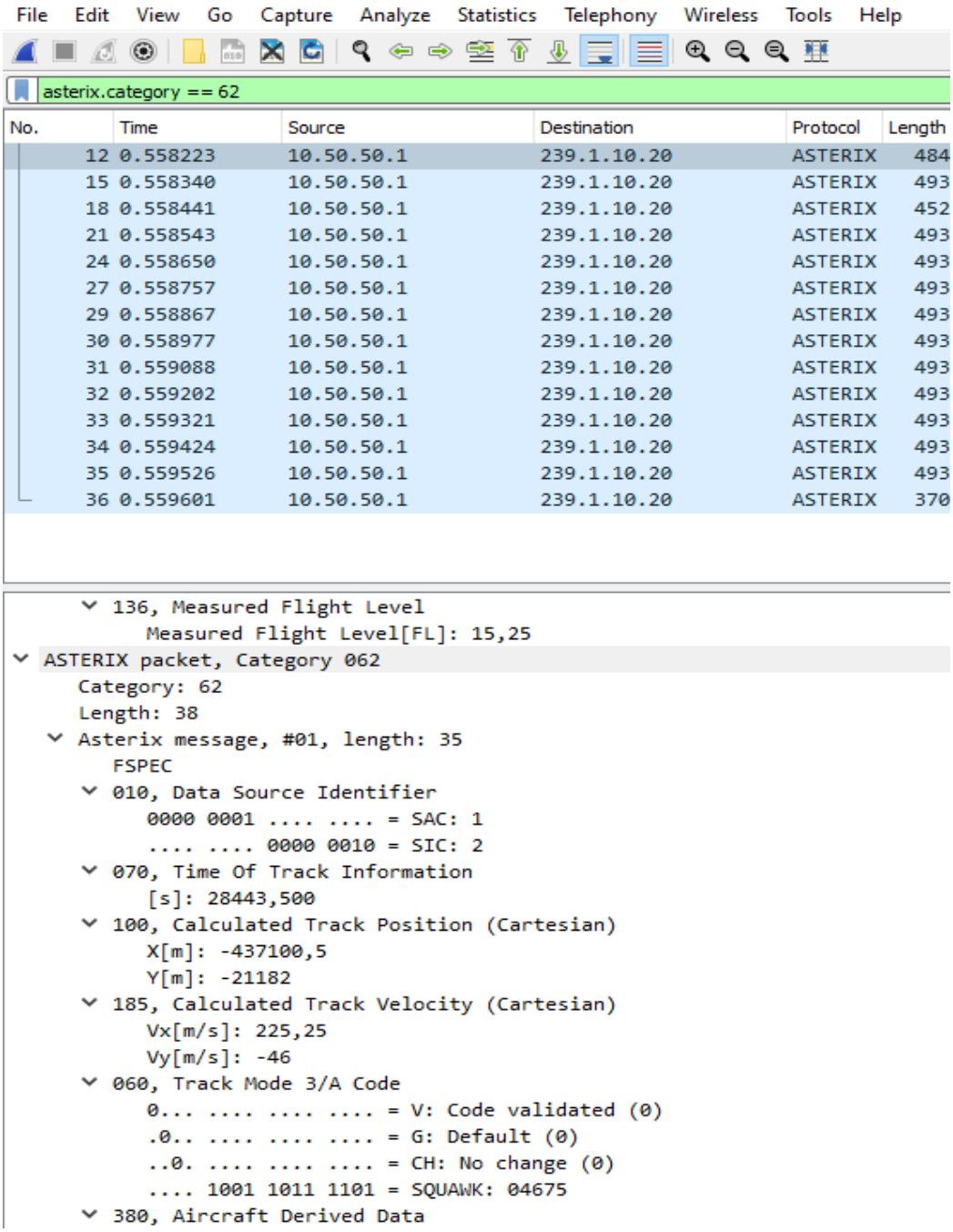

Figure 9. Filtering by category 062 of the ASTERIX protocol.

A report on the problem later revealed that this problem was first identified on July 10, 2020, when three passengers identified themselves as Miss and were registered as children in the program. Airline staff noticed the problem and resolved the issue manually. An unsuccessful attempt by the developers to fix the problem followed. 11 days later, the third, and last, TUI Airways flight BY-7226 with such a problem takes off with 167 passengers on board, 65 of them children. It was

subsequently learned that there were in fact only 29 children. If this bug is discovered by hackers, it could turn into a zero-day attack and lead to a fatal end.

4. Recommendations and protections

Based on the analysis of attacks in Section 3, recommendations have been made to mitigate this type of malicious activity:

1. Eavesdropping using tools like WireShark can be avoided by using a VPN. The VPN would allow encryption of the data on both sides and so the data intercepted by Wireshark would be useless as the VPN encrypts the data and makes it impossible to decode.
2. Implementing an identification and authentication step after the date link layer of the ADS-B receiving protocol would prevent man in the middle attacks.
3. Optimize systems control. Provide reliable encryption, authorization, and authentication methods. Limit redundant access to highly sensitive computer configurations.
4. Cybersecurity training for teams working on and off airbases and airports. The goal of the training is to improve information security literacy to avoid insider attacks.
5. Prohibiting the use of any personal devices on airports and airbases. This is to protect against an already infected device that, when connected to the airport or airbase network, could spread or gain access to sensitive information.
6. The application of artificial intelligence would solve a large percentage of external and internal cyber threats. Using databases of various cyber threats already created by many different institutes, artificial intelligence could detect and block malware in the fastest and most optimal way. Artificial intelligence and machine learning can process large amounts of information in a short amount of time, making them favorites over conventional methods of defense. By building a neural network to analyze the performance of every suspicious file in systems, artificial intelligence avoids the weakness of "cloaking" some viruses, allowing them to be hidden from normal antivirus and firewalls. Another important advantage of artificial intelligence is that it can redirect resources to weak spots in a computer system when it is attacked. It will be possible to predict how and where defenses are most likely to be compromised, and a plan will be devised to redirect resources to address weaknesses. The use of artificial intelligence is critical to understanding the impact of various infosecurity programs and reporting relevant information to all stakeholders.

5. Conclusion

The continuous development of information technology and engineering has led to its integration into many of the systems used in aviation. This leads to the optimization of flight logistics and the handling of technical details. It also makes operators dependent on the help of modern software tools and leads to new threats. Over the last decade, we have seen a dramatic increase in cyber attacks,

both on business areas as well as military and aviation infrastructures. Cyber attacks are fast, effective and cheap. With the development of the Dark Web and cryptocurrencies, these attacks are becoming more accessible. All of this determines the danger of this type of malicious activity. The aviation industry is prone to this type of attack as they operate with billions of dollars of capital and at the cost of passenger safety. In order to be prepared for future cyber incidents, airport and airbase personnel should receive cyber security training. This would limit the impact of this type of attack. The implementation of artificial intelligence is of utmost importance for the development of cyber security of such key infrastructures.

References

1. “Aviation: Benefits Beyond Borders global report”, Aviation Benefits Beyond Borders, 2020
2. Wu Z., S. Tong, A. Guo, “Security issues in automatic dependent surveillance - broadcast (ads-b): a survey”, IEEE Access 2020, 8, 122147 - 122167
3. Mauro L., E. Piracci, G. Galati, “ADS-B vulnerability to low cost jammers: risk assessment and possible solutions”, 2014 Tyrrhenian International Workshop on Digital Communications - Enhanced Surveillance of Aircraft and Vehicles (TIWDC/ESAV), 2014
4. Gary K., J. P. Craiger, "Aviation cybersecurity: An overview", 2018
5. Andrew J. K., D. P. Shepard, J. A. Bhatti,T. E. Humphreys, “ Unmanned Aircraft Capture and Control Via GPS Spoofing ”, Special Issue: Special Issue on Low Altitude Flight of UAVs, Issue 4, 617-636
6. EUROCONTROL EATM-CERT Services, 2020, 12
7. Arjun K., “Hack attack leaves 1,400 airline passengers grounded”, CNBC, 2015
8. Sergiu G., “European Airport Systems Infected With Monero-Mining Malware”, Bleeping Computer, 2019
9. Wireshark, “Asterix”, https://wiki.wireshark.org/ASTERIX
10. European organisation for the safety of air navigation, “Eurocontrol standard document for surveillance data exchange. Part 9 : category 062. Transmission of system track data”, 2002
11. Thomas C., “Airline software super-bug: Flight loads miscalculated because women using 'Miss' were treated as children”,The Register, 2021

On the phenomenon of a light sphere in an inclined air jet

Vladimir Savov

Bulgarian Air Force Academy, Faculty of aviation, D. Mitropolia, Bulgaria, vladsavov@yahoo.com

Abstract: The article offers an explanation of the phenomenon of suspension of a light sphere in an air jet. The incompleteness of the widespread explanations based on the Bernoulli equation and the Coanda effect is shown. An explanation including the existence of a stall zone has been proposed and it has been shown that the Bernoulli equation and the Coanda effect have an indirect effect by shifting the stall area. The validity of the proposed logic is partially proved by comparing the constructed flow picture with the actual one obtained by schlieren photography.

Keywords: *turbulent jet, hydrodynamic levitation, Bernoulli equation, Coanda effect*.

1. Introduction

Somewhere in the early 1990s, on a visit to the AFA “G. Benkovski” was the President of the Republic of Bulgaria, Dr. Zh. Zhelev. As is usual during such visits, the officials get acquainted with the training facilities of the School. The Aerodynamics Laboratory was represented by the Head of the Aerodynamics Department, Colonel Krassimir Dimitrov, a first class military pilot, an instructor for all types of conditions. At the presentation of the laboratory, Colonel Dimitrov demonstrated the hanging of a ping-pong ball in a inclined air jet. The author of this article has shown this experiment many times, including to his children, and the usual reaction is, "Well, so what?" However, Dr. Zhelev, as a man of scientific thinking, was sincerely interested in the paradoxical behavior of the ping-pong ball and asked Colonel Dimitrov: "Could you explain this phenomenon to me, Mr. Colonel, but somehow simpler, as for a head of state?” Krassimir Dimitrov is a man with a sound judgment of circumstances and people, and therefore his answer, "In science, Mr. President, there are no royal roads." was by no means a show of disrespect, but result of his natural sense of humor, his broad general culture, and a hint to the Dr. Zhelev's scientific background. Of course, as a scientist-philosopher, Dr. Zhelev knew the famous phrase attributed to Euclid that there are no royal roads in geometry, he burst out laughing and did not stop laughing until he and his entourage left the aerodynamic laboratory.

After this sketch was thoroughly and irrigatingly discussed at informal meetings of the department, the question somehow arose: "Do we really know the explanation of this phenomenon?". Of course, the standard explanations are widely known, but a more detailed analysis raises a number of questions. Since then, the author of this article has repeatedly returned to them and become convinced that this is one of the cases of popular misconcepts in aerodynamics [1].

2. Explanation of the phenomenon of a light sphere in an air jet

2.1. Description of the phenomenon

A ping-pong ball is placed in a vertical air jet (for example, from a hair dryer). The jet impacting from below "holds" the ball in the air, and since, unlike in Fig. 1, in the real experiment the jet is not visible, the ball appears to "levitate". It is intuitively clear that the pressure force from the jet balances the weight of the ball. The ball oscillates laterally, but does not fall out of the jet, but self-centers. If we start to tilt the jet, the ball does not fall, but up to an angle, for example of 45^{o}, remains in the jet, which is surprising (Fig. 1).

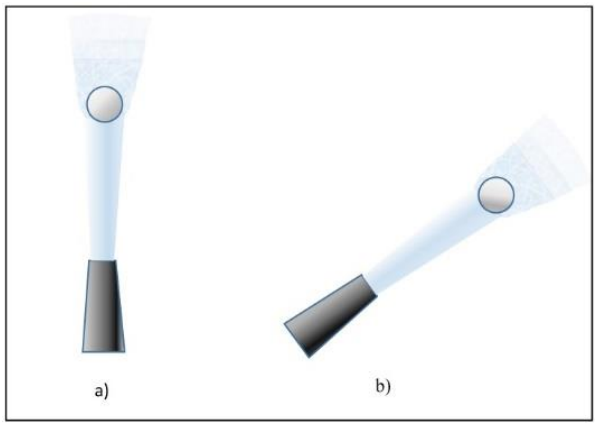

Figure 1. Light sphere in an air jet: a - vertical, b – inclined

A meaningful explanation of this phenomenon should answer the following questions:

- Why the ball does not fall when the jet is vertical?
- Why the lateral oscillations do not throw the ball out of the jet, but it self-centers?
- Why doesn't the ball fall off when the jet is tilted?

2.2. Existing widespread explanations

In some older publications [2] the suspension of the ball in the jet when the jet tilted is based on the direct applying of Bernoulli equation. When the jet is tilted, the ball moves to the side and the streamtubes of which the jet consists are deformed, as shown in Fig. 2. In the narrow part of the streamtube air velocity increases and according to Bernoulli equation pressure decreases, sucking the ball in the jet.

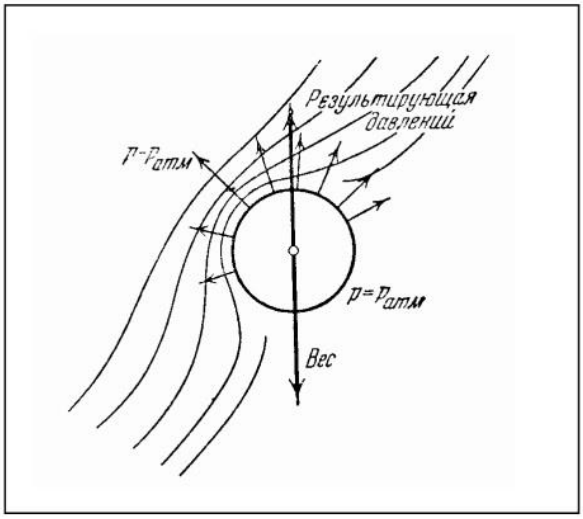

Figure 2. Explanation of the phenomenon ping-pong ball in an inclined air jet [2]

Such a flow picture, however, corresponds to an ideal fluid with no viscosity. In real air, in the back side of the sphere, the flow separates from the surface of the sphere and as such, this explanation is not correct.

In other sources [4] the explanation of the phenomenon under consideration is based on the Coanda effect . The effect of Coanda is that a free jet in a viscous fluid near bent surface adheres to the surface (Fig. 3).

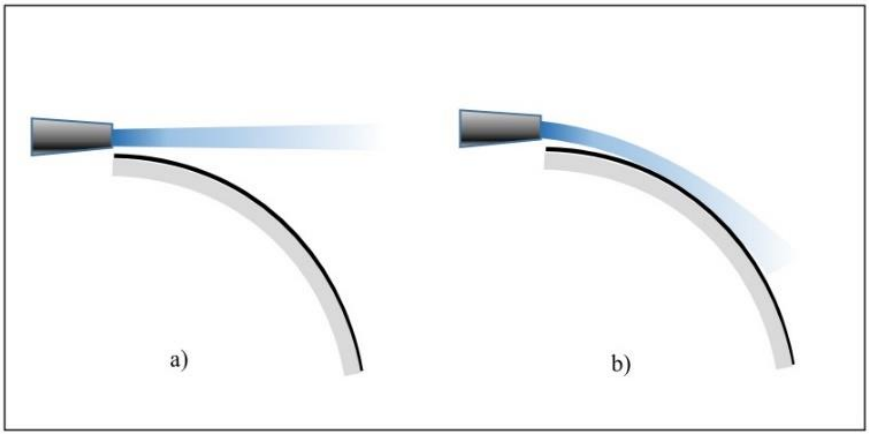

Figure 3. Coanda effect: a - jet in an ideal medium, b - jet near curved surface in a real medium

The explanation of the phenomenon under consideration, based on the Coanda effect, suggests that the jet adheres to the surface of the sphere. The jet bends (Fig. 3). If we think of the jet surface as a streamtube, we can apply the analogy between the behavior of streamtubes and rubber tubes [5]. When the rubber tube "bends", the cross-sectional area decreases, the speed increases, and according to Bernoulli's equation, the pressure decreases. The resulting low pressure balances the force of the weight and the ball remains sucked to the jet (Fig. 4).

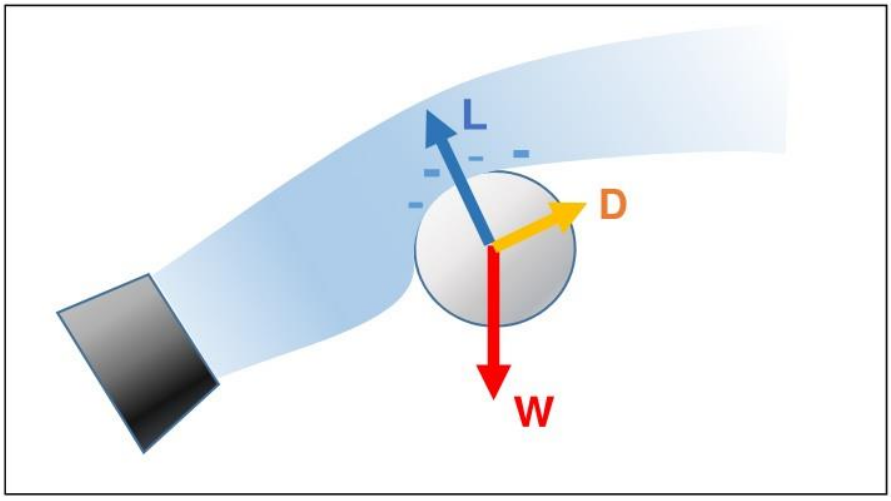

Figure 4. Coanda effect in case of a light sphere in an inclined jet

Indeed, with a jet of small diameter (compared to the diameter of the ball) this is the case (Fig. 5).

Figure 5. Light sphere "glued" to water jet due to the Coanda effect [3]

However, studies on the degree of manifestation of the Coanda effect at different ratios of jet thickness and sphere diameter [6] show that the jet adhere to the surface at ratios $\frac{h}{d} \leq 0.5$ (Fig.6). In the case of thicker jets, an initial pressure decrease is observed under the adhered jet, after which the jet separates from the surface. This leads us to think that the formation of a stall zone with reduced pressure should be taken into account for jets with a larger diameter.

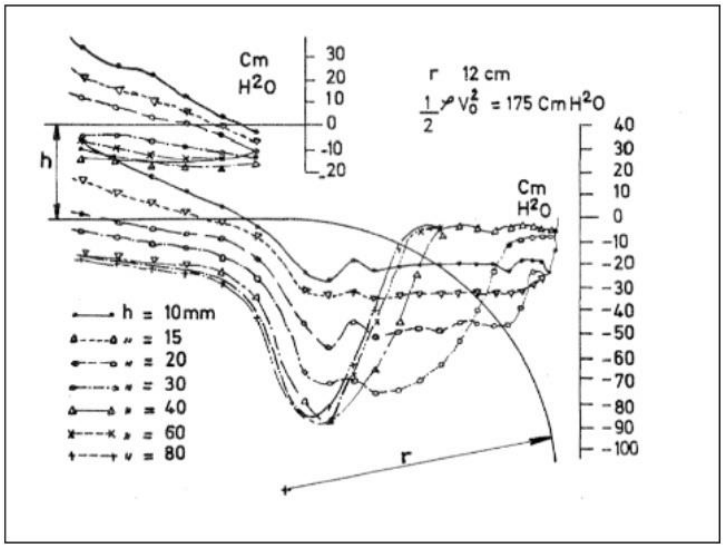

Figure 6. Jet thickness influence on the pressure distribution on a cylindrical surface [6]

2.3. Explanation taking into account the existence of flow separation zone

One of the factors to consider in the explanation is that the air jet is turbulent. The jet expands to establish inner pressure equal to the ambient one, and the airspeed decreases due to turbulent friction and the ejection effect on the ambient air (Fig. 7). The kinetic energy of the flow along the jet decreases. The Bernoulli equation, which is derived from the assumption of no viscosity, cannot be applied to the jet.

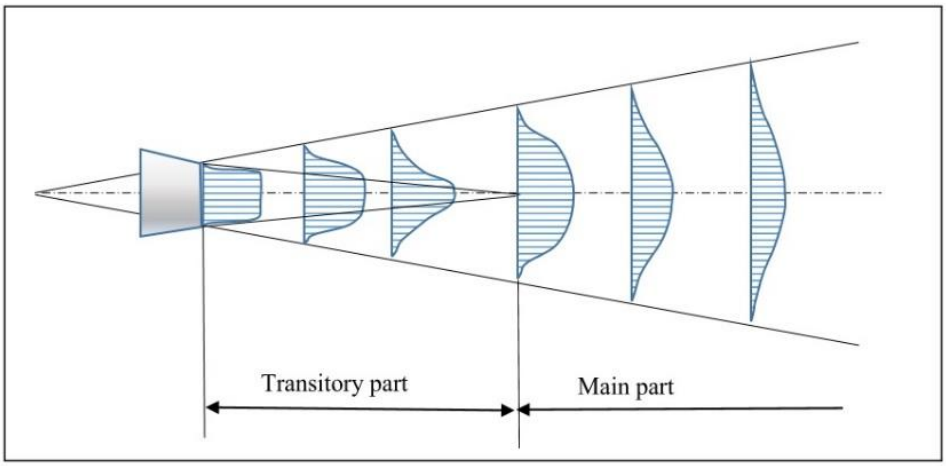

Figure 7. Mean velocity distribution in a free turbulent jet

Based on the assumption that the flow around the sphere implies the existence of a stall zone, the author offers the following answers to the above questions.

About the suspension of the ball in a vertical jet. When the jet diameter is small, the layer formed in the flow around the sphere has a small thickness and as such is subject to Coanda effect (Fig. 8a).

There is no separation of the flow and the weight of the sphere is balanced mainly by the friction forces in the boundary layer. With a larger jet diameter, the layer surrounding the sphere has a large thickness and separates off in the rear (upper) part of the sphere. The increased pressure at the front critical point and the reduced pressure in the stagnant zone create a significant force of pressure drag, which balances the weight of the sphere (Fig. 8b).

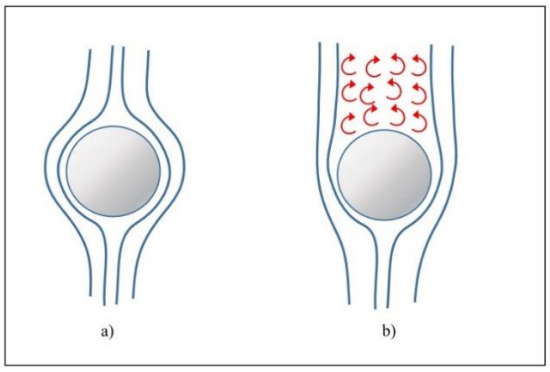

Figure 8. Vertical jet flow picture: a - for small diameter jet, b - for a jet with a larger diameter

About the "self-centering" of the ball in a vertical jet. Turbulent disturbances in the jet cause transverse motions of the sphere. If we have a shift of the sphere to the right, the layer to the right of the sphere thins and due to the Coanda effect sticks to the surface of the sphere. The stall point on the right is shifted backwards. The layer to the left of the sphere thickens and the separation point moves forward. The asymmetry of the detachment zone creates a pressure force that returns the sphere to the neutral position (Fig. 9). In addition, the pressure difference is exacerbated by the uneven velocity distribution along the radius of the turbulent jet - at higher velocities in the central part, the pressure diminishing in the narrowing of the streamtubes is greater than the diminishing in the outer streamtubes, where the velocity in the undistorted jet is less.

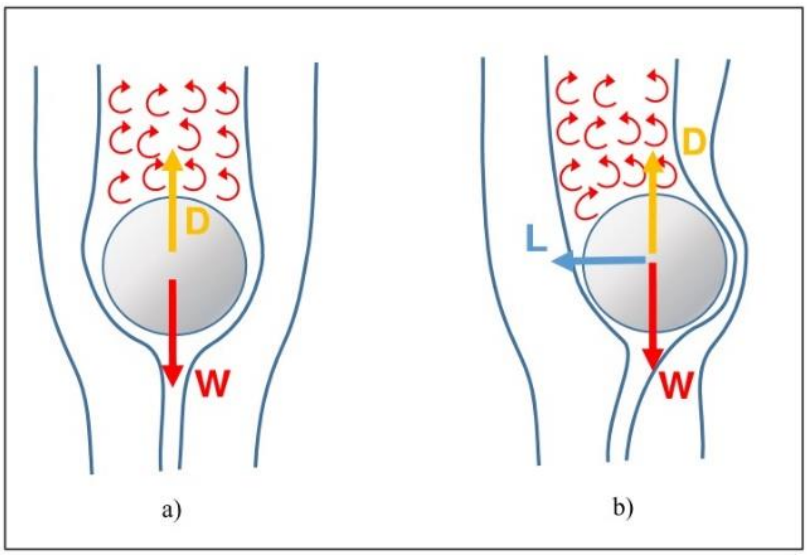

Figure 9. "Self-centering" of the sphere in a vertical jet

Regarding the suspension of the ball when tilting the jet. When the jet is tilted, the weight shifts the ball to the side and the logic of the explanation is similar. The weight of the ball is balanced by the sum of the lateral force and the drag (Fig. 10).

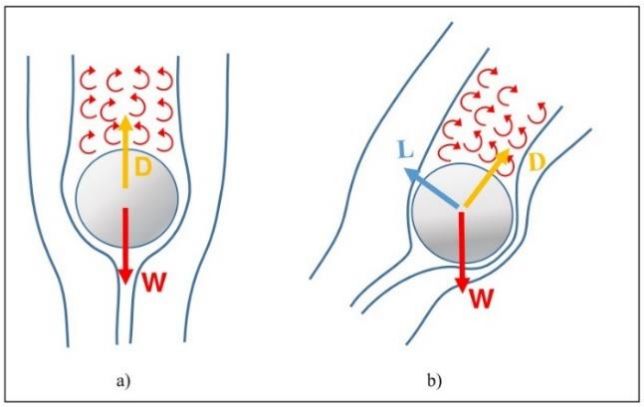

Figure 10. Зависване на сферата в наклонена струя

In order to test the above hypothesis, visualizations of the flow were used obtained by another author for a jet of hot air [4] with the help of schlieren optics (Fig. 11).

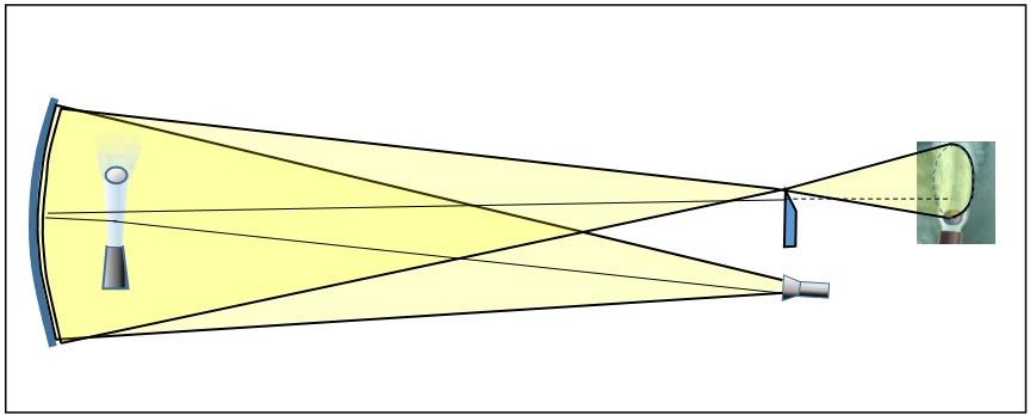

Figure 11. Schlieren optics with concave mirror

Fig. 12 shows the real pictures of the flow in the case of a sphere in a vertical and inclined jet.

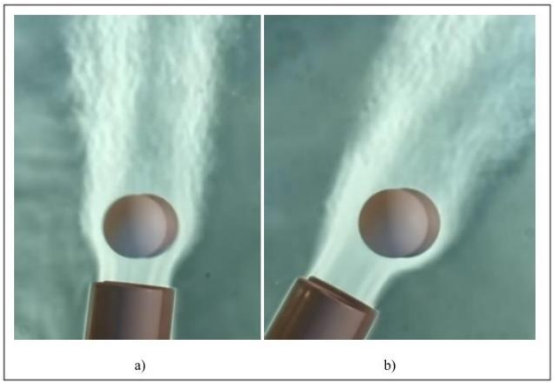

Figure 12. Schlieren photography of the flow in vertical (a) and inclined (b) jets [4]

3. Conclusion

The flow patterns shown in Fig. 10 were proposed by the author of this article before the photographs of Fig. 12 were available to him. The good similarity between the speculative picture of the flow and the real one in first approximation justifies the logic of the above considerations. Both Bernoulli equation and the Coanda effect have a place in the constructed explanations, but not directly, as in the standard explanations of the phenomenon of a light sphere hanging in an air jet. The key moment is their influence on the stall zone. And returning to the prehistory of this little application of the mental mechanics of fluids (MFD - the term was introduced by Doug McLean [1]), the author begins to think that the phrase "There are no royal roads in geometry" was uttered by Euclid with a thoughtful expression and look turned inward.

References

1. McLean, Doug (Doug J.), Understanding aerodynamics: arguing from the real physics, John Wiley & Sons, Ltd., 2013.
2. Фабрикант, Н. Я., Аэродинамика, ГИТТЛ, М:, 1949, 74
3. Hydrodynamic levitation - https://www.youtube.com/watch?v=mNHp8iyyIjo
4. Wolfgang Rueckner demonstrates the Coanda Effect. Harvard Natural Sciences Lecture Demonstrations channel on YouTube, https://thekidshouldseethis.com/post/demonstrations-of-the-coanda-effect
5. Савов, В. С., Използване на пластично-хидравлична аналогия за визуализиране на течението около крилен профил, сб. Доклади на НС на ф. „Авиационен“, 2014. 55-71
6. Kadosch M., Déviation d'un jet par adhérence à une paroi convexe in Journal de Physique et le Radium, avril 1958, Paris,1–12A